2009

m VIVO TRACKING OF IRON-LABELED DENDRITIC CELLS IN MICE USING MAGNETIC RESONANCE IMAGING

Roja Rohani

Recommended Citation

Rohani, Roja, "m VIVO TRACKING OF IRON-LABELED DENDRITIC CELLS IN MICE USING MAGNETIC RESONANCE IMAGING" (2009). *Digitized Theses*. 4314.
https://ir.lib.uwo.ca/digitizedtheses/4314

IN VIVO TRACKING OF IRON-LABELED DENDRITIC CELLS IN MICE USING MAGNETIC RESONANCE IMAGING

(Spine Title: Cancer Vaccines: MRI of MPIO-Labeled Dendritic Cells)

(Thesis Format: Integrated Article)

by

Roja Rohani

Graduate Program
in
Medical Biophysics

A thesis submitted in partial fulfillment
of the requirements for the degree of
Master of Science

School of Graduate and Postdoctoral Studies
The University of Western Ontario
London, Ontario, Canada
December 2009

Abstract

Successful migration of adequate numbers of dendritic cells (DC) to draining lymph nodes is crucial for effective DC immunotherapy. Since currently, less than 3% of injected DC migrate to lymph nodes, improving DC migration is necessary. A non-invasive method is required to monitor DC migration in animal models. This work presents the first report of using Micron-sized Superparamagnetic Iron-Oxide Particles (MPIO) to label DC for detection by MRI and of tracking their migration in a mouse model in vivo.

A quantitative approach was used to measure the signal loss in MR images and the fluorescence detected by microscopy. Moreover, the fate of MPIO-labeled DC was followed longitudinally. Labeling DC with MPIO for cell tracking provides an excellent option for imaging small numbers of cells in vivo for important preclinical investigations of disease.

Keywords: Magnetic Resonance Imaging (MRI), cellular MRI, contrast agent, fast imaging employing steady state acquisition pulse sequence (FIESTA), micron sized superparamagnetic iron-oxide particles (MPIO), signal void, lymph node volume, cancer vaccine, dendritic cell, fluorescence microscopy.

برای مادرم،

معنای فداکاری، گذشت، محبت، اراده و عشق

برای همسرم، حمید،

همه هستی من
دلیل بودن من

To my Hamid,
All my reasons to live

To my mom,
The eternal flame of love

Acknowledgments

I wish I could find a word strong enough to express my feeling about my supervisor, Dr. Paula Foster. First I wanted to start with this sentence "I'd like to thank my supervisor", but then I thought "thank" is not really enough to show how much I appreciate her guidance, support and confidence in me. Without her continuous help and encouragement, as well as her thoughtful consideration to all barriers I faced as a new immigrant to Canada, it would be impossible to complete this road to graduation. Dr. Paula Foster is the best supervisor that I could ever wish for.

I would like to thank my advisory committee members, Dr. Gregory A. Dekaban and Dr. Savita Dhanvantari for their time and priceless advice. My special thanks go to the previous member of our lab, Jonatan Snir, for his precious research work, which was fundamental for mine and also for his moral help. I would also like to thank Yuhua Chen for all her help in histology and microcopy, and Christy Willert for her help in cell culture. Additionally, I should thank previous and present lab members: Elizabeth Dunn for her technical assist in the lab, Dr. Dan Jirak and Klara Hofa for their uniquely important friendship, Dr. Emeline Ribot for her best sense of humor, Laura Gonzalez-Lara for being very supportive and Shruti Krishnamoorthy for being so nice to spend a lot of time listening to my stories. I would also like to extend my thanks to members of Dr. Rutt lab. Most importantly, my Iranian friends, Roshanak Banan and Mehdi Delrobaei, have supported me in all aspects of my studies.

I would like to take this opportunity to thank Hamid, meaning of my life, who has had the most significant role in all success I have achieved. Happiness in every moment

of my life with him inspires me to go ahead. I could not have done any of this without him.

And finally, I want to express my special gratitude to my mom, who devoted herself entirely to her children. For me, she means love, kindness, insight, determination and dedication.

Table of Contents

List of Tables

List of Figures

List of Equations

List of Appendices

List of Abbreviations

3D	Three-dimensional
ANOVA	Analysis of variance
APC	Antigen presenting cell
BLI	Bioluminescence imaging
BM	Bone marrow
BSA	Bovine serum albumin
bSSFP	Balanced steady state free precession
BW	Bandwidth
CCR7	C-C chemokine receptor type 7
CO_2	Carbon dioxide
CNR	Contrast-to-noise ratio
DC	Dendritic Cells
EGFP	Enhanced green fluorescent protein
EMF	Electromotive force
FA	Flip angle
FBS	Fetal bovine serum
FID	Free induction decay
FIESTA	Fast imaging employing steady state acquisition
FOV	Field of view
Gd	Gadolinium
GM-CSF	Granulocyte-macrophage colony stimulating factor
GRE	Gradient echo
HBSS	Hank's balance salt solution
HPV	Human papilloma virus
HSPs	Heat shock proteins
ICP-MS	Inductively coupled plasma mass spectroscopy
IFN	Interferon
IL	Interleukin
kHz	Kilo Hertz
LNV	Lymph node volume
MHC	Major histocompatibility complex
MPIO	Micron-sized iron-oxide
MRI	Magnetic resonance imaging
MSCs	Mesenchymal stem cells
NK	Natural killer
PBS	Phosphate buffer solution
PFPE	Perfluoropolyether
PET	Positron emission tomography

RF	Radiofrequency
ROI	Region of Interest
RPMI	Roswell park memorial institute
S	Signal intensity
SD	Standard deviation
SE	Spin echo
SEM	Standard Error of the mean
SNR	Signal-to-noise ratio
SPIO	Superparamagnetic iron-oxide
T	Tesla
T_1	Longitudinal relaxation time constant
T_2	Transverse relaxation time constant
TAA	Tumor-associated antigen
TE	Echo time
TGF	Transforming growth factor
Th	*Helper T cell*
TNF	Tumor necrosis factor
TR	Repetition time
USFDA	U.S. food and drug administration
USPIO	Ultra-small superparamagnetic iron-oxide

Chapter 1: General Introduction

1.1. Immune Cells and the Immune System

1.1.1. Dendritic Cells

Dendritic cells (DC) have a unique role in the mammalian immune system. DC were first found as Langerhans cells in the skin in 1868 (1) and Ralph Steinman first described characteristics of mouse DC almost 30 years ago (2, 3). They are professional antigen presenting cells (APC) and some of them can stimulate T cells and initiate strong immune responses. DC are cells of the haemopoietic lineage derived from stem cells found in the bone marrow. There are two major DC subsets, myeloid DC and plasmacytoid (or lymphoid) DC and both are present at body surfaces such as the skin, pharynx, vagina, and anus as well as at mucosal surfaces such as in the respiratory and gastrointestinal systems.

Myeloid lineage DC, also known as classical DC, originate from multipotent CD34+ progenitors or peripheral blood mononuclear cells in the presence of granulocyte-macrophage colony stimulating factor (GM-CSF), tumor necrosis factor α (TNFα) ± interleukin 4 (IL-4) and transforming growth factor beta (TGF-β) (4-6). DC raised from $CD14^-$ myeloid committed cells reside in peripheral tissues as Langerhans DC to take up and process antigens. Another subset of myeloid DC migrate to the lymphoid follicles and become follicular DC which are able to activate B cells (6).

Lymphoid DC originate from lymphoid $CD34^+$ committed cells in the presence of IL-3. These cells are able to produce high amounts of interferon-alpha (IFN-α). A different subset of lymphoid DC is generated from progenitors that have the potential to mature T cells and natural killer (NK) cells (4). These progenitors are located within the thymus and T cell areas of lymph nodes (4, 5). One of their functions is to contribute to the negative selection process in the thymus. They promote the induction of apoptosis thereby eliminating potentially self-reactive T cells. They also may produce IL-10, a cytokine that induces T regulatory cells. Combined, these properties impart a regulatory function to this subset of lymphoid DC (4, 7).

DC have two stages of life: immature and mature stages (1, 8, 9). In most tissues, DC exist in the immature state. Immature DC do not have the ability to stimulate T cells, due to the lack of surface major histocompatibility complex (MHC) and co-stimulatory molecules. However, they have specific features that make them well suited for antigen capturing and processing. They take up antigens by phagocytosis, macropinocytosis and receptor-mediated endocytosis (10, 11, 12, 13). They express receptors like C-type lectin receptors, which mediate adsorptive endocytosis (1). Immature DC also possess abundant intracellular structures necessary for antigen processing such as endosomes and lysosomes as well as compartments containing high levels of intracellular MHC class II (13, 14).

When immature DC come into contact with an antigen and capture it, they undergo dramatic phenotypic changes and a maturation process (1, 16). The morphology of mature DC is characterized by the presence of abundant membrane processes that can extend for up to hundreds of micrometers. This feature fits their function, which is to contact with T cells and present antigen to them. The ability of DC to capture antigens decreases as they mature, while their features as potent APC and stimulators of T cell activation and proliferation increase. They upregulate adhesion and co-stimulatory molecules as well as peptide-MHC class II complexes on their cell surface (19). When foreign antigens are present in DC, they are degraded into short peptides and loaded onto MHC I and II molecules depending on the pathway that the antigen entered the cell (11). These complexes are then sent to the cell surface and remain there stable for variable amounts of time. Because of the rich number of peptide-MHC complexes on the surface of DC, they are highly efficient at stimulating T cells. DC can achieve peptide-MHC complexes 10-100 times higher than B cells or monocytes (1, 19). One of the major problems related to detecting DC using flow cytometry is that a single DC specific marker has yet to be identified. DC are most often identified by using a combination of different markers (6). Mature DC express large amounts of peptide-MHC class II molecules, co-stimulatory molecules such as CD40, CD80 and CD86 and adhesion molecules such as CD11 a,b,c , CD50 and CD54 (1). Mature DC are highly motile and migrate to T cell areas of lymph nodes through afferent lymphatic vessels. DC need to express chemokine receptor C-C chemokine receptor type 7 (CCR7) and CD38 to migrate to lymph nodes (20, 21).

In lymph nodes, DC may undergo further maturation and release chemokines to attract T and B cells and present peptides to naïve CD4$^+$ helper T cells, CD8$^+$ killer T cells and B cells (22). DC present processed peptides on MHC class II molecules to CD4+ helper T cells. After recognition of peptide-MHC class II complexes and activation with co-stimulatory signals (e.g., CD40, CD86), helper T cells proliferate and secrete a variety of cytokines such as IL-2, IL-4 and IL-5 that induce proliferation and activation of killer T cells, B cells and eosinophils. CD8$^+$ T cells, known as killer T cells, recognize peptides expressed on MHC class I molecules (23). Activated killer T cells, mediate the killing of the infected and dysfunctional cells.

Indeed, interaction between DC and T cells seems to be a two-way interaction rather than a one-way. DC and T cells communicate using several receptors and their ligands such as CD40/CD40L. Expression of CD40 ligand on activated T cells leads to increased DC viability (17) and facilitates DC maturation (15). Activated DC then produce IL-12 which turns T cells into IFN-γ producing Th1 cells (136). Activation of DC after CD40/CD40L interaction also leads to upregulation of CD80 and CD86 (17).

DC can also contribute to the proliferation and activation of B cells both directly and indirectly via activation of helper T cells.

1.1.2. Cancer Immunotherapy

Cancer is among the most life-threatening diseases worldwide. In Canada, it is the leading cause of premature death. Approximately, one in four Canadians dies of cancer (24). Conventional cancer therapies are surgery, radiation and chemotherapy and most patients are treated by a combination of these. Although these standard therapies are effective in treating the primary tumors, no effective therapy has been established for preventing the metastasis of the cancerous cells.

Cancer immunotherapy is a novel strategy for cancer treatment. Pioneering work in the field of cancer immunotherapy was done in the late 1800s by a surgeon, William Coley (25). He treated sarcoma patients using an immune adjuvant he called “Coley’s toxins” that was made up of killed bacteria. During the last few decades, cancer immunotherapy has moved to its modern phase through the development of novel biotechnology (26). The current approach is designed to stimulate the host’s immune system to fight against cancer more effectively. The immune system normally resists cancer growth naturally. However, when cancer does develop, the cancer cells have acquired properties that defeat immune surveillance. Immune surveillance is the early detection and destruction of abnormal cells by the immune system. Escape of cancer cells from immune surveillance is mostly the result of the lack of T cell mediated immunity (27). Cancer cells have different ways to evade the immune system. For instance, they express the host's self-antigens and therefore the host immune cells are tolerant to them (27, 28). They can also inhibit cytotoxic immune responses at the tumor site by altering and impeding the function of DC and other antigen presenting cells and they quite often downregulate MHC and co-stimulatory molecules (29). Even if MHC I and II are present, the lack of co-stimulatory molecules leads to a tolerogenic response towards tumor antigens. Furthermore, they can secrete immunosuppressant factors such as IL-10 to down-regulate the immune surveillance (30, 31). Passive cancer immunotherapy is intended to briefly supply the immune system with high amounts of effector molecules, i.e., tumor-specific antibodies or effector cells, i.e., killer T cells. (32). On the other hand, active cancer immunotherapy (cancer vaccines) is designed to induce long-term tumor antigen-specific immune responses (32, 44).

Two broad types of cancer vaccines are: preventive vaccines and therapeutic vaccines. Preventive vaccines aim to prevent cancers caused by infectious agents, such as the human papilloma virus (HPV), which causes cervical cancers, and the helicobacter pylori bacteria, which causes gastric cancers. There is one U.S. Food and Drug Administration (USFDA) approved preventive vaccine, known as Gardasil®, which protects against infection by two types of HPV, types 16 and 18, which cause almost 70 percent of all cases of cervical cancer worldwide (33).

Therapeutic vaccines are intended to treat existing cancers by strengthening the host's immune system against cancer (34). Currently, B cells, T cells or APCs have been manipulated to stimulate the immune system. T cells can be activated directly. However, it has been observed that the role of host's APCs in processing and presentation of antigens to the T cells is crucial for the detection of tumor antigens by the immune system (35). Cancer vaccines can be highly targeted, such as peptide-based vaccines, or less targeted, such as whole tumor cell cancer vaccines and tumor cell lysate vaccines (36, 37, 38, 39, 45, 46, 50, 51). Whole tumor cells used in whole tumor cell vaccines are inactivated and have a variety of abnormal tumor proteins. This has the advantage that detailed tumor analysis is not needed, since it is assumed that tumoral antigens, including as yet undefined tumor-associated antigens (TAA), are present in the whole tumor cell. After introducing these inactivated cells to the patient's body, the immune system responds to tumor proteins and generates anti-tumor immune responses. Lahn et al. showed that autologous tumor cells (a patient's own tumor cells) can be used in designing whole cell vaccines (40). Otherwise, allogeneic tumor cells (from another patient with the same type of cancer) can be used (41).

The ideal cancer vaccine would induce a strong immune response against cancerous cells without causing major autoimmunity (42). Autoimmunity is caused by the body's immune responses against self-antigens. An important challenge in the design of cancer vaccines is that all tumor cells contain self-antigens. They differ from normal cells by mutations or by the expression levels of the self-antigens. Therefore, one of the potential risks of cancer immunotherapy is the development of clinically significant autoimmunity. One approach to minimize autoimmunity and improve the specificity of vaccines is to use specific protein antigens in designing them. These antigens are over-expressed on the tumor cells but are limited, or not expressed, on normal cells. The characterization of TAA allowed the development of tumor-specific cancer vaccines (43). TAAs have been used in a number of studies for designing active cancer vaccines (45, 46, 47, 48). A number of clinical trials have been conducted with both antigen-based and whole tumor-based cancer vaccines and promising results have been obtained (45, 46, 48, 49, 50, 51, 52).

Tumor regression and increased survival rates have been observed in melanoma patients treated with cancer vaccines using different TAAs such as MART-1 (47), MAGE (46, 52) or heat shock proteins (HSPs) (53). A vaccine for renal cancer assessed in a phase III study using autologous cancer cells and lysates showed progression-free survivals (54).

1.1.3. Dendritic Cell-Based Cancer Immunotherapy

DC are considered the most potent candidate for cancer immunotherapy, since they possess a key role in the immune system and play a role as sentinels of immunity. A DC-based cancer vaccine consists of antigen-loaded DC that cause antigen-specific T-cell responses against a tumor (55, 56). In early pre-clinical studies, regression of established tumors was observed in mice injected with tumor antigen-loaded DC. Several animal studies confirmed that this resulted in minimal or no side effects (57, 58, 59, 60, 61).

The first human clinical study of a DC vaccine was published in *Nature Medicine* in 1996 (62). More than 60 different clinical trials have since been performed, between

1996 and 2004, using tumor antigen-loaded DC-based vaccines (55, 63, 64). These trials were mostly done in patients with malignant lymphoma, melanoma, colorectal carcinoma and prostate cancer and demonstrated promising results, although limited to a few patients (18, 65).

To design DC-based cancer vaccines, autologous DC are harvested from a cancer patient. They are loaded with tumor antigen and then administrated back into the patient. After administration, the antigen-loaded DC migrate to secondary lymphoid tissues and present antigen to lymphocytes that initiate cytotoxic immune responses against tumor cells presenting this antigen (55).

Pioneering work in 1992 demonstrated that mouse DC can be generated ex vivo from bone marrow precursors in the presence of GM-CSF (66). A few years after, a method was developed to generate myeloid DC from monocytes in the presence of GM-CSF and IL-4 (67). The development of these new methods for generating large numbers of normally scarce DC has boosted clinical trials. Ex vivo generated DC can be pulsed with tumor antigen in several ways, for example, with tumour-associated peptides (43, 48), tumor lysates (68), whole protein (69) or by antigen encoding mRNA or cDNA (70). These studies confirmed the stimulation of T cells after the injection of the vaccine. Fusion of tumor cells with DC is another approach, which results in the induction of T cell responses (37, 71).

The successful migration of DC to lymph nodes is essential for effective immunotherapy. The maturation state of DC has a significant impact on their migration. It has been confirmed that immature DC migrate much less than mature DC in vivo (72, 73). Still, less than 3% of mature DC appear to reach lymph nodes after subcutaneous or intradermal injection (21, 73). Other routes of DC administration have been investigated to maximize their migration. Intravenously injected DC first localize in the lungs and finally in the spleen and liver and lead to weak T cell responses (74, 75). The comparison between intravenous and subcutaneous injection routes in a mouse model of melanoma revealed that subcutaneous injection is more efficient in producing an antigen specific T cell response in lymph nodes (76). Some trials have explored the direct injection of DC into the lymph nodes or lymphatic vessels (39, 73, 74, 77). Intranodal or intralymphatic administration of DC is more challenging and time-consuming. In addition, intranodal injection can destroy the architecture of the injected lymph node and impair the potential for an immune response (72). However, migration to subsequent nodes has been observed (39, 74, 77).

Currently in most studies, DC are administrated subcutaneously or intradermally and it has been confirmed that they migrate to draining lymph nodes (56). One approach to enhance DC migration following intradermal injection is pretreatment of the injection site with inflammatory cytokines such as TNF or IL-12 (22, 57). These pretreatments have been shown to increase DC migration up to 10-fold (22). Comparing the intranodal administration of DC-based vaccines with the intradermal route needs to be explored more comprehensively.

Although the results of numerous DC trials are encouraging and suggest that there is significant promise in DC-based immunotherapy, more studies are needed to make this therapy practical. Variables that require more evaluation include: new methods for the generation of DC, routes of administration, the maturation and activation status of DC, the mode of antigen loading and the use of different DC-subsets (63).

The design of optimal DC-based cancer vaccines would be facilitated by technologies for following the fate of DC in vivo after injection. MRI provides three-dimensional, high-resolution images and is widely used in clinical practice. The basic physics of MRI is explained in the next section.

1.2. Magnetic Resonance Imaging

1.2.1. Basics of MR Physics

The nature of MRI is based on the interaction of nuclear spins with external magnetic fields. In the classical view, protons are spinning charged particles that produce a small magnetic moment (78). They possess *spin* that is a fundamental property of nature. Protons are fermions and have spin of $\frac{1}{2}$. They have spin angular momentum, $\vec{S}$, associated with a magnetic dipole moment $\vec{\mu}$ that is oriented along the spin axis and expressed as:

Equation 1.1. $$\vec{\mu} = \gamma\vec{S}$$

where γ is known as the gyromagnetic ratio. The value of $\bar{\gamma}$ ($\gamma/2\pi$) is 42.576 $\times 10^6$ Hertz per Tesla (Hz/T) for protons (78).

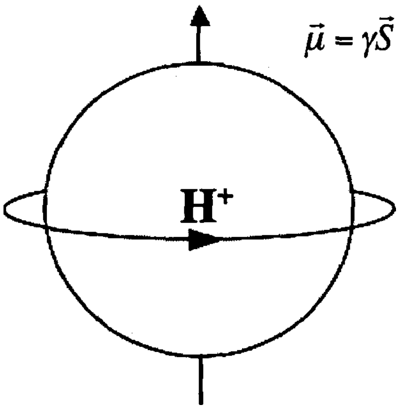

Figure 1.1. **Proton spin and its relationship to magnetic dipole momentum**

Hydrogen with one proton in its nucleus and a nuclear spin of $\frac{1}{2}$ is the most abundant atom in the body (mainly in the water followed by fat). Therefore, MR imaging of the proton is the most common approach (78).

The sum of all small magnetic moments of spins is called the net magnetization. In the absence of an external magnetic field, spins are oriented randomly and their magnetic moments cancel each other out. This distribution results in a net magnetization of zero. If a large external magnetic field (called B_0) is present, nuclear spins align with it (80). Some of the spins align in the same direction as B_0 (parallel) and some align in the opposite direction as B_0 (anti-parallel). In the B_0 magnetic field, more spins tend to align parallel to it.

The spins' actual orientation is tipped away from the B_0 axis by an angle θ. Therefore, spins' magnetic moments experience a torque that causes them to precess clockwise around the direction of the magnetic field at a frequency ω_0 (called the Larmor or resonance frequency, in Hz), and determined by:

Equation 1.2. $\vec{\omega}_0 = \gamma \vec{B}_0$ (81)

One can break down the spin's magnetic moment into two orthogonal components: a longitudinal, or Z component, and a transverse component, on the XY plane.

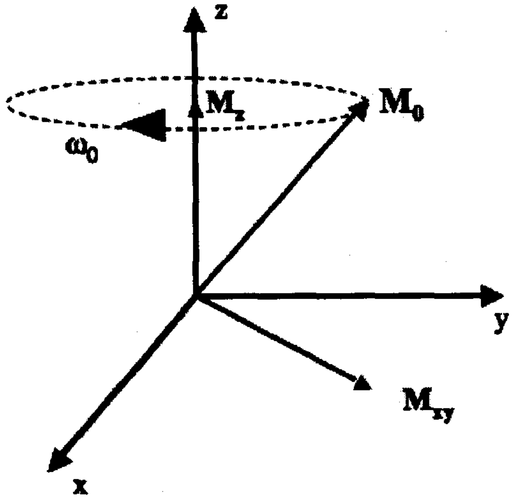

Figure 1.2. **Magnetization vector and its orthogonal components**

Because there are slightly more spins aligned parallel to the main magnetic field than anti-parallel, net magnetization, $\vec{M}_0$, is aligned with $\vec{B}_0$ and only has a component along the z-axis (longitudinal component) (81).

Resonance is the exchange of energy between two systems at a particular frequency called the resonance frequency. Nuclear magnetic resonance refers to the exchange of energy between the spin's nuclear magnetic moment and the electromagnetic radiofrequency (RF) (82). Protons can absorb the energy of an RF pulse applied at the resonance frequency. In quantum mechanics, protons jump to higher energy state after absorption of energy. In the classical view, an induced torque to M_0 causes it to tip away from the z-axis. An observer in the external laboratory frame of reference sees the magnetization vector, M_0, spiral down towards the XY plane. If the observer views the system in the rotating frame of reference, M_0 seems to smoothly tip down (79).

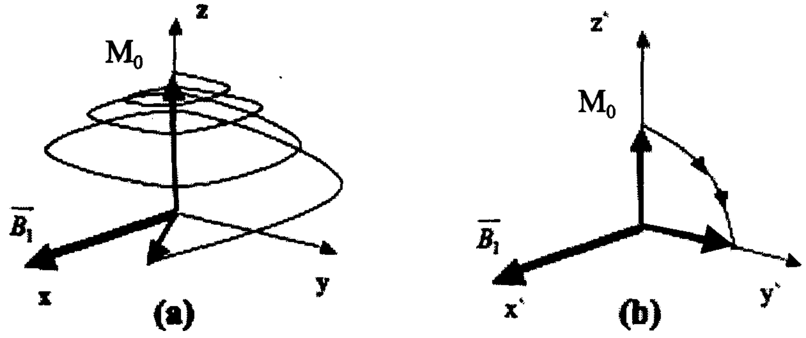

Figure 1.3. **Resonance and spin excitation in (a) the lab frame and (b) the rotating frame of references.**

The tip angle, α, is a function of the RF pulse strength, B_1, and duration, τ.

Equation 1.3. $$\alpha = \gamma B_1(t)\tau \qquad (82)$$

The applied RF pulse causes the system to be excited and thermally unstable. The system will return from the unstable state to its equilibrium if the RF pulse is re-transmitted. When the RF transmitter is turned off, the absorbed RF energy is retransmitted at the resonance frequency and simultaneously the longitudinal component of magnetization, M_z will recover (T_1 recovery) and the transverse magnetization, M_{xy}, will dephase (T_2 and T_2^* relaxation) (78).

According to Faraday's Law of induction, a change in flux ϕ in the receiver coil induces an electromotive force (EMF). Once M_z is tipped away from the z-axis, it will continue to rotate around the external B_0 field at the resonance frequency. The rotating magnetization vector, M_{xy}, induces EMF in the radiofrequency receiver coil resulting in a time signal called a free induction decay (FID) which is the basic recorded MR signal (83).

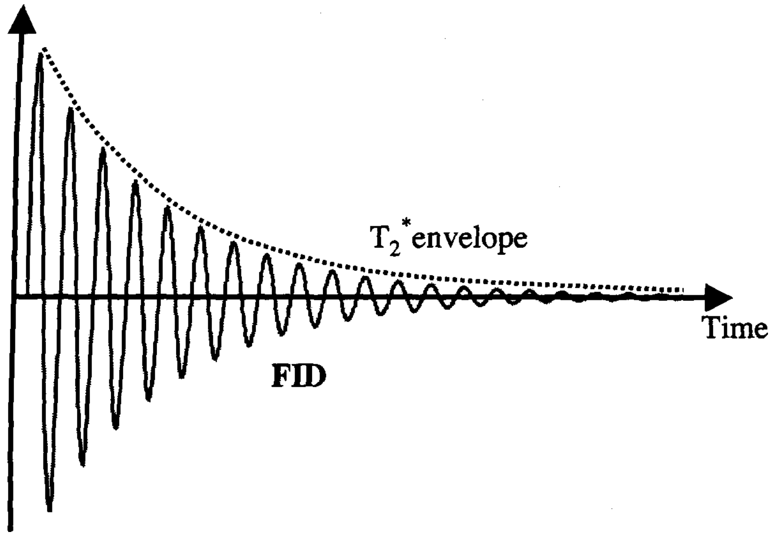

Figure 1.4. **Free Induction Decay (FID) signal.** The signal unaffected by any gradient is known as a Free Induction Decay (FID).

T_1 recovery, or T_1 relaxation, describes the return of the net magnetization vector to its equilibrium state along the z-axis. When the RF pulse is turned off, spins release the energy absorbed during excitation to the surrounding environment or spin-lattice. This type of relaxation is also called "spin-lattice relaxation". As the result of T_1 relaxation, the longitudinal magnetization component, M_z, begins to grow and recovers back to its equilibrium value. The recovery is exponential and can be mathematically described using the following equation:

Equation 1.4.

$$M_z = M_0 + [M_z(0) - M_0]e^{-\frac{t}{T_1}} \qquad (84)$$

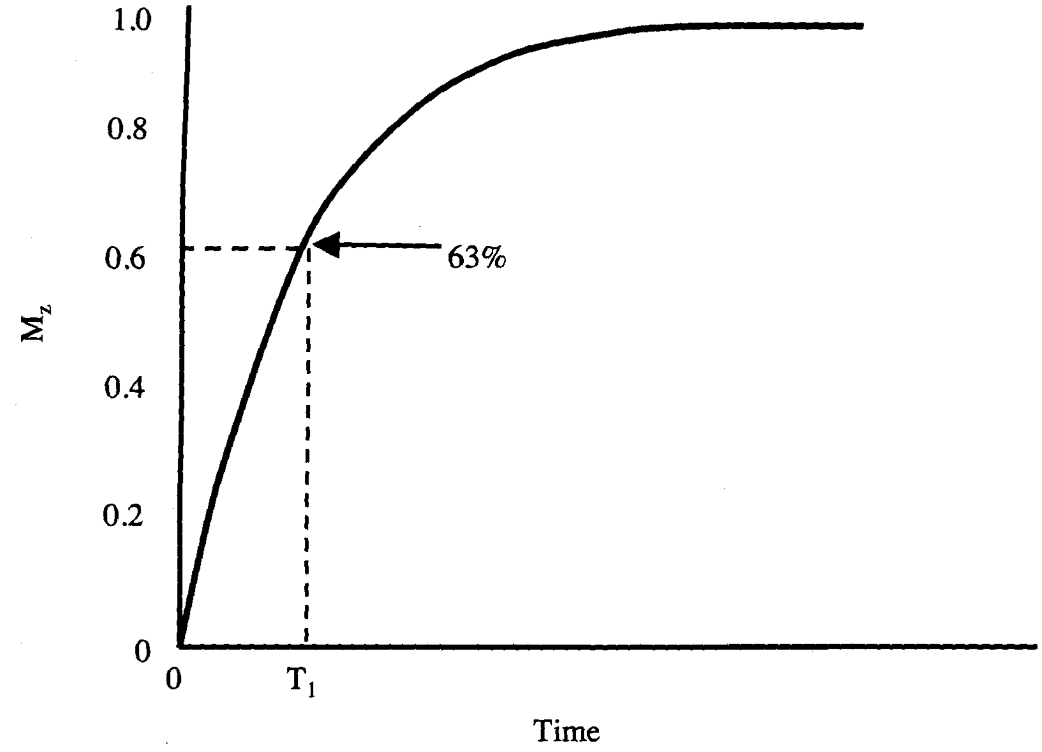

Figure 1.5. **T_1 recovery curve after a 90° excitation pulse.** The T_1 relaxation time is the time for the magnetization to return to 63% of its original magnitude.

This recovery is characterized by a tissue-specific time constant called T_1. After time T_1, longitudinal magnetization has returned to 63% of its equilibrium value. If a 90° excitation pulse is applied, M_0 is completely tipped into the XY plane i.e. $M_z(0)=0$; hence:

Equation 1.5. $$M_z = M_0(1 - e^{-\frac{t}{T_1}})$$

T_2 relaxation characterizes the decay of the transverse magnetization, M_{xy}. This form of relaxation happens because of the loss of phase coherence of the spins. When spins are in close proximity, their magnetic fields begin to interact (spin-spin interaction), resulting in different rates of precession. These temporary, random interactions lead to a cumulative loss of phase and loss of net signal. Transverse magnetization decay follows an exponential curve and can be mathematically described using the following equation:

Equation 1.6. $$M_{xy} = M_{xy0}e^{-\frac{t}{T_2}} \qquad (84)$$

If a 90° excitation pulse is applied, $M_{xy0} = M_0$.

This decay is characterized by a time constant called T_2. After time T_2, transverse magnetization has lost 63% of its initial value.

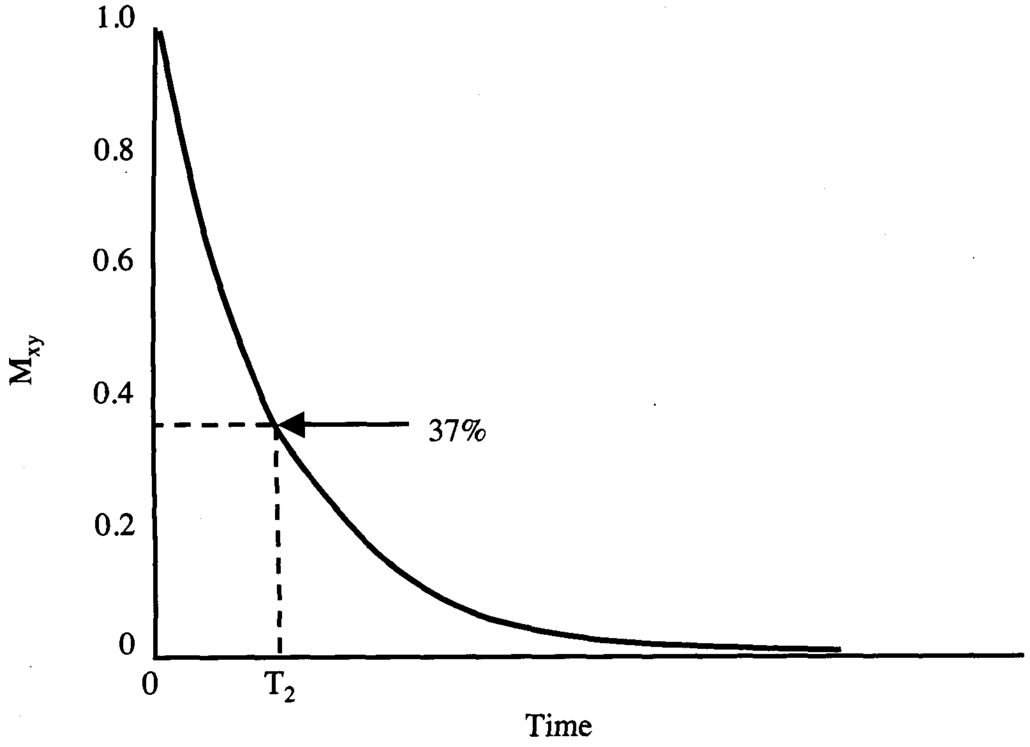

Figure 1.6. T_2 relaxation curve after a 90° excitation pulse. The T_2 relaxation time is the time it takes for the transverse magnetization to decay to 37% of its original magnitude.

Besides the effect of spin-spin relaxation, another source of relaxation hastens the net signal decay. This source is due to magnetic field inhomogeneities. There are many factors causing inhomogeneities of the magnetic field, B_0, such as variations in the static magnetic field and different magnetic susceptibilities of tissues (85). This type of relaxation is characterized by the time constant T_2'. The apparent transverse relaxation time constant T_2^* is given by:

Equation 1.7.

$$\frac{1}{T_2^*} = \frac{1}{T_2} + \frac{1}{T_2'} \qquad (84)$$

The T_2 effect is not reversible but T_2' effects can be refocused using 180° pulse, provided they are static (i.e. diffusion will result in some non-reversible diphasing from T_2' mechanisms).

Besides the main magnetic field, B_0, and the radiofrequency field, B_1, another type of magnetic field is involved in the formation of MR images. This type of magnetic field is called the linear gradient field, G, and changes the strength of B_0 linearly. In MRI a set of gradients is applied on each axis that causes the signal from each location of the sample to have a different frequency and phase. A slice selection gradient is applied to select a slice of the sample. Within this slice, the place of each point will be encoded vertically and horizontally by applying a phase encoding gradient and a frequency-encoding gradient. After the application of these three sets of gradients, a time dependent signal is detected. This signal is processed mathematically using the Fourier transform technique to acquire spatial information (83).

1.2.1. Pulse Sequences

A pulse sequence is a set of RF pulses and gradient fields applied to a sample repeatedly during the image acquisition (86). Pulse sequences are usually specified in terms of the order, spacing, amplitudes and shapes of both RF and gradient waveforms (87). In a pulse sequence, the time between repeated RF excitation pulses is called the repetition time, TR, and the time between the RF pulse and the peak of the signal is called the echo time, TE. Two main categories of pulse sequences are the spin echo (SE) sequence and the gradient echo (GRE) sequence.

In the SE pulse sequence, a 90° RF excitation pulse is applied causing the net magnetization to tip into the transverse plane. At a time TE/2, a 180° pulse is applied in order to refocus the dephasing due to T_2' mechanisms and an echo is formed at time TE (85).

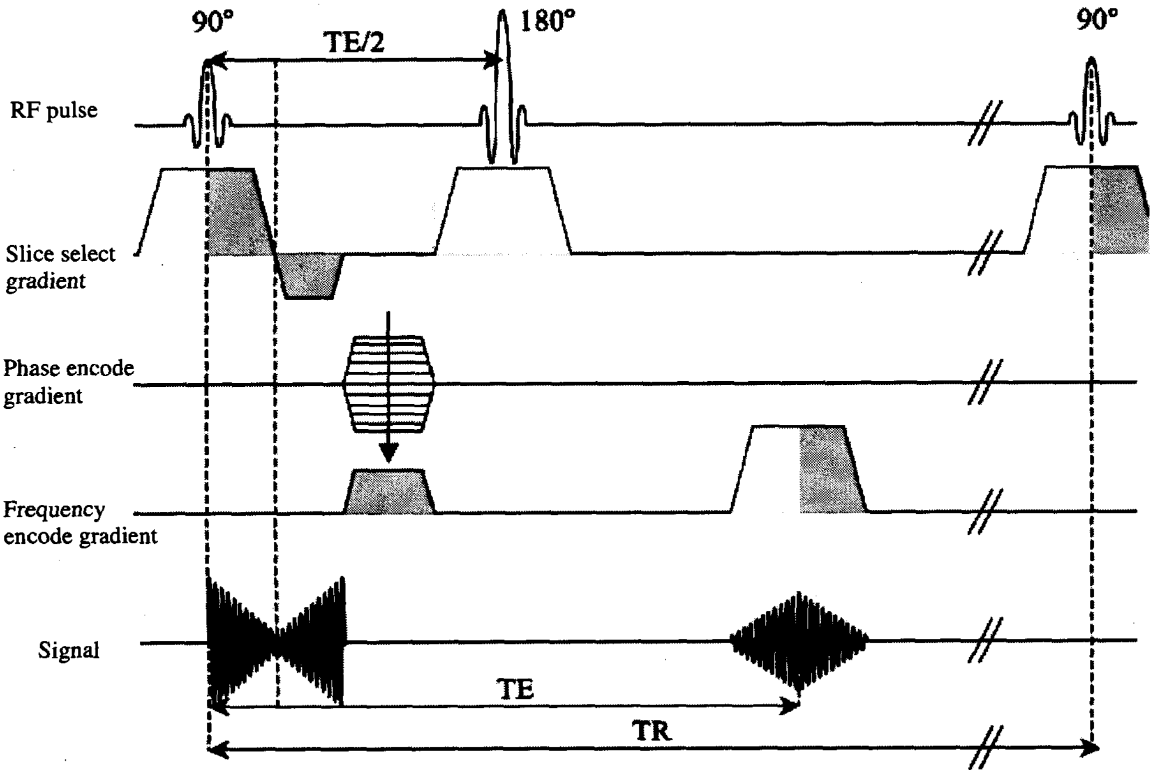

Figure 1.7. **Spin echo pulse sequence.** It uses 90° RF excitation pulses to excite the net magnetization and 180° pulses to refocus the spins to create signal echoes named spin echoes (SE).

The GRE sequence is simpler than the SE sequence and can be completed more rapidly. There are two main differences between SE and GRE pulse sequences. First, the GRE sequence employs flip angles less than 90° for excitation, in order to maintain some longitudinal magnetization undisturbed. This reduces the TR and consequently the total scan time. The second difference is that the GRE sequence does not use the 180° refocusing pulse, resulting in the persistence of T_2' effects. In the GRE sequence, gradient reversal is used to form the gradient echo. Because the applied readout gradient causes the spins to dephase during the signal acquisition, an inverse gradient is employed to refocus the magnetization and form an echo (88).

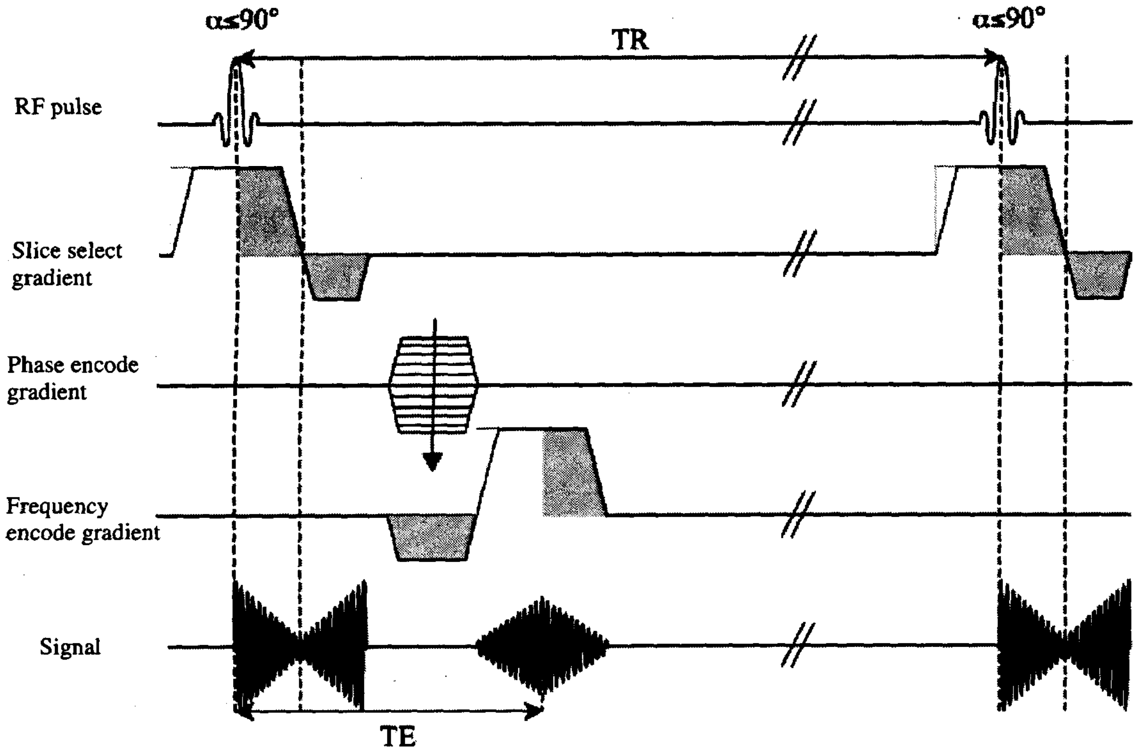

***Figure 1.8*. Gradient echo pulse sequence.** It uses pairs of bipolar gradient pulses to generate gradient echoes (GE).

The balanced steady-state free precession (b-SSFP) pulse sequence, which is used in this thesis, falls under the category of GRE sequences. This sequence requires the net magnetization to reach steady state before the data acquisition. In this sequence, the same RF pulse is applied repetitively at a short TR. Steady state is achieved when the amount of magnetization relaxation within TR is equal to the amount of tipped magnetization after excitation (89). To achieve the steady state, the TR needs to be much smaller than T_2

and T_1. This causes limited T_1 recovery and T_2 dephasing effects. In addition, α and TR must remain constant. In b-SSFP, a gradient pulse with opposite polarity is used to balance each gradient pulse applied within the TR. Fast Imaging Employing Steady-State Acquisition (FIESTA) is one of many commercial names for b-SSFP. In the FIESTA sequence, all imaging gradients along all axes are balanced before data acquisition and both longitudinal and transverse magnetizations reach steady state (90). FIESTA imaging produces a high signal to noise ratio (SNR) in a short scan time. FIESTA is very sensitive to field inhomogeneities. Because of the presence of both longitudinal and transverse magnetization during the signal acquisition, the contrast is dependent on the ratio of T_2/T_1.

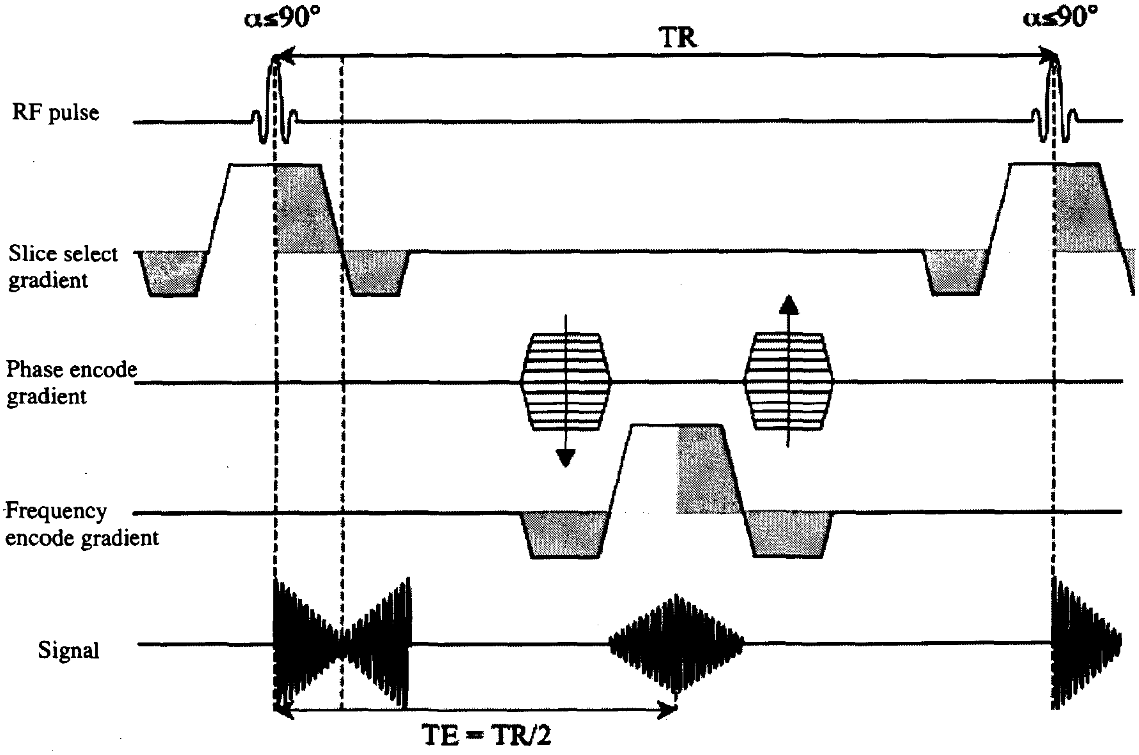

Figure 1.9. **b-SSFP pulse sequence.** In this sequence, all imaging gradients along all axes are balanced.

1.2.2. Contrast Agents

Although MRI is known to offer excellent tissue contrast, in some cases contrast agents are needed to improve the contrast between tissues. MRI contrast agents are classified by their effect on the relaxation processes (91). Two main classes of MRI contrast agents are: positive contrast agents and negative contrast agents.

Positive contrast agents are paramagnetic and cause enhancement of the signal intensity by shortening the T_1 relaxation time. They are also called T_1-shortening agents and cause enhancement of signal in T_1-weighted images. They are typically gadolinium-based agents (92). Gadolinium (Gd) has unpaired electrons in its outer shell. In the presence of an external magnetic field, they align with the field in a similar fashion to that of nuclear spins resulting in an internal magnetization (93). This leads to an energy transfer to the lattice, thus enhancing spin-lattice relaxation.

Negative contrast agents are mostly superparamagnetic iron oxide (SPIO) based particles. These particles were first used as MRI contrast agents shortly after the use of the positive agents (94, 95). Studies in animals on toxicity of these agents have shown no toxicity in doses greater than 100 times the clinical effective dose (97). Iron oxide-based agents are also known as T_2-shortening agents. Their core consists of crystallites of iron oxide, which is commonly magnetite ($Fe_2^{3+}O_3Fe^{2+}O$) (98). Within an external magnetic field, magnetic domains of the crystallites align in the same direction, forming a large net magnetization. This induces a local magnetic field gradient that is experienced by protons in the surrounding area. This leads to a rapid dephasing of nearby protons and T_2 shortening. The tissue that contains contrast agent appears as a region of signal loss in T_2 or T_2^* weighted images.

Iron-based agents vary in physical and chemical characteristics. Their properties, including the composition, size, charge and nature of the coating, determine the extent of the change in the signal intensity and their biodegradation and metabolism (99). Besides the agents' characteristics, the concentration of the particles within a given imaging voxel and the data acquisition parameters also affect the contrast generated (100).

1.2.3. Cellular MRI

Cellular MRI is a relatively young imaging field that has attracted increasing interest over the past decade. Cellular imaging can be defined as the "non-invasive and repetitive imaging of targeted cells and cellular processes in living organisms" (99). Cellular MRI combines high resolution MRI and cellular contrast agents.

The iron-based contrast agents are most widely used for cellular MRI because of their very high relaxivity, compared with the Gd-based agents. Relaxivity of a contrast agent is a quantitative measure of its efficiency to change the relaxation rates. A typical SPIO agent has a T_1 relaxivity of 30 $mM^{-1}s^{-1}$ and a T_2 relaxivity of 100 $mM^{-1}s^{-1}$, at 0.47T while a paramagnetic molecule such as Gd-DTPA has a T_1 relaxivity of 4 $mM^{-1}s^{-1}$ and a T_2 relaxivity of 6 $mM^{-1}s^{-1}$(103). This means that a much greater concentration of Gd-gadolinium molecules is needed to produce the same effect as an equivalent concentration of iron-based agent.

Iron-based agents are categorized into 3 classes in terms of their size (99): ultra-small superparamagnetic iron-oxide particles (USPIO: 10–20 nm; standard superparamagnetic iron-oxide particles (SPIO: 50 – 150 nm); and micron-sized iron-oxide particles (MPIO: 0.9 – 8.5 μm). Particle size has a dominant effect on the T_2 relaxivity of the agents because typically the greater size of a particle allows it to encapsulate more crystallites of iron oxide.

SPIO is the most commonly used agent for cellular MRI, and to date, the only clinically approved negative contrast agent. It has been used to label and track different cell types in animal models and in humans (102). Currently, SPIO is routinely used for liver imaging in the clinic because of the intense Kupffer cell (liver macrophages) uptake (104). In vitro analysis of SPIO-labeled cells indicates no adverse effect of labeling on cells viability.

The T_2^* relaxivity of SPIO was measured to be 240 ± 27 mM^{-1} s^{-1} and for MPIO 356 ± 21 mM^{-1} s^{-1} at 4.7T (100). A large amount of SPIO or USPIO particles is needed in an imaging voxel in order to change the signal intensity significantly. However, it has been shown that a single MPIO particle can be detected and used for cell labeling (101).

A potential limitation of using SPIO or USPIO for cell labeling and tracking is that they are coated with dextran that makes them biodegradable. With time, their iron is broken down and consumed by cells beyond detection. In contrast, MPIO particles are polymer-coated and not biodegradable. They persist within cells for several weeks making longitudinal studies more feasible. Some MPIO are also tagged with a fluorescent agent, which makes it possible to do both fluorescence microscopy and MRI on MPIO-labeled cells.

Particle	Iron equivalent core size (μm)	pg iron per particle	Number of particles per gram	Surface Coating
SPIO (Feridex)	0.02–0.03	10^{-6} to 10^{-7}	NA	Dextran
MPIO (Bangs Beads)	0.90	0.367	1.242×10^{12}	Polystyrene

Table 1.1. **Properties of SPIO (Feridex) and MPIO (Bangs Beads) iron-based contrast agents**

There are two main methods for labeling cells with iron-based contrast agents: *in vitro* and *in vivo* labeling. In the in vivo method iron particles are administrated intravenously and taken up by phagocytic cells, like macrophages and immature dendritic cells, involved in disease. The main clinical application of in vivo cell labeling is to detect liver metastases (104). After intravenous administration of iron particles, liver Kupffer cells (macrophages) take them up by phagocytosis and the presence of iron-labeled Kupffer cells creates regions of signal loss in MR images. Since there are large numbers of Kupffer cells in the normal liver, and relatively few macrophages in liver tumors, the normal liver tissue appears with low signal intensity and the tumor tissue appears relatively bright. This method has also been used to study the immune cells involved in diseases such as multiple sclerosis (105), organ transplant rejection (106) and atherosclerosis (107).

For in vitro cell labeling cells are incubated with the contrast agent prior to the injection or transplantation of labeled cells. Phagocytic cells are the simplest to label since they will ingest particles naturally during co-culture. Non-phagocytic cells are not labeled as efficiently by simple incubation with SPIO agents. There are a number of methods to enhance the uptake of SPIO by cells. A common method is the use of transfection agents such as protamine sulfate or lipofectamine along with the contrast agent (108, 109). Matuszewski et al showed an increase of iron oxide uptake of up to 2.6-fold after incubating with a lipofection agent (108). Another method is magnetoelectroporation, which induces reversible permeability changes in cell membranes and increases iron particle uptake (110). In contrast to SPIO, MPIO particles can be taken up easily by most cells without using transfection agents (100, 101, 111). In this study, DC were labeled in vitro by incubation with MPIO.

Cellular MRI using pre-labeling with iron agents has been used to track a variety of cells including stem cells (112), cancer cells, (113, 114) and cells of the immune system such as T cells (115) and macrophages (116). Exciting advances in the sensitivity of cellular MRI have made it possible to detect a single cell in vivo (114, 120, 121). Several studies have been done on different cell types labeled with iron-based agents in order to address concerns of the effect of labeling on cell viability and functionality. These studies have typically shown minimal changes in their viability and phenotypes (122-126). In studies of iron labeled DC, no statistical difference was observed between SPIO labeled DC and unlabeled DC in terms of the viability (126). Although it has been shown that SPIO labeling impairs the endocytic ability of DC, it does not alter DC phenotypic or functional maturation state (119).

The most common sequences for cellular MRI are T_2-weighted or T_2*-weighted pulse sequences which are most sensitive to iron. Iron-labeled cells appear as regions of signal loss in the images acquired with these pulse sequences. The size of the region of signal loss produced by iron-oxide particles is much greater than their actual size. This phenomenon is called the "blooming artifact" and facilitates the detection of small amounts of iron in the tissue.

Another main requirement for cellular MRI is high-resolution imaging. High-resolution images are typically achieved by using research-dedicated MR scanners with magnetic field strengths of 4T or higher since the higher field strength is associated with higher SNR which is necessary to maintain good image quality at high resolution. Research-dedicated MR scanners are also typically equipped with strong gradients. In this study, custom-made hardware including a gradient coil insert and solenoid mouse body RF coil, has been used along with the FIESTA pulse sequence in order to perform cellular MRI using a clinical MRI scanner at 3T.

Since negative contrast in MR images is not specific to iron-based contrast agents it is important to provide verification of the presence of labeled cells in tissue with other techniques. In most studies, histology and immunohistology of dissected tissue have been used as the standard methods to verify the detection of iron labeled cells within tissue (105 -107, 118-121).

1.2.4. Imaging Dendritic Cells

Several imaging modalities have been used to track DC migration non-invasively in vivo including scintigraphy, positron emission tomography (PET), bioluminescence imaging (BLI) and cellular MRI. (127-130)

DC are labeled with radionuclides for scintigraphy, which has been used to visualize the distribution patterns of DC in cancer patients (128, 129). The main drawbacks of scintigraphy are the lack of spatial resolution and anatomical detail (129). PET is another modality in which a radionuclide is used to label DC. It has been shown that the biodistribution of Fluorine-18-labeled DC can be visualized using PET imaging (130). However, because of the short half-life of ^{18}F, detection of the labeled DC is limited to a few hours after injection. PET also has low spatial resolution which inhibits the accurate localization of cells in tissue. Bioluminescence imaging (BLI) is used for the noninvasive detection of cells in small laboratory animals (131). BLI detects visible light produced during enzyme-mediated oxidation of a substrate. BLI has high sensitivity to detect a small number of cells. Another advantage of BLI is its short imaging time. BLI is able to produce images of multiple mice in a few seconds to minutes in a single image acquisition. Its major limitation is the limited depth of transmitted light through the object. Compared to other non-invasive imaging modalities, MRI has the highest spatial resolution and provides detailed anatomical information. At this time there are only eight papers published which have reported the use of cell labeling and MRI for imaging DC and seven of these have demonstrated the ability to track the migration of DC in vivo.

The first paper on labeling DC showed that DC can be labeled with antibody conjugated SPIO by receptor-mediated endocytosis (132). This paper showed that the uptake of SPIO in DC was increased with this labeling approach and that there was no change in their viability or phenotype. Labeled DC were implanted into the flank and detected by 11.7T MRI for up to four days. However, no DC migration was detected. In 2006, Verdijk et al. explored the sensitivity of MRI for in vitro detection of SPIO-DC on 3T and 7T scanners and estimated that with 3T MRI whole body scanners local accumulations of >1,000 SPIO-labeled cells can be detected in vivo when the iron concentration is at least 25 pg Fe/cell or more (126). In a pre-clinical study, the migration of iron-labeled DC to the draining lymph node was detected in mice using a 4.7T scanner (118).

In our own lab, we showed that mouse DC expressing enhanced green fluorescent protein (EGFP) can be labeled with SPIO and their migration visualized in vivo using a 1.5T clinical scanner (119). In addition, we reported a quantitative method to analyze MR images. We showed that the volume of signal void caused by SPIO-labeled DC and fractional signal loss correlates with migration of DC to lymph nodes.

Recently, a study has reported in vivo labeling of DC with SPIO in a mouse model (134). In this study, mice were immunized with a tumor cell–based vaccine that was irradiated and labeled with SPIO. APC, including DC, captured SPIO in the site of injection and migrated into the lymph nodes. Their accumulation was detected in the lymph nodes 3 days postvaccination using a 9.4 T scanner. Flow cytometry of dissected lymph nodes suggested that the major population of cells that took up SPIO were DC.

An important clinical study showed that SPIO-labeled DC can be tracked in humans by cellular MRI (129). In this study, a comparison was made between scintigraphy and MRI in melanoma patients after the injection of DC labeled with both ^{111}In-oxine and SPIO. This study revealed that MRI provides high-resolution images which allowed the distinction between nodes which were close together unlike scintigraphy. In addition, MRI revealed when injections were not accurate; this was missed by scintigraphy. MRI also provided high anatomical information about the localization of migrated SPIO-labeled DC in the lymph node.

There are a few reports of using contrast agents other than SPIO to image DC using cellular MRI. A paper in 2005 reported the use of ^{19}F MRI for tracking perfluoropolyether (PFPE) –labeled DC in vivo (135). In this study, PFPE-labeled DC were injected subcutaneously into the hind footpad in mice and their migration to the lymph node was detected. It has been shown that DC labeling with PFPE has minimal effects on the function of DC. ^{19}F MRI allows highly selective imaging of the labeled DC because the lack of endogenous fluorine atoms in the body causes the absence of any background signal. A great advantage of this method is that the hot spot ^{19}F images can be superimposed on anatomical ^{1}H images obtained in the same imaging session. However, using PFPE as the cell label has several limitations. Label can be diluted by cell proliferation, or released from dead cells and taken up by other cells such as macrophages. This will cause misinterpretation of labeled cells.

The first paper on labeling and imaging DC with a Gd-based contrast agent was published in 2009 (133). In this study, rat DC were incubated with ProHance^{TM} in vitro. The amount of intracellular ProHance^{TM} varied from 5.9 to 25 mM depending on the extracellular Gd-CA concentration. Loading DC with this agent did not negatively impact DC phenotype or function. To image DC in vivo, they were injected directly into tumors in the rat brain. One limitation of this approach was that the numbers of DC detected in vivo was as high as 2×10^6. Also, the retention of contrast was limited to 24 hours postinjection of labeled DC.

1.3. Thesis Overview

Cancer immunotherapy is an innovative way for treating cancer where the patient's own immune system is manipulated to fight against cancer cells. DC-based cancer vaccines have been used in clinical trails and have provided promising results. However, the poor migration of DC in vivo has been a significant barrier to the clinical implementation of DC-based cancer vaccine. So far, the deficiency of techniques to track the migration of DC non-invasively, limits our knowledge of the fate of the DC-based cancer vaccine. The focus of this research is on the in vivo validation of the use of MPIO particles for DC tracking using cellular MRI.

The use of SPIO particles for labeling and tracking DC in vivo has been previously investigated in our lab (119). Dekaban et al 2009 showed that SPIO labeling enables the detection of DC in vivo after their migration to draining lymph nodes. Moreover, a quantitative method for analysis of the signal loss caused by iron-labeled DC was described (119). For preclinical work, MPIO may have some advantages. MPIO has higher relaxivity compared to SPIO, creating larger signal change in MR images. MPIO particles are inert so the label should persist longer in vivo than with SPIO. They are also tagged with fluorescent agent. Therefore it is possible to do both fluorescence microscopy and MRI on cells labeled with such particles. We hypothesize that MPIO particles can be used to label DC and to detect, track and quantify the migration of DC in vivo using cellular MRI. A MRI cell tracking method should allow for careful and interesting in vivo investigations of strategies for improving DC cancer vaccines in preclinical models.

In Chapter 2, an imaging approach is established to track the migration of MPIO-labeled DC in vivo, in a mouse model using a 3T GE scanner with custom built gradient insert and a solenoid whole mouse body RF coil. In addition, a quantitative analysis of MR images of MPIO-labeled DC and correlative histology is presented.

In Chapter 3, the imaging approach presented in the second chapter is used for longitudinal tracking of the migration of MPIO-labeled DC in vivo. Histological analysis of lymph nodes is also presented. In this chapter, the quantification method for analysis of MR images is further assessed for inter- and intra-observer variability.

One of the main concerns for using MPIO particles in longitudinal studies is that free MPIO particles might be incorrectly identified as MPIO-labeled cells. The fourth chapter addresses this concern by studying the MRI and histological appearance of mouse lymph nodes after the injection of free MPIO. In Chapter 5, a summary of the findings and the future directions of this research are provided.

1.4. References

1. Banchereau J, Steinman RM, Dendritic cells and the control of immunity. Nature. 1998 Mar 19; 392(6673): 245-52

2. Steinman RM, Cohn ZA, Identification of a novel cell type in peripheral lymphoid organs of mice. I. Morphology, quantitation, tissue distribution. J. Exp. Med. 1973. 137: 1142–1162.

3. Steinman, RM, Cohn ZA, Identification of a novel cell type in peripheral lymphoid organs of mice. II. Functional properties in vitro. J. Exp. Med. 1974. 139: 380–397.

4. Shortman K, Caux C, Dendritic cell development: multiple pathways to nature's adjuvants. Stem Cells. 1997. 15(6): 409-19.

5. Mohamadzadeh M, Luftig R. Dendritic cells: In the forefront of immunopathogenesis and vaccine development – A review. J Immune Based Ther Vaccines. 2004 Jan 13;2(1):1

6. Wieder E, Dendritic cells: A basic review. ISCT May 2003

7. Satthaporn S, Eremin O, Dendritic cells (I): biological functions. J R Coll Surg Edinb. 2001 Feb;46(1):9-19.

8. Dieu MC, Vanbervliet B, Vicari A, Bridon JM, Oldham E, Aït-Yahia S, Brière F, Zlotnik A, Lebecque S, Caux C. Selective recruitment of immature and mature dendritic cells by distinct chemokines expressed in different anatomic sites. J Exp Med. 1998 Jul 20;188(2):373-86.

9. de Vries IJ, Eggert AA, Scharenborg NM, Vissers JL, Lesterhuis WJ, Boerman OC, Punt CJ, Adema GJ, Figdor CG. Phenotypical and Functional Characterization of Clinical Grade Dendritic Cells. J Immunother. 2002 Sep-Oct; 25(5):429-38

10. Inaba K, Inaba M, Naito M, Steinman, RM. Dendritic cell progenitors phagocytose particulates, including *Bacillus* Calmette-Guerin organisms, and sensitize mice to mycobacterial antigens *in vivo.* J Exp. Med. 1993; 178, 479–488.

11. Svensson M, Stockinger B, Wick MJ, Bone marrow-derived dendritic cells can process bacteria for MHC-1 and MHC-II presentation to T cells. J. Immunol. 1997; 158, 4229–4236.

12. Sallusto F, Lanzavecchia A, Dendritic cells use macropinocytosis and the mannose receptor to concentrate antigen to the MHC class II compartment.

Downregulation by cytokines and bacterial products. J Exp Med. 1995; 182, 389–400.

13. Sallusto, F. & Lanzavecchia, A. Efficient presentation of soluble antigen by cultured human dendritic cells is maintained by granulocyte/macrophage colony-stimulating factor plus interleukin 4 and downregulated by tumor necrosis factor a. J Exp Med. 1994; 179, 1109–1118.

14. Nijman HW, Kleijmeer MJ, Ossevoort MA, Oorschot VM, Vierboom MP, van de Keur M, Kenemans P, Kast WM, Geuze HJ, Melief CJ. Antigen capture and MHCclass II compartments of freshly isolated and cultured human blood dendritic cells. J Exp Med. 1995; 182, 163–174.

15. Grewal IS, Flavell RA. A central role of CD40 ligand in the regulation of CD4+ T-cell responses. Immunol Today. 1996 Sep;17(9):410-4.

16. Mellman I, Steinman RM. Dendritic cells: Specialized and regulated antigen processing machines. Cell 2001; 106(3):225-8.

17. Caux C, Massacrier C, Vanbervliet B, Dubois B, Van Kooten C, Durand I, Banchereau J. Activation of human dendritic cells through CD40 cross-linking. J Exp Med. 1994 Oct 1;180(4):1263-72.

18. Timmerman JM, Levy R. Dendritic cell vaccines for cancer immunotherapy. Annu Rev Med. 1999; 50:507-29.

19. Inaba K, Pack M, Inaba M, Sakuta H, Isdell F, Steinman RM. High levels of a major histocompatibility complex II–self peptide complex on dendritic cells from lymph node. J Exp Med. 1997; 186, 665–672.

20. Förster R, Schubel A, Breitfeld D, Kremmer E, Renner-Müller I, Wolf E, Lipp M. CCR7 coordinates the primary immune response by establishing functional microenvironments in secondary lymphoid organs. Cell. 1999 Oct 1;99(1):23-33.

21. Martin-Fontecha A, Sebastiani S, Höpken UE, Uguccioni M, Lipp M, Lanzavecchia A, Sallusto F. Regulation of dendritic cell migration to the draining lymph node: impact on T lymphocyte traffic and priming. J Exp Med. 2003 Aug 18;198(4):615-21.

22. Adema GJ, Hartgers F, Verstraten R, de Vries E, Marland G, Menon S, Foster J, Xu Y, Nooyen P, McClanahan T, Bacon KB, Figdor CG. dendritic-cell-derived C-C chemokine that preferentially attracts naive T cells. Nature. 1997 Jun 12; 387(6634):713-7.2.

23. Janis Kuby, Immunology. W. H. Freeman and Company. New York1992.

24. Canadian Cancer Society, Canadian cancer statistics 2009, Probability of developing or dying from cancer. Available: http://www.cancer.ca

25. Coley WB. The treatment of malignant tumors by repeated inoculations of erysipelas. With a report of ten original cases. 1893. Clin Orthop Relat Res. 1991 Jan; (262):3-11.

26. Emens LA, Jaffee EM. Cancer vaccines: an old idea comes of age. Cancer Biol Ther. 2003 Jul-Aug; 2(4 Suppl 1):S161-8

27. Marincola FM, Jaffee EM, Hicklin DJ, Ferrone S. Escape of human solid tumors from T-cell recognition: molecular mechanisms and functional significance. Adv Immunol. 2000; 74:181-273.

28. Morris EC, Bendle GM, Stauss HJ. Prospects for immunotherapy of malignant disease. Clin Exp Immunol. 2003 Jan; 131(1):1-7.

29. Radoja S, Frey AB. Cancer-induced defective cytotoxic T lymphocyte effector function: another mechanism how antigenic tumors escape immune-mediated killing. Mol Med. 2000 Jun; 6(6):465-79.

30. Salih HR, Nussler V, Commentary: Immune escape versus tumor tolerance: how do tumors evade immune surveillance? Eur J Med Res. 2001; 6, 323–332.

31. Kiessling R, Wasserman K, Horiguchi S, Kono K, Sjöberg J, Pisa P, Petersson M. Tumor-induced immune dysfunction. Cancer Immunol. Immunother. 1999; 48, 353–362.

32. Schuster M, Nechansky A, Kircheis R. Cancer immunotherapy. Biotechnol J. 2006 Feb; 1(2):138-47.

33. Doorbar J. Molecular biology of human papillomavirus infection and cervical cancer. Clin Sci (Lond). 2006; May; 110(5):525-41.

34. Giarelli E. Cancer vaccines: a new frontier in prevention and treatment. Oncology (Williston Park). 2007 Oct; 21(11 Suppl Nurse Ed):11-7

35. Maass, G, Schmidt W, Berger M, Schilcher F, Koszik F. et al., Priming of tumor-specific T cells in the draining lymph nodes after immunization with interleukin 2-secreting tumor cells: three consecutive stages may be required for successful tumor vaccination. Proc. Natl. Acad. Sci. USA 1995, 92, 5540–5544

36. Renard, V., Sonderbye, L., Ebbehoj, K., Rasmussen, P.B., Gregorius, K. et al., HER-2 DNA and protein vaccines containing potent Th cell epitopes induce distinct protective and therapeutic antitumor responses in HER-2 transgenic mice. J. Immunol. 2003, 171, 1588–1595.

37. Humann P, Moc I, Humrich J, Berger TG, Schultz ES, Schuler G, Jenne L. Antigen loading of dendritic cells with whole tumor cell preparations. J Immunol Methods. 2003; 277:1–16. doi: 10.1016/S0022-1759(03)00102-9

38. Deacon DH, Hogan KT, Swanson EM, Chianese-Bullock KA, Denlinger CE, Czarkowski AR, Schrecengost RS, Patterson JW, Teague MW, Slingluff CL Jr. The use of gamma-irradiation and ultraviolet-irradiation in the preparation of human melanoma cells for use in autologous whole-cell vaccines. BMC Cancer. 2008 Dec 4; 8:360

39. Nestle FO, Alijagic S, Gilliet M, Sun Y, Grabbe S, Dummer R, Burg G, Schadendorf D. Vaccination of melanoma patients with peptide- or tumor lysate-pulsed dendritic cells. Nat Med 1998; 4:328–32.

40. Lahn M, Köhler G, Schmoor C, Dengler W, Veelken H, Brennscheidt U, Mackensen A, Kulmburg P, Hentrich I, Jesuiter H, Rosenthal FM, Fiebig HH, Sommerkamp H, Farthmann EH, Hasse J, Mertelsmann R, Lindemann. Processing of tumor tissues for vaccination with autologous tumor cells. Eur Surg Res. 1997;29(4):292-302.

41. Chan AD, Morton DL. Active immunotherapy with allogeneic tumor cell vaccines: present status. Semin Oncol. 1998 Dec;25(6):611-22.

42. Anderson KS. Tumor Vaccines for Breast Cancer. Cancer Invest. 2009 May; 27(4):361-8.

43. Burdin N, Moingeon P. Cancer vaccines based on dendritic cells loaded with tumor-associated antigens. Cell Biol Toxicol. 2001;17(2):67-75.

44. Bertolaccini L, Olivero G, Cancer immunotherapy. A future therapeutical choice? Minerva Chir. 2001, 56, 183–191.

45. Thurner B, Haendle I, Roder C, Dieckmann D, Keikavoussi P, Jonuleit H, Bender A, Maczek C, Schreiner D, von den Driesch P, et al., Vaccination with mage-3A1 peptide-pulsed mature, monocyte-derived dendritic cells expands specific cytotoxic T cells and induces regression of some metastases in advanced stage IV melanoma. J Exp Med 1999; (190) 1669–1678

46. Marchand M, van Baren N, Weynants P, Brichard V, Dréno B, Tessier MH, Rankin E, Parmiani G, Arienti F, Humblet Y, Bourlond A, Vanwijck R, Liénard D, Beauduin M, Dietrich PY, Russo V, Kerger J, Masucci G, Jäger E, De Greve J, Atzpodien J, Brasseur F, Coulie PG, van der Bruggen P, Boon T. Tumor regressions observed in patients with metastatic melanoma treated with an antigenic peptide encoded by gene MAGE-3 and presented by HLA-A1. Int J Cancer. 1999 Jan 18;80(2):219-30.

47. Jäeger E, Bernhard H, Romero P, Ringhoffer M, Arand M, Karbach J, Ilsemann C, Hagedorn M, Knuth A. Generation of cytotoxic T-cell responses with synthetic melanoma-associated peptides in vivo: implications for tumor vaccines with melanoma-associated antigens. Int J Cancer. 1996 Apr 10;66(2):162-9.

48. Mackensen A, Herbst B, Chen JL, Köhler G, Noppen C, Herr W, Spagnoli GC, Cerundolo V, Lindemann A. Phase I study in melanoma patients of a vaccine with peptide-pulsed dendritic cells generated in vitro from CD34(+) hematopoietic progenitor cells. Int J Cancer. 2000 May 1;86(3):385-92.

49. Kugler A, Stuhler G, Walden P, Zöller G, Zobywalski A, Brossart P, Trefzer U, Ullrich S, Müller CA, Becker V, Gross AJ, Hemmerlein B, Kanz L, Müller GA, Ringert RH. Regression of human metastatic renal cell carcinoma after vaccination with tumor cell-dendritic cell hybrids. Nat Med. 2000 Mar; 6(3):332-6.

50. Berd D, Maguire HC Jr, McCue P, Mastrangelo MJ. Treatment of metastatic melanoma with an autologous tumor-cell vaccine: clinical and immunologic results in 64 patients. J Clin Oncol. 1990 Nov;8(11):1858-67.

51. Soiffer R, Lynch T, Mihm M, Jung K, Rhuda C, Schmollinger JC, Hodi FS, Liebster L, Lam P, Mentzer S, et al. Vaccination with irradiated autologous melanoma cells engineered to secrete human granulocyte-macrophage colony-stimulating factor generates potent antitumor immunity in patients with metastatic melanoma. Proc Natl Acad Sci U S A. 1998 Oct 27;95(22):13141-6.

52. Weber JS, Hua FL, Spears L, Marty V, Kuniyoshi C, Celis E. A phase I trial of an HLA-A1 restricted MAGE-3 epitope peptide with incomplete Freund's adjuvant in patients with resected high-risk melanoma. J Immunother. 1999 Sep;22(5):431-40.

53. Pilla L, Patuzzo R, Rivoltini L, Maio M, Pennacchioli E, Lamaj E, Maurichi A, Massarut S, Marchianò A, Santantonio C, Tosi D, Arienti F, Cova A, et al. A phase II trial of vaccination with autologous, tumor-derived heat-shock protein peptide complexes Gp96, in combination with GM-CSF and interferon-alpha in metastatic melanoma patients. Cancer Immunol Immunother. 2006 Aug; 55(8):958-68

54. Jocham D, Richter A, Hoffmann L, Iwig K, Fahlenkamp D, Zakrzewski G, Schmitt E, Dannenberg T, Lehmacher W, von Wietersheim J, Doehn C. Adjuvant autologous renal tumour cell vaccine and risk of tumour progression in patients with renal-cell carcinoma after radical nephrectomy: phase III, randomised controlled trial. Lancet. 2004 Feb 21;363(9409):594-9

55. Steinman RM, Banchereau J. Taking dendritic cells into medicine. Nature. 2007 Sep 27; 449(7161):419-26.

56. Figdor CG, de Vries IJ, Lesterhuis WJ, Melief CJ. Dendritic cell immunotherapy: mapping the way. Nat Med. 2004 May;10(5):475-80.

57. Mayordomo JI, Zorina T, Storkus WJ, Zitvogel L, Celluzzi C, Falo LD, Melief CJ, Ildstad ST, Kast WM, Deleo AB, et al. Bone marrow-derived dendritic cells pulsed with synthetic tumour peptides elicit protective and therapeutic antitumour immunity. Nat Med. 1995 Dec;1(12):1297-302.

58. Flamand V, Sornasse T, Thielemans K, Demanet C, Leo O, Urbain J, Moser M. Vaccination with tumor-antigen-pulsed dendritic cells induces in vivo resistance to a B cell lymphoma. Adv Exp Med Biol. 1993;329:611-6.

59. Paglia P, Chiodoni C, Rodolfo M, Colombo MP. Murine dendritic cells loaded in vitro with soluble protein prime cytotoxic T lymphocytes against tumor antigen in vivo. J Exp Med. 1996 Jan 1;183(1):7-11.

60. Porgador A, Snyder D, Gilboa E. Induction of antitumor immunity using bone marrow-generated dendritic cells. J Immunol. 1996 Apr 15;156(8):2918-26.

61. Hermans IF, Daish A, Moroni-Rawson P, Ronchese F. Tumor-peptide-pulsed dendritic cells isolated from spleen or cultured in vitro from bone marrow precursors can provide protection against tumor challenge. Cancer Immunol Immunother. 1997 Aug;44(6):341-7.

62. Hsu FJ, Benike C, Fagnoni F, Liles TM, Czerwinski D, Taidi B, Engleman EG, Levy R. Vaccination of patients with B-cell lymphoma using autologous antigen-pulsed dendritic cells. Nat Med. 1996 Jan;2(1):52-8.

63. Aarntzen EH, Figdor CG, Adema GJ, Punt CJ, de Vries IJ. Dendritic cell vaccination and immune monitoring. Cancer Immunol Immunother. 2008 Oct;57(10):1559-68.

64. Rosenberg SA, Yang JC, Restifo NP. Cancer immunotherapy: moving beyond current vaccines. Nat Med. 2004 Sep;10(9):909-15.

65. Ridgway D. The first 1000 dendritic cell vaccines. Cancer Invest. 2003; 21(6):873-86.

66. Inaba K, Inaba M, Romani N, Aya H, Deguchi M, Ikehara S, Muramatsu S, Steinman RM. Generation of large numbers of dendritic cells from mouse bone marrow cultures supplemented with granulocyte/macrophage colony-stimulating factor. J Exp Med. 1992 Dec 1;176(6):1693-702.

67. Romani N, Gruner S, Brang D, Kämpgen E, Lenz A, Trockenbacher B, Konwalinka G, Fritsch PO, Steinman RM, Schuler G. Proliferating dendritic cell progenitors in human blood. J Exp Med. 1994 Jul 1; 180(1):83-93.

68. Bercovici N, Haicheur N, Massicard S, Vernel-Pauillac F, Adotevi O, Landais D, Gorin I, Robert C, Prince HM, Grob JJ, Leccia MT, Lesimple T, Wijdenes J, Bartholeyns J, Fridman WH, Salcedo M, Ferries E, Tartour E. Analysis and characterization of antitumor T-cell response after administration of dendritic cells loaded with allogeneic tumor lysate to metastatic melanoma patients. J Immunother. 2008 Jan; 31(1):101-12

69. Adam C, Mysliwietz J, Mocikat R. Specific targeting of whole lymphoma cells to dendritic cells ex vivo provides a potent antitumor vaccine. J Transl Med. 2007 Mar 14; 5:16.

70. Su Z, Dannull J, Yang BK, Dahm P, Coleman D, Yancey D, Sichi S, Niedzwiecki D, Boczkowski D, Gilboa E, Vieweg J. Telomerase mRNA-transfected dendritic cells stimulate antigen-specific CD8+ and CD4+ T cell responses in patients with metastatic prostate cancer. J Immunol. 2005 Mar 15;174(6):3798-807.

71. Wang J, Saffold S, Cao X, Krauss J, Chen W. Eliciting T cell immunity against poorly immunogenic tumors by immunization with dendritic cell-tumor fusion vaccines. J Immunol. 1998 Nov 15;161(10):5516-24.

72. Adema GJ, de Vries IJ, Punt CJ, Figdor CG. Migration of dendritic cell based cancer vaccines: in vivo veritas? Curr Opin Immunol. 2005 Apr;17(2):170-4.

73. De Vries IJ, Krooshoop DJ, Scharenborg NM, Lesterhuis WJ, Diepstra JH, Van Muijen GN, Strijk SP, Ruers TJ, Boerman OC, Oyen WJ, Adema GJ, Punt CJ, Figdor CG. Effective migration of antigen-pulsed dendritic cells to lymph nodes in melanoma patients is determined by their maturation state. Cancer Res. 2003 Jan 1;63(1):12-7.

74. Mackensen A, Krause T, Blum U, Uhrmeister P, Mertelsmann R, Lindemann A. Homing of intravenously and intralymphatically injected human dendritic cells generated in vitro from CD34+ hematopoietic progenitor cells. Cancer Immunol Immunother. 1999 May-Jun;48(2-3):118-22.

75. Fong L, Brockstedt D, Benike C, Wu L, Engleman EG. Dendritic cells injected via different routes induce immunity in cancer patients. J Immunol. 2001 Mar 15;166(6):4254-9.

76. Mullins DW, Sheasley SL, Ream RM, Bullock TN, Fu YX, Engelhard VH. Route of immunization with peptide-pulsed dendritic cells controls the distribution of memory and effector T cells in lymphoid tissues and determines the pattern of regional tumor control. J Exp Med. 2003 Oct 6;198(7):1023-34.

77. Jonuleit H, Giesecke-Tuettenberg A, Tüting T, Thurner-Schuler B, Stuge TB, Paragnik L, Kandemir A, Lee PP, Schuler G, Knop J, Enk AH. A comparison of

two types of dendritic cell as adjuvants for the induction of melanoma-specific T-cell responses in humans following intranodal injection. Int J Cancer. 2001 Jul 15;93(2):243-51.

78. Nishimura DG. Physics, in Principles of magnetic resonance imaging. 1995, Stanford University: Stanford, CA. p. 55-66.

79. Haacke EM. Magnetic Resonance Imaging: physical principles and sequence design. New York: J. Wiley-Liss; 1999. P. 68-71.

80. Pykett IL, Newhouse JH, Buonanno FS, Brady TJ, Goldman MR, Kistler JP, Pohost GM. Principles of nuclear magnetic resonance imaging. Radiology. 1982 Apr; 143(1):157-68.

81. Haacke EM. Magnetic Resonance Imaging: physical principles and sequence design. New York: J. Wiley-Liss; 1999. P. 1-16.

82. Nishimura DG. Excitation, in Principles of magnetic resonance imaging. 1995, Stanford University: Stanford, CA. p. 107-132.

83. Nishimura DG. Overview, in Principles of magnetic resonance imaging. 1995, Stanford University: Stanford, CA. p. 33-54.

84. Haacke EM. Magnetic Resonance Imaging: physical principles and sequence design. New York: J. Wiley-Liss; 1999. P. 51-64.

85. Nishimura DG. Imaging Consideration, in Principles of magnetic resonance imaging. 1995, Stanford University: Stanford, CA. p. 133-176.

86. Hornak JP. The basic of NMR, Rochester Institute of Technology, Rochester, NY 1997-99

87. Brown MA, RC Semelka, Pulse sequences, in MRI: basic principles and applications. 1995, Wiley-Liss: New York. p. 45-67.

88. Westbrook C, Roth CK, Talbot J. Pulse sequences, MRI in practice. Wiley-Blackwell; June 2005, p. 143-201

89. Chavhan GB, Babyn PS, Jankharia BG, Cheng HL, Shroff MM. Steady-state MR imaging sequences: physics, classification, and clinical applications. Radiographics. 2008 Jul-Aug; 28(4):1147-60.

90. Scheffler, K. and S. Lehnhardt, Principles and applications of balanced SSFP techniques. Eur Radiol, 2003. 13(11): p. 2409-18.

91. Strijkers GJ, Mulder WJ, van Tilborg GA, Nicolay K. MRI contrast agents: current status and future perspectives. Anticancer Agents Med Chem. 2007 May;7(3):291-305.
92. Werner EJ, Datta A, Jocher CJ, Raymond KN. High-relaxivity MRI contrast agents: where coordination chemistry meets medical imaging. Angew Chem Int Ed Engl. 2008;47(45):8568-80.
93. Caravan P, Ellison JJ, McMurry TJ, Lauffer RB. Gadolinium(III) Chelates as MRI Contrast Agents: Structure, Dynamics, and Applications. Chem Rev. 1999 Sep 8;99(9):2293-352.
94. Mendonca Dias MH, Lauterbur PC. Ferromagnetic particles as contrast agents for magnetic resonance imaging of liver and spleen. Magn. Reson. Med. 1986; 3: 328–330.
95. Olsson M, Persson B, Salford L, Schroder U. Ferromagnetic particles as contrast agents in T2 NMR imaging. Magn. Reson. Imaging 1986; 4: 437–440.
96. Bulte JW, Kraitchman DL. Iron oxide MR contrast agents for molecular and cellular imaging. NMR Biomed. 2004 Nov; 17(7):484-99.
97. Simonsen CZ, Ostergaard L, Vestergaard-Poulsen P, Røhl L, Bjørnerud A, Gyldensted C. CBF and CBV measurements by USPIO bolus tracking: reproducibility and comparison with Gd-based values. J Magn Reson Imaging. 1999 Feb;9(2):342-7.
98. Wang YX, Hussain SM, Krestin GP. Superparamagnetic iron oxide contrast agents: physicochemical characteristics and applications in MR imaging. Eur Radiol. 2001;11(11):2319-31.
99. Modo M, Hoehn M, Bulte JW. Cellular MR imaging. Mol Imaging. 2005 Jul-Sep;4(3):143-64.
100. Hinds KA, Hill JM, Shapiro EM, Laukkanen MO, Silva AC, Combs CA, Varney TR, Balaban RS, Koretsky AP, Dunbar CE. Highly efficient endosomal labeling of progenitor and stem cells with large magnetic particles allows magnetic resonance imaging of single cells. Blood, 2003. 102(3): p. 867-72.
101. Shapiro EM, Skrtic S, Sharer K, Hill JM, Dunbar CE, Koretsky AP. MRI detection of single particles for cellular imaging. Proc Natl Acad Sci U S A. 2004 Jul 27;101(30):10901-6. Epub 2004 Jul 15
102. Liu W, Frank JA. Detection and quantification of magnetically labeled cells by cellular MRI. Eur J Radiol. 2009 May;70(2):258-64.

103. Jung CW, Jacobs P. Physical and chemical properties of superparamagnetic iron oxide MR contrast agents: ferumoxides, ferumoxtran, ferumoxsil. Magn Reson Imaging. 1995;13(5):661-74.

104. Stark DD,Weissleder R, Elizondo G, Hahn PF, Saini S, Todd LE, Wittenberg J, Ferrucci JT. Superparamagnetic iron oxide: clinical application as a contrast agent for MR imaging of the liver. Radiology 1988; 168: 297–301.

105. Dousset V, Delalande C, Ballarino L, Quesson B, Seilhan D, Coussemacq M, Thiaudiére E, Brochet B, Canioni P, Caillé JM. In vivo macrophage activity imaging in the central nervous system detected by magnetic resonance. Magn Reson Med, 1999. 41(2): p. 329-33.

106. Zhang Y, Dodd SJ, Hendrich KS, Williams M, Ho C. Magnetic resonance imaging detection of rat renal transplant rejection by monitoring macrophage infiltration. Kidney Int, 2000. 58(3): p.1300-10.

107. Schmitz SA, Coupland SE, Gust R, Winterhalter S, Wagner S, Kresse M, Semmler W, Wolf KJ. Superparamagnetic iron oxide-enhanced MRI of atherosclerotic plaques in Watanabe hereditable hyperlipidemic rabbits. Invest Radiol, 2000. 35(8): p. 460-71.

108. Matuszewski L, Persigehl T, Wall A, Schwindt W, Tombach B, Fobker M, Poremba C, Ebert W, Heindel W, Bremer C. Cell tagging with clinically approved iron oxides: feasibility and effect of lipofection, particle size, and surface coating on labeling efficiency. Radiology. 2005 Apr;235(1):155-61. Epub 2005 Mar 4.

109. Arbab AS, Yocum GT, Rad AM, Khakoo AY, Fellowes V, Read EJ, Frank JA. Labeling of cells with ferumoxides-protamine sulfate complexes does not inhibit function or differentiation capacity of hematopoietic or mesenchymal stem cells. NMR Biomed. 2005 Dec;18(8):553-9

110. Walczak P, Kedziorek DA, Gilad AA, Lin S, Bulte JW. Instant MR labeling of stem cells using magnetoelectroporation. Magn Reson Med. 2005 Oct;54(4):769-74.

111. Shapiro EM, S Skrtic, AP Koretsky. Sizing it up: cellular MRI using micron-sized iron oxide particles. Magn Reson Med, 2005. 53(2): p. 329-38.

112. Kraitchman DL, Bulte JW. Imaging of stem cells using MRI. Basic Res Cardiol. 2008 Mar;103(2):105-13.

113. Fleige G, Nolte C, Synowitz M, Seeberger F, Kettenmann H, Zimmer C. Magnetic labeling of activated microglia in experimental gliomas. Neoplasia. 2001 Nov-Dec;3(6):489-99.

114. Heyn C, Ronald JA, Mackenzie LT, MacDonald IC, Chambers AF, Rutt BK, Foster PJ. In vivo magnetic resonance imaging of single cells in mouse brain with optical validation. Magn Reson Med. 2006 Jan;55(1):23-9.

115. Shapiro EM, Medford-Davis LN, Fahmy TM, Dunbar CE, Koretsky AP. Antibody-mediated cell labeling of peripheral T cells with micron-sized iron oxide particles (MPIOs) allows single cell detection by MRI. Contrast Media Mol Imaging. 2007 May;2(3):147-53.

116. Williams JB, Ye Q, Hitchens TK, Kaufman CL, Ho C. MRI detection of macrophages labeled using micrometer-sized iron oxide particles. J Magn Reson Imaging. 2007 Jun;25(6):1210-8.

117. Baumjohann D, Lutz MB. Non-invasive imaging of dendritic cell migration in vivo. Immunobiology. 2006;211(6-8):587-97. Epub 2006 Jul 3.

118. Baumjohann D, Hess A, Budinsky L, Brune K, Schuler G, Lutz MB. In vivo magnetic resonance imaging of dendritic cell migration into the draining lymph nodes of mice. Eur J Immunol. 2006 Sep;36(9):2544-55.

119. Dekaban GA, Snir J, Shrum B, de Chickera S, Willert C, Merrill M, Said EA, Sekaly RP, Foster PJ, O'Connell PJ. Semiquantitation of mouse dendritic cell migration in vivo using cellular MRI. J Immunother. 2009 Apr;32(3):240-51.

120. Smirnov P, Poirier-Quinot M, Wilhelm C, Lavergne E, Ginefri JC, Combadière B, Clément O, Darrasse L, Gazeau F. In vivo single cell detection of tumor-infiltrating lymphocytes with a clinical 1.5 Tesla MRI system. Magn Reson Med. 2008 Dec;60(6):1292-7.

121. Shapiro EM, Sharer K, Skrtic S, Koretsky AP. In vivo detection of single cells by MRI. Magn Reson Med. 2006 Feb;55(2):242-9.

122. Arbab AS, Bashaw LA, Miller BR, Jordan EK, Lewis BK, Kalish H, Frank JA. Characterization of biophysical and metabolic properties of cells labeled with superparamagnetic iron oxide nanoparticles and transfection agent for cellular MR imaging. Radiology. 2003 Dec;229(3):838-46.

123. Mai XL, Ma ZL, Sun JH, Ju SH, Ma M, Teng GJ. Assessments of proliferation capacity and viability of New Zealand rabbit peripheral blood endothelial progenitor cells labeled with superparamagnetic particles. Cell Transplant. 2009;18(2):171-81.

124. Berkova Z, Kriz J, Girman P, Zacharovova K, Koblas T, Dovolilova E, Saudek F. Vitality of pancreatic islets labeled for magnetic resonance imaging with iron particles. Transplant Proc. 2005 Oct;37(8):3496-8.

125. Kim HS, Choi Y, Song IC, Moon WK. Magnetic resonance imaging and biological properties of pancreatic islets labeled with iron oxide nanoparticles. NMR Biomed. 2009 Jun 1.

126. Verdijk P, Scheenen TW, Lesterhuis WJ, Gambarota G, Veltien AA, Walczak P, Scharenborg NM, Bulte JW, Punt CJ, Heerschap A, Figdor CG, de Vries IJ. Sensitivity of magnetic resonance imaging of dendritic cells for in vivo tracking of cellular cancer vaccines. Int J Cancer. 2006 Mar 1;120(5):978-84.

127. Schimmelpfennig CH, Schulz S, Arber C, Baker J, Tarner I, McBride J, Contag CH, Negrin RS. Ex vivo expanded dendritic cells home to T-cell zones of lymphoid organs and survive in vivo after allogeneic bone marrow transplantation. Am J Pathol. 2005 Nov;167(5):1321-31.

128. Blocklet D, Toungouz M, Kiss R, Lambermont M, Velu T, Duriau D, Goldman M, Goldman S. 111In-oxine and 99mTc-HMPAO labelling of antigen-loaded dendritic cells: in vivo imaging and influence on motility and actin content. Eur J Nucl Med Mol Imaging. 2003 Mar;30(3):440-7.

129. de Vries IJ, Lesterhuis WJ, Barentsz JO, Verdijk P, van Krieken JH, Boerman OC, Oyen WJ, Bonenkamp JJ, Boezeman JB, Adema GJ, Bulte JW, Scheenen TW, Punt CJ, Heerschap A, Figdor CG. Magnetic resonance tracking of dendritic cells in melanoma patients for monitoring of cellular therapy. Nat Biotechnol. 2005 Nov;23(11):1407-13.

130. Olasz EB, Lang L, Seidel J, Green MV, Eckelman WC, Katz SI. Fluorine-18 labeled mouse bone marrow-derived dendritic cells can be detected in vivo by high resolution projection imaging. J Immunol Methods. 2002 Feb 1;260(1-2):137-48

131. Contag CH, Bachmann MH. Advances in in vivo bioluminescence imaging of gene expression. Annu Rev Biomed Eng. 2002;4:235-60.

132. Ahrens ET, Feili-Hariri M, Xu H, Genove G, Morel PA. Receptor-mediated endocytosis of iron-oxide particles provides efficient labeling of dendritic cells for in vivo MR imaging. Magn Reson Med. 2003 Jun;49(6):1006-13.

133. Sengar RS, Spokauskiene L, Steed DP, Griffin P, Arbujas N, Chambers WH, Wiener EC. Magnetic resonance imaging-guided adoptive cellular immunotherapy of central nervous system tumors with a T(1) contrast agent. Magn Reson Med. 2009 Jun 18.

134. Long CM, van Laarhoven HW, Bulte JW, Levitsky HI. Magnetovaccination as a novel method to assess and quantify dendritic cell tumor antigen capture and delivery to lymph nodes. Cancer Res. 2009 Apr 1;69(7):3180-7.

135. Ahrens ET, Flores R, Xu H, Morel PA. In vivo imaging platform for tracking immunotherapeutic cells. Nat Biotechnol. 2005 Aug;23(8):983-7.

136. Mackey MF, Gunn JR, Maliszewski CR, Kikutani H, Noeller RJ, Barth JR. DC require maturation via CD40 to generate protective anti-tumor immunity. J Immunol 1998, 161:2094-2098.

Chapter 2: Tracking MPIO-labeled Dendritic Cells In Vivo

Work presented in this chapter was done in collaboration with Dr. Gregory Dekaban. DC isolation, iron labeling and injection were performed by Christy Willert. Yuhua Chen, lab manager of Foster group performed cryosectioning of lymph nodes. Development of the custom gradient insert coil and radiofrequency coils used in this project was completed in Dr. Rutt's Lab. All other procedures including MR acquisition, mouse anesthesia, data analysis, tissue dissection and preparation for microscopy and fluorescence microscopy were performed by Roja Rohani.

2.1. Introduction

The manipulation of immune cells to recognize and attack cancer cells is the main idea behind cancer immunotherapy. Among all immune cells, dendritic cells (DC) are unique in their ability to professionally present antigens and act as the adjuvant (1, 2). DC capture antigens in peripheral tissues and migrate to lymph nodes to introduce them to T cells and induce antigen-specific immune responses. Because of their important role in the immune system, DC have been widely explored in designing cancer vaccines (3, 4, 5). The results of clinical trials investigating DC-based cancer vaccines have been promising. They have showed that DC vaccines are safe and non-toxic. These trials have reported generation of tumor specific immune responses and reductions in metastasis (3, 4, 5).

The success of immunotherapy with a DC-based cancer vaccine depends on the efficient migration of DC to secondary lymphoid organs. However, after subcutaneous or intradermal injection of in vitro generated DC only 0.01 to 3 % of them migrate to lymph nodes (6, 22). Most current methods used to assess the migration of DC are invasive and require biopsy or removal of tissues. Therefore, there is a strong need for a non-invasive and sensitive method to follow the migration of DC in vivo.

A number of labs have now shown that DC can be labeled with iron nanoparticles for detection by MRI (7-12). These studies have shown that DC can take up SPIO with minimal or no side effects on their viability or functionality. Three preclinical studies have reported detection of SPIO-DC migration to the lymph nodes (9, 11, 12). Previously in our lab we have shown that the migration of SPIO-labeled DC can be tracked in mice using a steady-state acquisition (FIESTA) pulse sequence at 1.5T on a clinical scanner (9). In the only clinical study on SPIO-DC, it has been confirmed that SPIO-labeled DC can be imaged in humans using cellular MRI (7).

To date, all papers which use iron for DC tracking with MRI have used SPIO as the cell label. In this chapter, we explore the use of a different MRI cell label for imaging DC migration, what is known as micron sized iron oxide (MPIO). MPIO, which is commercially available, is a larger particle than SPIO and creates a much larger magnetization within individual cells, increasing the possibility of in vivo detection of single cells or very small numbers of cells. It is a feasible label to image different cell types such as macrophages (13, 14), T cells (15), glioma cells (16), hematopoeitic progenitor (CD34+) and mesenchymal stem cells (MSCs) (18) using cellular MRI without altering their functionality and viability. Shapiro et al (2004) showed that a single MPIO particle can be detected in the fixed mouse embryo using cellular MRI (17). Different studies also have reported imaging single MPIO-labeled cells in vitro and in vivo (15-18). Since MPIO particles are not biodegradable, they can stay within the cells for several weeks. Moreover, the fluorescent tag on their coating makes fluorescent microscopy possible.

In this chapter, we show that MPIO particles can be used to label DC without affecting their viability and that the migration of MPIO-labeled DC to the popliteal lymph node can be tracked by MRI. We are able to measure the volume of the lymph nodes and of the regions of signal loss caused by the MPIO-labeled DC. Moreover, we show by histology that the signal loss caused by MPIO-labeled DC can be related to the presence of MPIO-labeled DC in the draining lymph nodes.

2.2. Methods

2.2.1. Animal Groups

All protocols in this study were accredited by the University of Western Ontario Animal Use Subcommittee and agreed with the guidelines of the Canadian Council on Animal Care.

Two experiments were performed with two groups of mice. In the first experiment, DC were acquired from enhanced green fluorescence protein (EGFP) (C57BL/6-Tg[ACTB-EGFP]10sb/J) C57Bl/6 mice. In this experiment, 0.1×10^6 or 1×10^6 EGFP+ MPIO-labeled DC were injected subcutaneously into the left hind footpad of recipient C57Bl/6 mice (n=8, n=4 for each cell dose) and the equivalent number of unlabeled DC to their right hind footpad. In the second experiment, DC were obtained from wildtype C57Bl/6 mice (instead of EGFP+ mice) and PKH was used as the cell tracker. PKH is a fluorescent cell membrane linker. We used green PKH67 (excitation:emission peaks, 490:502 nm). In this experiment, 0.1×10^6 or 1×10^6 PKH+ MPIO-labeled or unlabeled DC were injected subcutaneously to the hind footpad of

C57Bl/6 mice (n=8, n=4 for each cell dose). Before the injection, mice were anesthetized with the gas anesthetic isofluorane (Forane, Baxter) (1% in 100% oxygen) and injections were done with a 28-gauge needle.

2.2.2. Dendritic Cell Culture and MPIO Labeling

Bone marrow (BM) DC were derived from femurs and tibias of 8-12 week old C57Bl/6 (Charles River Laboratory, Wilmington, MA) mice. The BM cells were collected by centrifugation at 500xg for 5 minutes using an Ependorf 5804R. After collecting, BM cells were cultured in an incubator in 1 mL of Roswell Park Memorial Institute (RPMI) 1640 media (Invitrogen) supplemented with 10% fetal bovine serum (FBS), 1% nonessential amino acids, L-glutamine, sodium pyruvate, penicillin streptomycin and 2-mercaptoethanol (Invitrogen) in the presence of granulocyte-macrophage colony-stimulating factor (GM-CSF) and Interleukin-4 (IL-4). They were cultured at 37° in a humidified atmosphere of 5% carbon dioxide (CO_2) in air for 4 days. DC were enriched by centrifugation over histodenz (132mg/mL, 25min, 500×g; Sigma). DC were labeled by overnight incubation with 12.5 μg/ml MPIO (Bangs beads, Bangs Laboratories, Fisher, IN). MPIO were 0.90 μm in diameter and tagged with flash-red fluorescent agent (excitation:emission peaks, 660:690 nm). Cells were washed with ice-cold Hank's balance salt solution (HBSS, Invitrogen) with 0.1% bovine serum albumin (BSA, Sigma) to ensure removal of unincorporated contrast agent. Unlabeled DC were used for the control experiment. Inductively coupled plasma mass spectroscopy (ICP-MS) was used to evaluate the iron content per cell. DC were further labeled with PKH67 Green Fluorescent cell linker. A suspension containing 2×10^7 DC was placed in a conical bottom polypropylene tube and washed once using HBSS with 0.1% BSA. Cells were washed a second time with phosphate buffer solution (PBS) with no BSA. After centrifuging cells (500*g*) for 5 minutes, the supernatant was carefully poured off. 1 mL of Diluent C was added to DC. Prior to staining, cells were counted and an appropriate volume of PKH dye was added such that a 2x working dye solution ($4x10^{-6}$) was made for every $2x10^{7}$ DC. 1 mL of cell suspension was rapidly added to 1 mL of dye and immediately mixed by pipetting. Cells were incubated at room temperature for 2-5 minutes with periodic mixing. An equal volume (2 mL) of FBS was added and incubated for 1 minute. 4mL of complete RPMI (with FBS) was added. DC were centrifuged at 500*g* for 5 minutes at 4° C. DC were washed once with HBSS with 0.1% BSA. DC were then resuspended in PBS with no BSA to count and then washed again before injection.

To detect intracellular uptake of MPIO particles, labeled DC were transferred to a cytospin centrifuge (Thermo Scientific). MPIO-labeled DC were spun onto glass microscope slides covered by a filter card. Slides were stained with Perl's Prussian blue (PPB) and eosin.

The trypan blue exclusion assay and flow cytometry analysis were performed to verify viability of MPIO-labeled cells. For flow cytometry, cells were stained with Annexin V conjugated to Phycoerythrin (PE) fluorochrome and 7-Amino-Actinomycin (7-AAD) to determine apoptotic or necrotic cell death.

2.2.3. Cellular MR Imaging

Imaging was performed in vivo using a 3 Tesla (3T) GE whole-body MR scanner (MR Signa® Excite™, GE Healthcare, Milwaukee, WI, USA) with a custom-built gradient coil (inner diameter=17.5cm, maximum gradient strength=500 mT/m, and peak slew rate=3000 T/m/sec) and a solenoid radiofrequency coil (4cm in length and 3cm in diameter). During scanning, anesthesia was induced and maintained with isofluorane (2% in oxygen to induce and 1.5% in oxygen to maintain) using a nose cone with vacuum for scavenging. Mice were placed on a custom-built plastic sled for secure positioning. The lower part of the body and tail of the mice were wrapped using gauze to maintain body temperature.

Mice were scanned using the 3D fast imaging employing steady state acquisition (3D-FIESTA; GE Medical Systems, Milwaukee, WI, USA) pulse sequence. The imaging parameters were: repetition time (TR) = 4.2 ms, echo time (TE) = 2.1 ms, flip angle = 20°, bandwidth = 62.5 kHz, 200 μm^3 isotropic resolution over a 6cm FOV, 8 RF phase cycles and 1 signal average. These are optimal parameters determined from previous work in our lab and protocol optimization steps which are shown in Appendix 1. Acquisition time was 21 minutes. Animals were scanned 24-48 hours prior to the injection of cells and 48 hours after the injection. All mice were sacrificed after the last imaging session.

2.2.4. MR Image Analysis

In order to assess the migration of MPIO-labeled DC to the draining popliteal lymph nodes, the volume of popliteal lymph nodes, the volume of the region of the signal loss, and the fractional signal loss in the nodes were measured from MR images. The measurements were performed using the imaging software VGStudio Max 1.2 (Heidelberg, Germany). The volume of each lymph node was measured by performing a manual segmentation of each lymph node image slice. In order to separate the lymph node from the surrounding adipose tissue, a threshold value was applied to the 3D region of interest (ROI). The value of the threshold was determined in the range of the lymph node signal intensity. The volume of signal void within the lymph node was measured by the application of an additional threshold value enabling the segregation of voxels with low signal intensity value (discrete or clustered "signal voids" in FIESTA images due to the presence of MPIO-labeled cells). Void volume was calculated as the sum of all voxels residing in the 3D segmentation and matching the threshold criteria. Fractional signal loss was used to assess the signal loss due to presence of MPIO-labeled DC. Fractional signal loss was defined as:

$$\Delta S/S = (S - S_{void})/S$$

where S_{void} is the minimum signal intensity value from the central voxels of the void observed in the left popliteal lymph node and S is the average signal intensity value from the contralateral lymph node.

2.2.5. Tissue Histology and Microscopy

After imaging, mice were euthanized by CO_2 inhalation and the popliteal lymph nodes were removed. Lymph nodes were fixed using 10% formaldehyde in PBS at 4% overnight. Cryoprotection of lymph nodes was performed by sequential incubation (24 hours) in increasing concentrations of sucrose in PBS (10%, 20% and 30%). For sectioning, lymph nodes were embedded in OCT compound (Sakura Finetek, Torrance CA) and snap frozen using dry ice. The entire node was cryosectioned into 16μm sections using a cryostat at a chamber and object temperature of $-20^{\circ}C$. Serial sections were placed on collagen coated glass slides. Sections were subsequently studied with fluorescence microscopy for the presence of green PKH+ DC and flash red MPIO particles. Each section was examined first, with the EGFP channel (excitation: 470/40 nm emission: 525/50 nm) to detect and localize green PKH+ DC and second, with the Texas red channel (excitation: 530-585 nm, emission: 615 nm) to detect MPIO particles. Digital images were collected using a Zeiss Axioimager fluorescence microscope equipped with a Qimaging Retiga Exi_color video camera.

Digital images were imported to ImageJ 1.42q software, an image processing and analysis software, to quantify the area of green PKH and the area of flash red fluorescence per area of lymph node. For each lymph node, approximately every fifth section was measured, providing a total of 10–14 sections. The area of fluorescence per area of lymph node was reported as the mean ± standard error of the mean (SEM).

2.2.6. Statistical Analysis

Results of measurements were reported as the mean ± SEM. Statistical comparison was based on the Student t test or repeated measures two-way analysis of variance (ANOVA). A Spearman's rank correlation analysis was used to determine the direction and strength of relationships between two different variables.

2.3. Results

2.3.1. MPIO labeling and DC viability

The cellular iron content measured by ICP-MS was 13.7 pg Fe/cell for MPIO-labeled DC and 0.63 pg Fe/cell for unlabeled DC. Figure 2.1 shows microscopic images of unlabeled and MPIO-labeled DC. Bright-field microscopy and fluorescence microscopy of labeled cells confirmed the intracellular labeling of DC with 0.90 μm flash red MPIO particles (Figure 2.1A and 2.1B). Comparison of fluorescent image with light microscopy image verified that dark brown particles were flash red MPIO particles. Figure 2.1C and 2.1D are the images of unlabeled DC and MPIO-labeled DC respectively, stained with PPB and eosin.

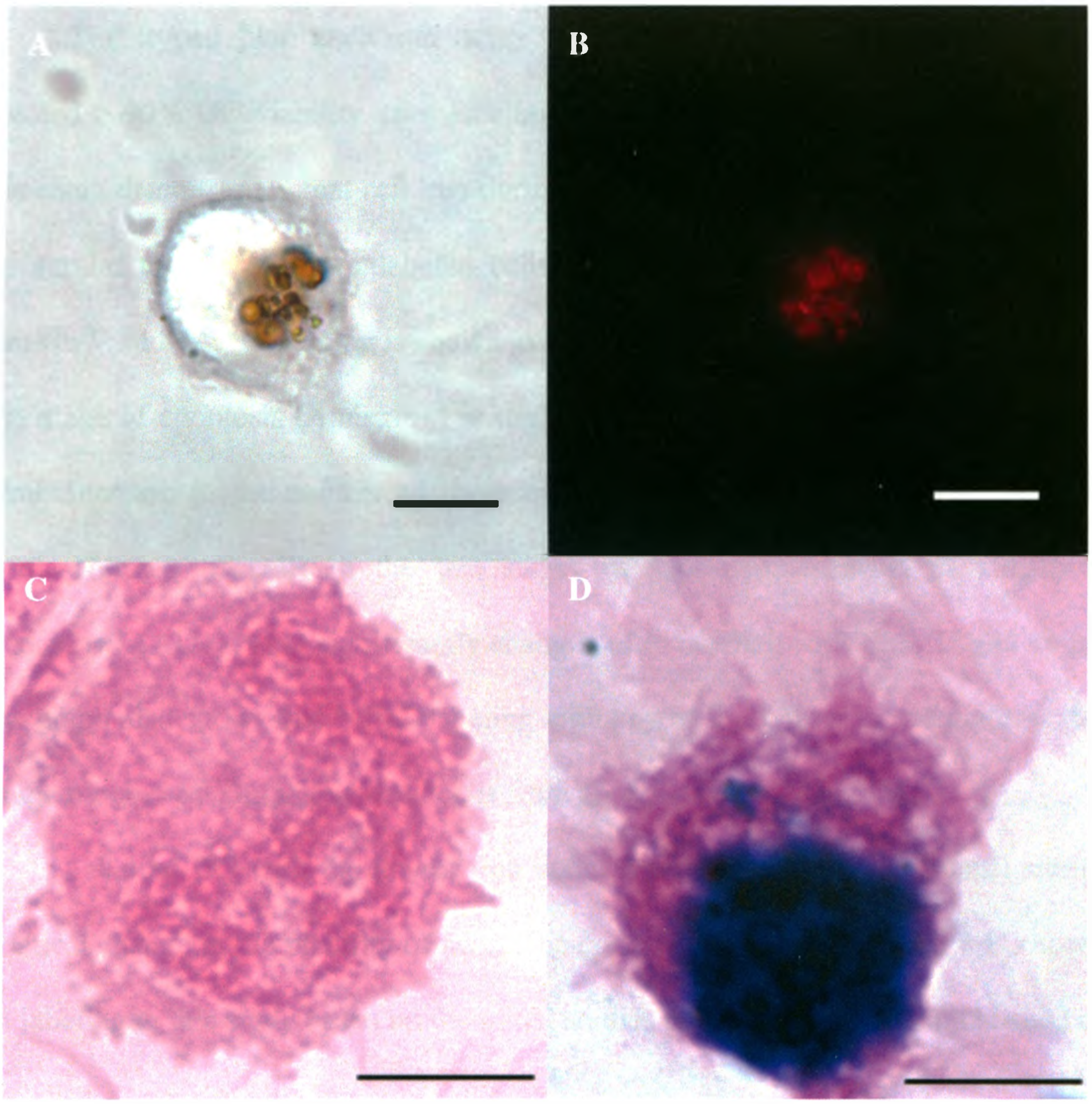

Figure 2.1. **Efficient uptake of MPIO particles by mouse DC**. Bright-field microscopic image (A) and red fluorescent image (B) of a DC labeled with 0.9 µm flash red MPIO. Unlabeled DC (C) and MPIO-labeled DC (D) stained with PPB and eosin. Magnification = 100x Scale bar = 10 µm.

The trypan blue exclusion assay for three different concentrations of MPIO revealed > 90% DC viability after labeling with 12.5, 25 and 50 µg/ml (Figure 2.2A). This result demonstrated that cell loss during labeling with these concentrations of MPIO was similar to that of the unlabeled cells. The result of flow cytometric analysis of Annexin V and 7AAD staining is shown in Figure 2.2B. The percentage of the cells in the early stage of apoptosis (Annexin+) is slightly increased after labeling with 12.5 and 25 µg/ml. Increase in the number of these cells is more dominant after labeling with 50 µg/ml. Number of cells in the late stages of apoptosis, necrosis or already dead (Annexin+7AAD+) is not significantly changed after labeling with 12.5, 25 and 50 µg/ml. This graph also shows that MPIO labeling with any of these three concentrations did not change number of completely dead cells from apoptosis or necrosis (7AAD+).

Labeling DC with the lowest iron concentrations (12.5 and 25 µg/ml) caused no statistical change in the viability of cells. The concentration of 12.5 µg/ml was chosen for cell labeling in this study based on the initial studies by Bradly Shrum (unpublished data).

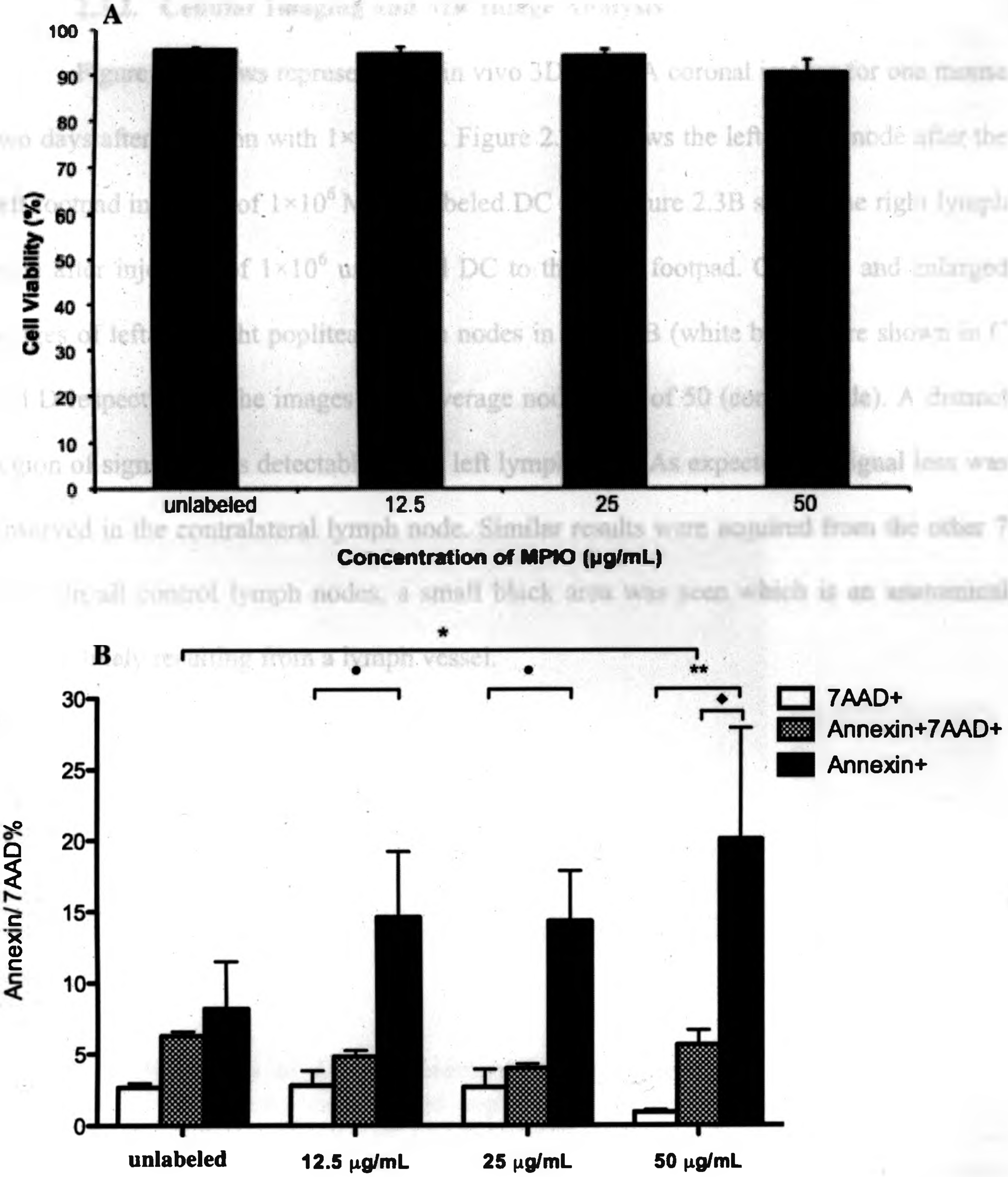

Figure 2.2. **DC viability after labeling with MPIO.** Trypan blue exclusion assay (A) and Annexin V/ 7AAD flow cytometric analysis (B) of unlabeled DC and MPIO-labeled DC with three concentrations. Data are mean of 3 independent experiments ± SEM. (◆P<0.05 for Annexin+7AAD+ vs. Annexin+ in 50µg/mL, •P<0.05 for 7AAD+ vs. Annexin+ in 12.5 and 25µg/mL, **P<0.01 for 7AAD+ vs. Annexin+ in 50µg/mL, *P<0.05 for control (0µg/mL) vs. 50µg/mL)

2.3.2. Cellular Imaging and MR Image Analysis

Figure 2.3 shows representative in vivo 3DFIESTA coronal images for one mouse two days after injection with 1×10^6 DC. Figure 2.3A shows the left lymph node after the left footpad injection of 1×10^6 MPIO-labeled DC and Figure 2.3B shows the right lymph node after injection of 1×10^6 unlabeled DC to the right footpad. Cropped and enlarged images of left and right popliteal lymph nodes in A and B (white boxes) are shown in C and D respectively. The images have average node SNR of 50 (control node). A distinct region of signal loss is detectable in the left lymph node. As expected, no signal loss was observed in the contralateral lymph node. Similar results were acquired from the other 7 mice. In all control lymph nodes, a small black area was seen which is an anatomical feature, likely resulting from a lymph vessel.

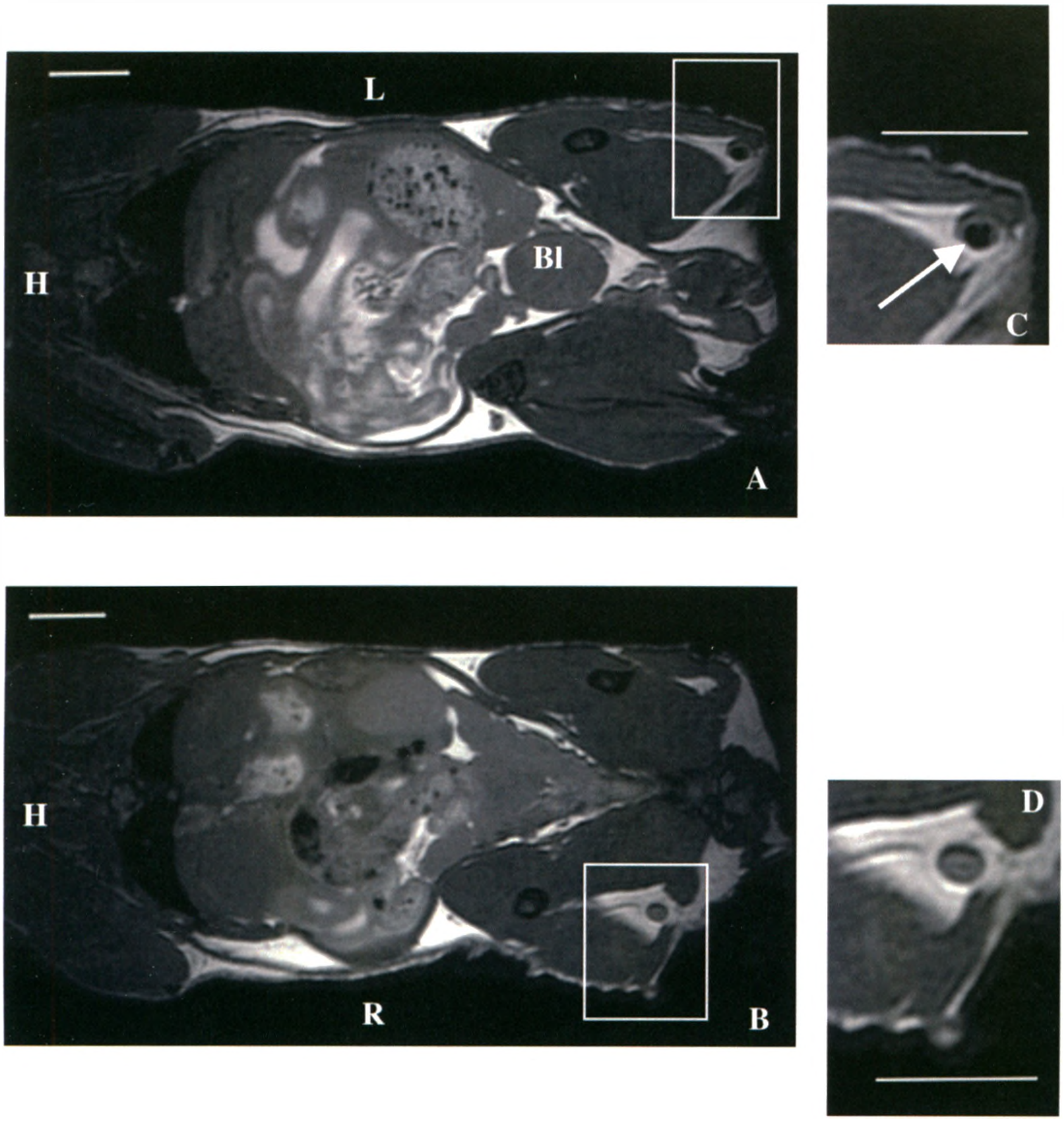

Figure 2.3. **Migration of DC is detectable by cellular MRI.** Coronal 3DFIESTA images (200x200x200μm) showing the popliteal lymph nodes from one representative mouse, two days after injection with (A) 1×10^6 MPIO-labeled DC or (B) 1×10^6 unlabeled DC. (C&D) Cropped and enlarged images of popliteal lymph nodes in A&B (white boxes). Arrow indicates the region of signal loss within the left lymph node.
Bl =Bladder, H=Head, L=left, R=right. Images are representative of n = 8. Scale bar = 0.5 cm.

As shown in Figure 2.4, the size of the region of signal loss in the draining lymph node is dose dependent. Figure 2.4 shows representative in vivo 3DFIESTA coronal images for mice at pre- and 2 days post-injection with 1×10^6 or 0.1×10^6 MPIO-labeled DC. The images of the left popliteal lymph node before and 2 days after injection of 1×10^6 MPIO-labeled DC are shown in Figures 2.4A and 2.4B (cropped and enlarged in E and F). Figures 2.4C and 2.4D show left popliteal lymph node of a mouse before and 2 days after injection of 0.1×10^6 MPIO-labeled DC (cropped and enlarged in G and H). The signal loss observed in the draining lymph node was significantly greater after injection of 1×10^6 MPIO-labeled DC compared with injection of 0.1×10^6 MPIO-labeled DC. The region of signal loss covered most of the left lymph node following injection of 1×10^6 MPIO-labeled DC and this was similar for all mice injected with this cell number. However, of the 8 mice injected with 0.1×10^6 MPIO-labeled DC, signal loss was only obvious in the node of one animal (shown in Figure 2.4D).

Figure 2.4. **Signal loss in MR images is different for different numbers of injected MPIO-labeled DC.** Coronal 3DFIESTA images (200x200x200µm) showing the popliteal lymph nodes from two representative mice before (A) and two days after (B) injection with $1\text{x}10^6$ MPIO-labeled DC or before (C) and 2 days after (D) injection with $0.1\text{x}10^6$ MPIO labeled DC. (E&F and G&H) Cropped and enlarged images of popliteal lymph nodes in A&B and D&D (white boxes). Arrows indicate the region of signal loss within the left lymph nodes.
Bl =Bladder, H=Head, L=left, R=right. Images are representative of n = 16. Scale bar = 0.5 cm.

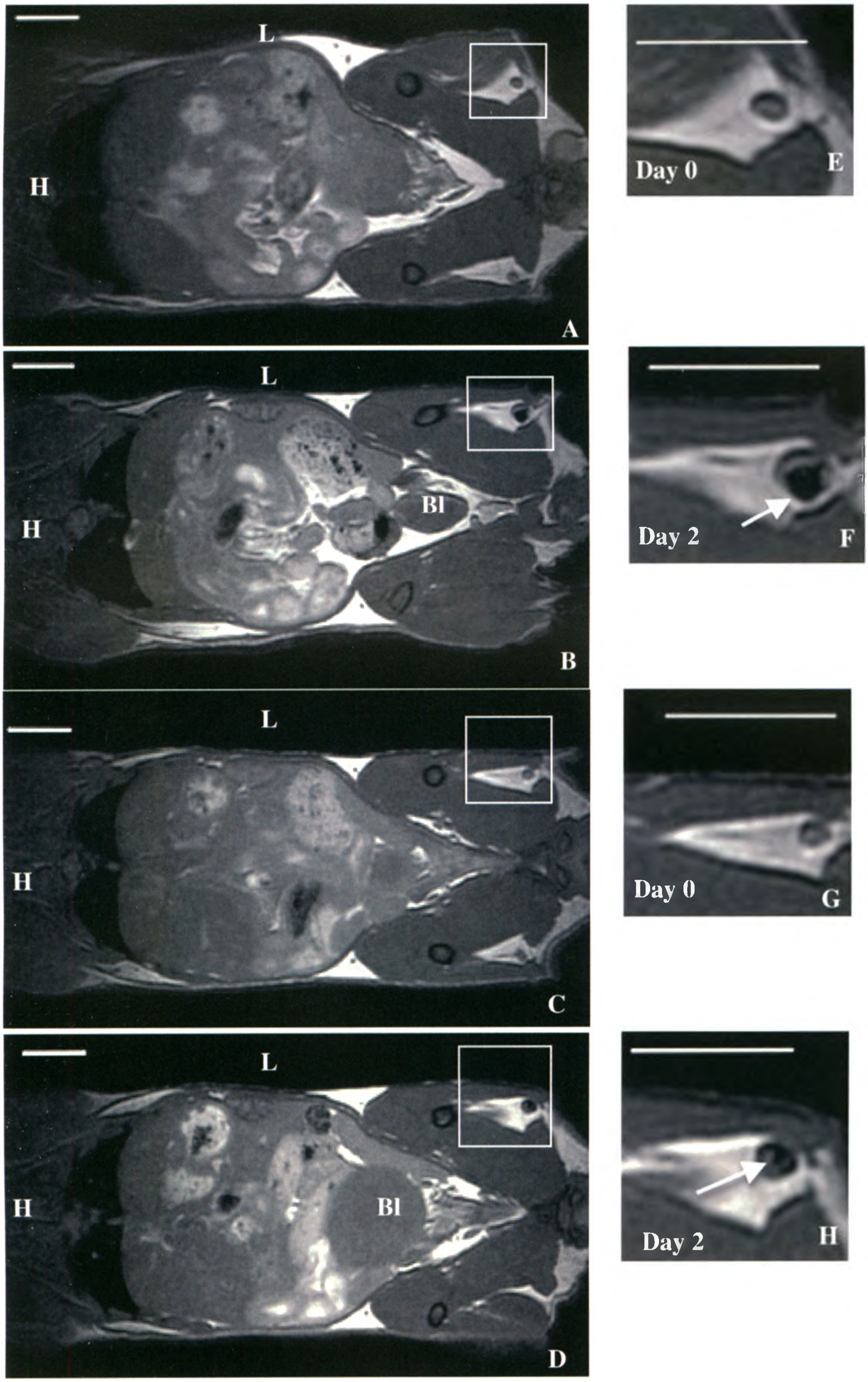
L
H
A
Day 0
E
L
Bl
H
B
Day 2
F
L
H
C
Day 0
G
L
Bl
H
D
Day 2
H

The lymph node volumes are shown in Figure 2.5. At 2 days post-injection, the volume of the popliteal lymph nodes was increased in all mice injected with 1×10^6 cells, whether cells were MPIO-labeled or unlabeled. The average volume of normal lymph node was 0.6 mm^3 and the average lymph node volume at 2 days after injection of 1×10^6 DC was approximately 2 mm^3 (1.4 mm^3 increase in lymph node volume). There was also an increase in the volume of lymph node following injection of the lower dose (0.1×10^6 cells). No significant difference was found in node volume after injection of unlabeled versus MPIO labeled DC but there was a significant difference between two doses of cells ($0.1x10^6$ vs. $1x10^6$ cells).

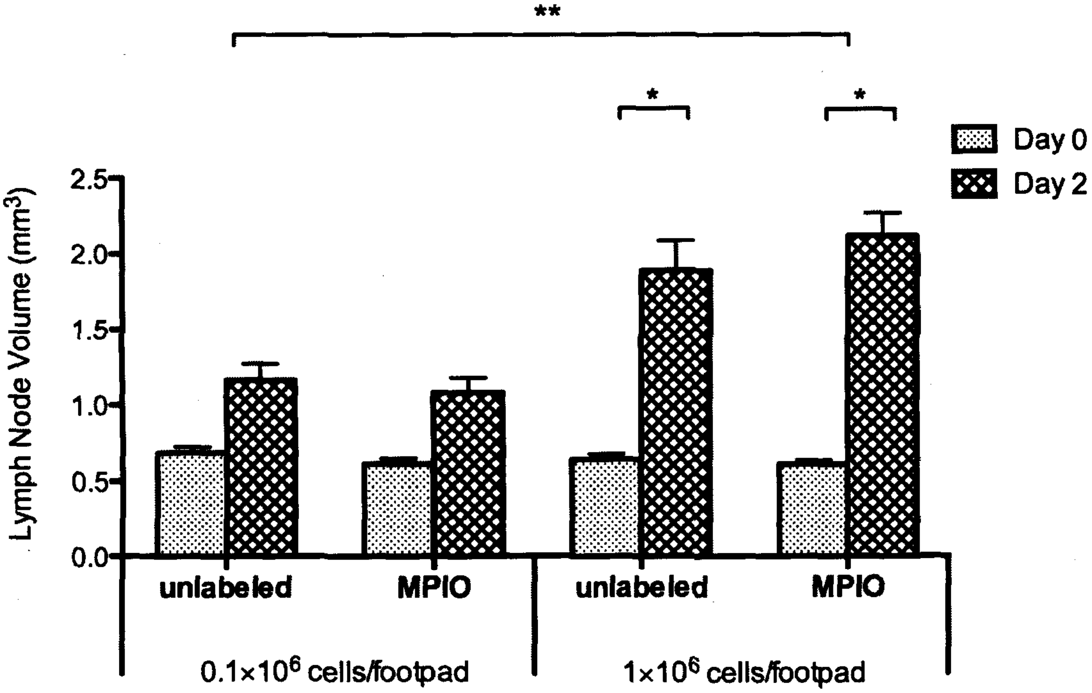

Figure 2.5. **Quantification of Lymph node volume from images acquired at pre-injection and two days after DC injection.** Horizontal bars represent mean values ±SEM. (n = 8, *$P<0.01$ Day 2 vs. Day 0, **$P<0.001$ for $1x10^6$ vs. $0.1x10^6$ cells/footpad).

The results of void volume and fractional signal loss measurement are summarized in tables 2.1 and 2.2 respectively. These tables show the results from mice injected with 1×10^6 MPIO-labeled DC. As mentioned above, detectable signal loss was only observed in 1 out of 8 mice following injection of 0.1×10^6 MPIO-labeled DC so, the analysis of signal void volume and fractional signal loss was not possible. The mean fractional signal loss was 90% in the lymph nodes on the side injected with MPIO-labeled cells. The mean signal void volume in the popliteal lymph nodes was 1.33 mm^3 after the injection of 1×10^6 MPIO-labeled DC. Therefore, 64% of the volume of the draining lymph node measured from MR images was occupied by the signal void caused by MPIO-labeled DC.

Signal Void Volume (mm^3)	
Mean	1.331
Standard Deviation	0.493
Median	1.3195
Standard Error	0.174

Table 2.1. **Results of signal void volume in popliteal lymph nodes after injection of 1×10^6 MPIO-labeled DC**

Fractional Signal Loss	
Mean	90%
Standard Deviation	4%
Median	92%
Standard Error	1%

Table 2.2. **Results of fractional signal loss in popliteal lymph nodes after injection of 1×10^6 MPIO-labeled DC**

2.3.3. Histology

Figure 2.6 presents representative fluorescent images of PKH+ DC in the lymph nodes 2 days after the injection of unlabeled or MPIO-labeled DC. Figures 2.6A and 2.6B show the distribution of 1×10^6 unlabeled or MPIO-labeled DC respectively in the left and right popliteal lymph nodes. PKH+ DC were mostly located in the deep cortex of lymph nodes whether MPIO-labeled or unlabeled. However, it was observed that the amount of DC in the draining lymph node were greater after injection of unlabeled DC compared to MPIO-labeled DC. Sections of right (C) and left (D) lymph nodes of a representative mouse injected with 0.1×10^6 unlabeled or MPIO-labeled DC also show that DC were distributed in the central part of lymph nodes. The amount of DC in the lymph nodes following injection of 1×10^6 cells is considerably higher than the amount of DC in the lymph nodes after injection of 0.1×10^6 cells.

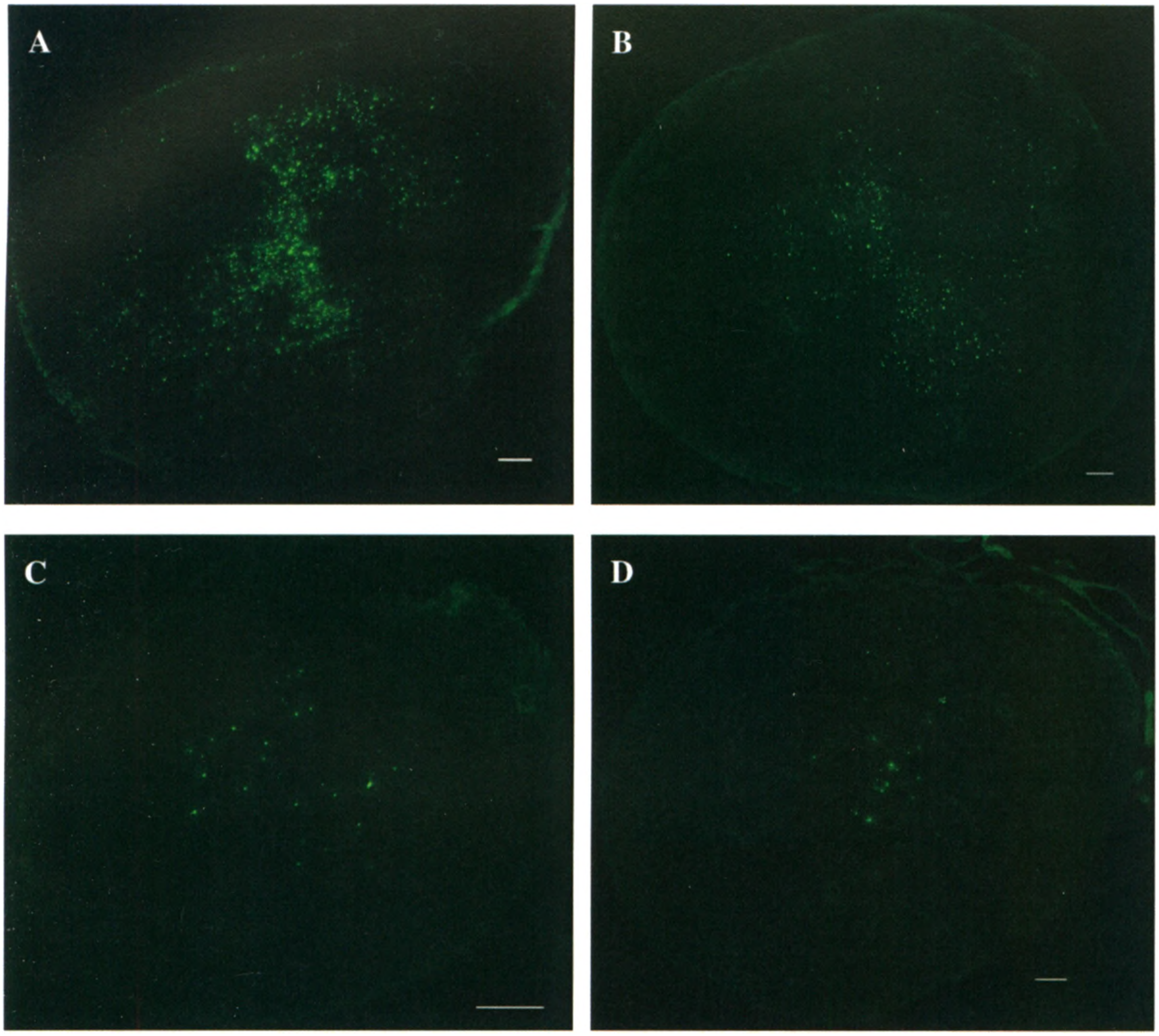

Figure 2.6. **Distribution of green PKH fluorescence in popliteal lymph nodes.** Distribution of green PKH fluorescence in popliteal lymph nodes two days after injection of (A) 1×10^6 unlabeled DC, (B) 1×10^6 MPIO-labeled DC, (C) 0.1×10^6 unlabeled DC or (D) 0.1×10^6 MPIO-labeled DC. The green fluorescence regions correspond the presence of PKH+ DC. Scale bar = 100 µm.

Fluorescence microscopy revealed that the distribution of green PKH+ DC was similar to the distribution of flash red MPIO particles in the left lymph node (Figure 2.7). As shown in Figure 2.7A, green PKH fluorescence that corresponds to PKH+ DC was mainly distributed in the central part of the lymph node. Flash red fluorescence that corresponds to MPIO particles had the same distribution pattern as green PKH (Figure 2.7B) and little difference was observed between the amount of green and red fluorescence. Figures 2.7A and 2.7B are representative images of $n = 4$ mice. The same results were obtained from the other lymph nodes.

The area of green PKH per area of lymph node measured for both right (control) and left (MPIO) lymph nodes are shown in Figure 2.7C. The area of green PKH fluorescence after injection of 1×10^6 DC was significantly greater, 10-fold, than the area of green PKH after injection of 0.1×10^6 DC. There was a significant difference between the area of green PKH after injection of 1×10^6 unlabeled DC and area of green PKH after injection of 1×10^6 MPIO-labeled DC. The area of fluorescence was significantly greater for unlabeled DC compared with MPIO-labeled DC. In contrast, no significant difference was found between the area of PKH following injection of 0.1×10^6 MPIO-labeled and unlabeled DC.

The area of flash red per area of lymph node measured for left (MPIO) lymph nodes is shown in Figure 2.7D. The area of flash red MPIO per left lymph node was also significantly greater, 10-fold, after injection of 1×10^6 MPIO-labeled DC compared with 0.1×10^6 MPIO-labeled DC. Spearman rank correlation analysis showed a strong positive correlation between the amount of green PKH fluorescence and the amount of flash red fluorescence in the left draining lymph nodes ($R^2 = 0.928$, Figure 2.7E).

Superposed images of green PKH and flash red MPIO in sections of left lymph nodes of mice injected with 1×10^6 cells demonstrate that the regions of green PKH and regions of flash red are in agreement with each other (Figure 2.7F). Figure 2.7G shows green PKH fluorescence in a section of right popliteal lymph node of a representative mouse injected with 1×10^6 cells. The section is counterstained with DAPI. The difference between the amount of green PKH in the right and left lymph nodes after injection of 1×10^6 PKH+ DC is clearly noticeable in Figures 2.7F and 2.7G. More representative fluorescent images are provided in Appendix 2.

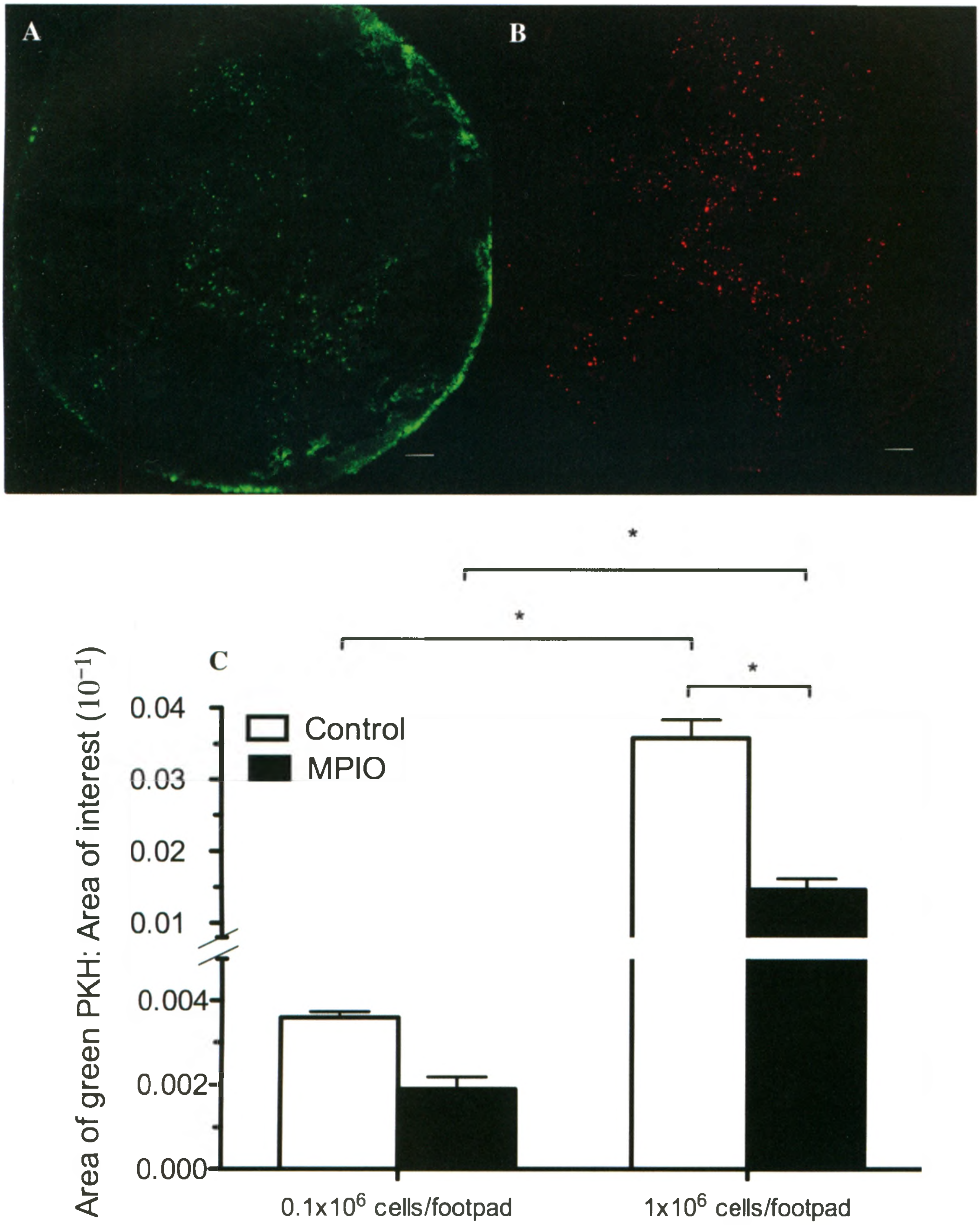
A
B
C
*
*
*
Control
MPIO
Area of green PKH: Area of interest (10^{-1})
0.04
0.03
0.02
0.01
0.004
0.002
0.000
$0.1x10^6$ cells/footpad
$1x10^6$ cells/footpad

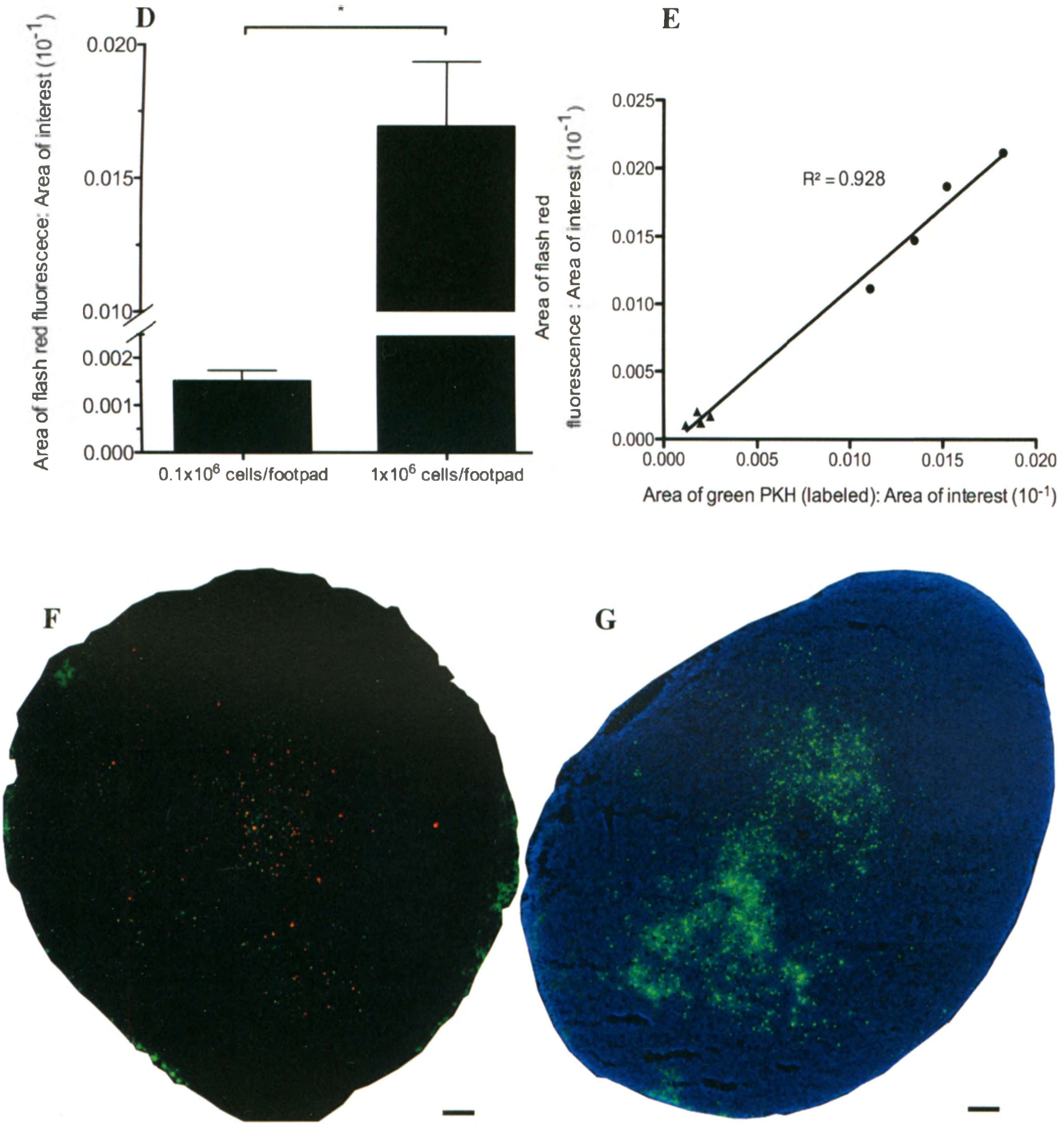

Figure 2.7. **Distribution of green PKH+ DC and flash red MPIO in popliteal lymph nodes 2 days after the injection of DC.** Distribution of green PKH+ DC in left lymph node (A) is consistent with the distribution of flash red MPIO particles (B). The area of green PKH fluorescence (C) and flash red fluorescence (D) were measured by digital morphometry. Data are mean ± SEM (n = 4, $^*P<0.05$). There is a strong positive correlation between amount of green PKH fluorescence and amount of flash red fluorescence in the left lymph node. ($R^2 = 0.928$) (E) (▲ data point for 0.1×10^6 cells/footpad, • data point for 1×10^6 cells/footpad). (F) Overlaid fluorescent images of green PKH+ DC and flash red MPIO in the left popliteal lymph node. (G) green PKH+ DC in a section of right popliteal lymph node of the same mouse counterstained with DAPI. Scale bar = 100 μm.

2.4. Discussion

This study presents the first report of in vivo tracking of MPIO-labeled DC using cellular MRI. Previously we have demonstrated the use of a specialized cellular imaging system for the in vivo detection of iron-labeled cells, including SPIO-labeled DC (9,19-21). This system includes a custom-built, high-performance gradient coil insert used with a clinical 1.5 or 3T MRI system running the 3D fast imaging employing steady state acquisition (FIESTA) pulse sequence with RF phase cycling. The FIESTA pulse sequence provides high SNR in short scan times and is very sensitive to the local magnetic field inhomogeneities caused by iron particles. This imaging strategy has allowed us to acquire high SNR images of the mouse whole body with clearly visible regions of signal loss in lymph nodes in less than 25 minutes.

A few groups have reported the use of SPIO particles to label and track DC in vitro and in vivo. In one of the early studies, ultra-small SPIO particles were used to label mouse DC (10). In this study, labeled DC were detected at the site of injection after intramuscular administration in spin-echo images on a 11.7 T MRI scanner. However, no DC were detected in the draining lymph nodes.

Three groups have shown that migration of SPIO-labeled DC to draining lymph nodes in mice can be detected by MRI (9,11,12). Baumjohann et al. were first to demonstrate this in 2006. In this study DC were labeled with SPIO and protamine sulfate and their migration to the draining lymph nodes in mice was imaged at 4.7 T (11). In 2009 our lab showed that migration of SPIO-labeled DC can be tracked in vivo using the FIESTA pulse sequence on 1.5T clinical scanner (9). We presented a quantitative approach to assess DC migration and a strong correlation was found between the signal loss in MR images and the presence of DC in nodes.

SPIO particles also have been used for labeling human DC (7). This study was conducted in the Netherlands. Autologous DC were labeled with SPIO and were injected intranodally in melanoma patients under ultrasound guidance. Imaging was performed using a gradient echo sequence on a 3T clinical MRI scanner. MRI allowed assessment of the accuracy of DC delivery and visualization of the migration of DC between adjacent or paired nodes.

This current study uniquely investigated the use of MPIO particles to label and track DC in vivo. MPIO is used less often than SPIO for cellular MRI. It has been used mainly for tracking cancer and stem cells in preclinical models (13-18). MPIO are the largest of the iron-based MRI contrast agents and contain the largest amounts of iron. While millions of SPIO particles are necessary within a cell for its detection, the higher iron content of MPIO enables the detection of cells labeled with even a single MPIO particle (17).

Labeling DC with MPIO was achieved simply by incubating cells with the particles. Results of the trypan blue exclusion assay showed that the tolerance of MPIO by DC was high (~95% survival). Flow cytometric analysis of Annexin V and 7AAD staining revealed that MPIO labeling with 12.5μg/mL of iron had no significant effect on the number of cells undergoing apoptosis/necrosis.

One of the important advantages of MPIO over SPIO is the fluorescent tag embedded in the coating of MPIO particles. These tags, which are available in a variety of fluorescent dyes, facilitate the direct detection of MPIO particles using fluorescence microscopy. We used this feature, as well as PPB and eosin staining, to verify the intracellular uptake of MPIO by DC. Within DC the MPIO particles are located in the cytoplasm.

Our imaging approach resulted in the generation of high quality whole mouse body images in 3D in less than 30 minutes. Our immediate goal was to visualize the popliteal lymph nodes which were easily detected in the surrounding fat pad in spite of their small size. Along with the popliteal nodes, many other lymph nodes were visible.

In mice injected with 1×10^6 MPIO-labeled DC an obvious region of signal void was present in the popliteal lymph node in all mice. The analysis of MR images revealed an increase in the volume of the lymph node after the injection of DC. This was true whether MPIO-labeled or unlabeled DC were injected. An increase in the node volume suggests that cell proliferation has occurred and in this case implies that DC have stimulated T cell activation and proliferation. The fact that there was no significant difference in the way MPIO-labeled or unlabeled DC changed the size of the lymph node suggests that there is no difference in the stimulatory ability of labeled and unlabeled cells. The volume increase was much greater when the higher DC dose was administered. Since we know from our fluorescence microscopy that greater numbers of DC migrate to the node after the higher DC dose, this observation provides additional evidence that when a larger number of DC migrate to the node a greater T cell activation occurs.

The red fluorescence of the MPIO particles used in this study enabled the direct visualization of iron particles in the lymph nodes and allowed for comparisons between the presence and location of MPIO and PKH+ DC. The strong positive correlation between the area of green PKH and flash red showed that the majority of DC located in the draining lymph nodes are MPIO-labeled DC.

Although we also used GFP+ donor DC in these studies the fluorescence microscopy was only performed on the nodes from mice that were injected with PKH+ DC. This was because during our early attempts to visualize the GFP+ DC we had issues with autofluorescence and a weak GFP signal. In addition, a decision was made midway through this research project to move away from using GFP+ donor DC because of the possibility of immune response against GFP. Since GFP is a foreign antigen for the wildtype recipient mice, their immune system will likely produce immune response against GFP+ DC.

Of interest, our measurements of changes in lymph node volume were performed in all mice and showed that the volume of the lymph node increased to the same extent whether mice received GFP+ DC or PKH+ DC.

A very important observation made from the fluorescence microscopy was that there is a significant difference between the migration of MPIO-labeled DC and unlabeled DC, indicating that DC migration is reduced after MPIO labeling. The same observation has been made with SPIO-labeled DC (DeChickera et al., unpublished). Since our in vitro assays of cell viability did not reveal substantial negative effects of labeling with MPIO there is a need for further more specific assays of cell function to shed light on the cause of reduced migration of MPIO-labeled DC.

Sensitive and non-invasive imaging techniques are key to gaining important information about the fate of DC-based vaccines *in vivo* and will facilitate the development of effective DC-based immunotherapies for the generation of potent, antitumour immunity. The techniques developed in our lab for tracking of MPIO-labeled DC in the mouse lymphatic system should be of value for the evaluation of new strategies for DC immunotherapy. For example, cellular MRI can be used to determine if the state of DC maturation, the type of DC, the site of injection, or multiple infusions influence DC migration.

2.5. References

1. Banchereau J, Steinman RM, Dendritic cell and the control of immunity. Nature. 1998 Mar 19; 392(6673): 245-52.

2. Shortman K, Caux C, Dendritic cell development: multiple pathways to nature's adjuvants. Stem Cells. 1997. 15(6): 409-19.

3. Ridgway D. The first 1000 dendritic cell vaccinees. Cancer Invest. 2003; 21(6):873-86.

4. Steinman RM, Banchereau J. Taking dendritic cells into medicine. Nature. 2007 Sep 27; 449(7161):419-26.

5. Aarntzen EH, Figdor CG, Adema GJ, Punt CJ, de Vries IJ. Dendritic cell vaccination and immune monitoring. Cancer Immunol Immunother. 2008 Oct;57(10):1559-68.

6. Martin-Fontecha A, Sebastiani S, Höpken UE, Uguccioni M, Lipp M, Lanzavecchia A, Sallusto F. Regulation of dendritic cell migration to the draining lymph node: impact on T lymphocyte traffic and priming. J Exp Med. 2003 Aug 18;198(4):615-21.

7. de Vries IJ, Lesterhuis WJ, Barentsz JO, Verdijk P, van Krieken JH, Boerman OC, Oyen WJ, Bonenkamp JJ, Boezeman JB, Adema GJ, Bulte JW, Scheenen TW, Punt CJ, Heerschap A, Figdor CG. Magnetic resonance tracking of dendritic cells in melanoma patients for monitoring of cellular therapy. Nat Biotechnol. 2005 Nov;23(11):1407-13.

8. Verdijk P, Scheenen TW, Lesterhuis WJ, Gambarota G, Veltien AA, Walczak P, Scharenborg NM, Bulte JW, Punt CJ, Heerschap A, Figdor CG, de Vries IJ. Sensitivity of magnetic resonance imaging of dendritic cells for in vivo tracking of cellular cancer vaccines. Int J Cancer. 2006 Mar 1;120(5):978-84.

9. Dekaban GA, Snir J, Shrum B, de Chickera S, Willert C, Merrill M, Said EA, Sekaly RP, Foster PJ, O'Connell PJ. Semiquantitation of mouse dendritic cell migration in vivo using cellular MRI. J Immunother. 2009 Apr;32(3):240-51.

10. Ahrens ET, Feili-Hariri M, Xu H, Genove G, Morel PA. Receptor-mediated endocytosis of iron-oxide particles provides efficient labeling of dendritic cells for in vivo MR imaging. Magn Reson Med. 2003 Jun;49(6):1006-13.

11. Long CM, van Laarhoven HW, Bulte JW, Levitsky HI. Magnetovaccination as a novel method to assess and quantify dendritic cell tumor antigen capture and delivery to lymph nodes. Cancer Res. 2009 Apr 1;69(7):3180-7.

12. Baumjohann D, Hess A, Budinsky L, Brune K, Schuler G, Lutz MB. In vivo magnetic resonance imaging of dendritic cell migration into the draining lymph nodes of mice. Eur J Immunol. 2006 Sep;36(9):2544-55.

13. Williams JB, Ye Q, Hitchens TK, Kaufman CL, Ho C. MRI detection of macrophages labeled using micrometer-sized iron oxide particles. J Magn Reson Imaging. 2007 Jun;25(6):1210-8.

14. Foley LM, Hitchens TK, Ho C, Janesko-Feldman KL, Melick JA, Bayır H, Kochanek PM. Magnetic Resonance Imaging Assessment of Macrophage Accumulation in Mouse Brain after Experimental Traumatic Brain Injury. J Neurotrauma. 2009 Sep;26(9):1509-1519.

15. Shapiro EM, Medford-Davis LN, Fahmy TM, Dunbar CE, Koretsky AP. Antibody-mediated cell labeling of peripheral T cells with micron-sized iron oxide particles (MPIOs) allows single cell detection by MRI. Contrast Media Mol Imaging. 2007 May;2(3):147-53.

16. Bernas LM, Foster PJ, Rutt BK. Magnetic resonance imaging of in vitro glioma cell invasion. J Neurosurg. 2007 Feb;106(2):306-13.

17. Shapiro EM, Skrtic S, Sharer K, Hill JM, Dunbar CE, Koretsky AP. MRI detection of single particles for cellular imaging. Proc Natl Acad Sci U S A. 2004 Jul 27;101(30):10901-6.

18. Hinds KA, Hill JM, Shapiro EM, Laukkanen MO, Silva AC, Combs CA, Varney TR, Balaban RS, Koretsky AP, Dunbar CE. Highly efficient endosomal labeling of progenitor and stem cells with large magnetic particles allows magnetic resonance imaging of single cells. Blood, 2003. 102(3): p. 867-72.

19. Heyn C, Ronald JA, Mackenzie LT, MacDonald IC, Chambers AF, Rutt BK, Foster PJ. In vivo magnetic resonance imaging of single cells in mouse brain with optical validation. Magn Reson Med. 2006 Jan;55(1):23-9.

20. Gonzalez-Lara LE, Xu X, Hofstetrova K, Pniak A, Brown A, Foster PJ. In vivo magnetic resonance imaging of spinal cord injury in the mouse. J Neurotrauma. 2009 May;26(5):753-62.

21. Bernas LM, Foster PJ, Rutt BK. Magnetic resonance imaging of in vitro glioma cell invasion. J Neurosurg. 2007 Feb;106(2):306-13.

22. de Vries IJ, Krooshoop DJ, Scharenborg NM, Lesterhuis WJ, Diepstra JH, Van Muijen GN, Strijk SP, Ruers TJ, Boerman OC, Oyen WJ, Adema GJ, Punt CJ, Figdor CG. Effective migration of antigen-pulsed dendritic cells to lymph nodes in melanoma patients is determined by their maturation state. Cancer Res. 2003 Jan 1;63(1):12-7.

Chapter 3: Monitoring the Fate of MPIO-labeled DC in the Mouse Body using Cellular MRI

Work presented in this chapter was done in collaboration with Dr. Greogory Dekaban. DC isolation, iron labeling and injection were performed by Christy Willert. Yuhua Chen, lab manager of Foster group performed cryosectioning of lymph nodes. Development of the custom gradient insert coil and radiofrequency coils used in this project was completed in Dr. Rutt's Lab. Inter- and Intra-observer variability assessment was done based on measurements performed by Anthony Prom. All other procedures including MR acquisition, mouse anesthesia, data analysis, tissue dissection and preparation for microscopy and fluorescence microscopy were performed by Roja Rohani.

3.1. Introduction

A promising approach to cancer immunotherapy is the use of dendritic cells (DC) loaded with tumor antigens. DC are potent immune cells that initiate immune responses by activating resting T cells to infiltrate tumors and initiate tumor regression (1-3). Improved migration of DC to draining lymph nodes is crucial for efficient immune responses. Several groups have explored the use of cellular MRI to assess migration of DC in vivo. These studies have used superparamagnetic iron oxide particles (SPIO) to label and track DC with MRI (4, 5, 8, 10, 13). In Chapter 2, we show that DC can also be labeled with micron sized iron oxide (MPIO) particles for in vivo tracking by MRI. One of the advantages of MPIO particles is their higher iron content compared to SPIO particles. This may enable the MR detection of smaller numbers of cells or cells containing fewer particles (9, 10). This is of great importance considering that only small numbers of injected DC (≤3%) successfully migrate to draining lymph nodes and that DC tend to take up less iron in culture than many other adherent cell types (6-8).

Another important property of MPIO is that its polymer coating is not biodegradable, allowing it to persist longer in vivo than SPIO, which are dextran coated. This raises a critical question about how long signal loss will persist after the injection of MPIO-labeled DC and whether the MRI appearance of MPIO particles in vivo mimics the life span of DC. A study on the effects of route of administration and activation status on the migration of DC showed that the accumulation of fully activated DC in the lymph nodes peaks at 48 hours after subcutaneous injection and declines at 96 hours (11). This suggests a life span of 1-3 days for activated DC in vivo. In this chapter, we report on the longitudinal monitoring of MPIO-labeled DC in the mouse body after subcutaneous injection. We also evaluate the precision of the method for quantification of MR images of lymph nodes, by the assessment of inter- and intra-observer variability.

Our images show that signal loss caused by MPIO persists in the node for up to 7 days post injection. This observation is unexpected since the life span of DC in vivo is reported as 2-3 days. Fluorescence microscopy of the nodes at day 7 post DC injection showed a lack of correspondence between MPIO particles and DC; many more MPIO particles were observed compared with DC. These observations suggests that at least some of the signal loss observed in images at day 7 is due to free MPIO particles, rather than MPIO-labeled DC. Our results suggest that care should be taken when interpreting signal loss due to MPIO-labeled DC in draining lymph nodes past 2 days.

3.2. Methods

3.2.1. Animal Groups

All protocols in this study were accredited by the University of Western Ontario Animal Use Subcommittee and agreed with the guidelines of the Canadian Council on Animal Care.

Two experiments were performed with two groups of mice. In the first experiment, DC were acquired from enhanced green fluorescence protein (EGFP) (C57BL/6-Tg[ACTB-EGFP]10sb/J) C57Bl/6 mice. In this experiment, 0.1×10^6 or 1×10^6 EGFP+ MPIO-labeled DC were injected subcutaneously into the left hind footpad of recipient C57Bl/6 mice (n=8, n=4 for each cell dose) and the equivalent number of unlabeled DC were injected into the right hind footpad. In the second experiment, DC were obtained from wildtype C57Bl/6 mice (instead of EGFP+ mice) and green PKH (excitation:emission peaks, 490:502 nm) was used as the cell tracker. In this experiment, we used only the higher dose of cells. 1×10^6 PKH+ MPIO-labeled or unlabeled DC were injected subcutaneously to the hind footpad of C57Bl/6 mice (n=4). Before the injection, mice were anesthetized with the gas anesthetic isofluorane (Forane, Baxter) (1% in 100% oxygen) and injections were done with a 28-gauge needle.

3.2.2. Dendritic Cell Culture and MPIO Labeling

The bone marrow derived DC were collected as described in Chapter 2. DC were labeled by overnight incubation with 12.5 μg/ml MPIO (Bangs beads, Bangs Laboratories, Fisher, IN). MPIO were 0.90 μm in diameter and tagged with flash-red fluorescent agent (excitation:emission peaks, 660:690 nm). Cells were washed with ice-cold Hank's balance salt solution (HBSS, Invitrogen) with 0.1% bovine serum albumin

(BSA, Sigma) to ensure removal of unincorporated contrast agent. DC were further labeled with PKH67 Green Fluorescent cell linker as described in Chapter 2.

3.2.3. Cellular MR Imaging

Imaging was performed in vivo using a 3 Tesla (3T) GE whole-body MR scanner (MR Signa® Excite™, GE Healthcare, Milwaukee, WI, USA) with a custom-built gradient coil (inner diameter=17.5cm, maximum gradient strength=500 mT/m, and peak slew rate=3000 T/m/sec) and a solenoid radiofrequency coil (4cm in length and 3cm in diameter). During scanning, anesthesia was induced and maintained with isofluorane (2% in oxygen to induce and 1.5% in oxygen to maintain) using a nose cone with vacuum for scavenging. Mice were placed on a custom-built plastic sled for secure positioning. The lower part of the body and tail of the mice were wrapped using gauze to maintain body temperature.

Mice were scanned using the 3D fast imaging employing steady state acquisition (3D-FIESTA; GE Medical Systems, Milwaukee, WI, USA) pulse sequence. The imaging parameters were: repetition time (TR) = 4.2 ms, echo time (TE) = 2.1 ms, flip angle = 20°, bandwidth = 62.5 kHz, 200 μm^3 isotropic resolution over a 6cm FOV, 8 RF phase cycles and 1 signal average. Acquisition time was 21 minutes. Animals were scanned 24-48 hours prior to the injection of cells and 2, 3 and 7 days after the injection. All mice were sacrificed after the last imaging session.

3.2.4. MR Image Analysis

In order to assess the migration of MPIO-labeled DC to the draining popliteal lymph nodes, the volume of popliteal lymph nodes, the volume of the region of the signal loss, and the fractional signal loss in the nodes were measured. The measurements were performed using the imaging software VGStudio Max 1.2 (Heidelberg, Germany). The volume of each lymph node was measured by performing a manual segmentation of each lymph node image slice. In order to separate the lymph node from the surrounding adipose tissue, a threshold value was applied to the 3D region of interest (ROI). The value of the threshold was determined in the range of the lymph node signal intensity.

The volume of signal void within the lymph node was measured by the application of an additional threshold value enabling the segregation of voxels with low signal intensity value (discrete or clustered "signal voids" in FIESTA images due to the presence of MPIO-labeled cells). Void volume was calculated as the sum of all voxels residing in the 3D segmentation and matching the threshold criteria. Fractional signal loss was used to assess the signal loss due to presence of MPIO-labeled DC. Fractional signal loss was defined as:

$$\Delta S/S = (S - S_{void})/S$$

where S_{void} is the minimum signal intensity value from the central voxels of the void observed in the left popliteal lymph node and S is the average signal intensity value from the contralateral lymph node.

3.2.5. Tissue Histology and Microscopy

After the last imaging session, mice from the second experiment were euthanized by CO_2 inhalation and the popliteal lymph nodes were removed. Lymph nodes were fixed using 10% formaldehyde in PBS at 4% overnight. Cryoprotection of lymph nodes was performed by sequential incubation (24 hours) in increasing concentrations of sucrose in PBS (10%, 20% and 30%). For sectioning, lymph nodes were embedded in OCT compound (Sakura Finetek, Torrance CA) and snap frozen using dry ice. The entire node was cryosectioned into 16μm sections using a cryostat at a chamber and object temperature of -20°C. Serial sections were placed on collagen coated glass slides. Sections were subsequently studied with fluorescence microscopy for the presence of green PKH+ DC and flash red MPIO particles. Each section was examined first, with the EGFP channel (excitation: 470/40 nm emission: 525/50 nm) to detect and localize green PKH+ DC and second, with the Texas red channel (excitation: 530-585 nm, emission: 615 nm) to detect MPIO particles. Digital images were collected using a Zeiss Axioimager fluorescence microscope equipped with a Qimaging Retiga Exi_color camera.

3.2.6. Inter- and Intra-observer Variability Assessment

To evaluate inter-observer variability of the quantitative analysis of MR images, the lymph node volumes for both right and left popliteal lymph nodes of 8 mice were measured at 4 time points (pre-scan, day 2, day 3, day 7) by two observers. One observer was trained by the researcher and blinded to the mouse identity and time point. In total 64 measurements were done by each observer (8 mice × 2 lymph nodes × 4 time points). To evaluate intra-observer variability, the blinded observer repeated the measurements of the same data set in randomized order.

3.2.7. Statistical Analysis

Results of measurements were reported as the mean ± SEM. Statistical comparison was based on the Student t test or repeated measures two-way analysis of variance (ANOVA). GraphPad Prism version 5 (GraphPad Software Inc. 2009) was employed for linear regressions and Bland Altman analyses.

3.3. Results

3.3.1. Cellular Imaging and MR Image Analysis

Figure 3.1 shows representative in vivo 3DFIESTA coronal images for one mouse at seven days after injection with 1×10^6 unlabeled DC to the right footpad and 1×10^6 MPIO-labeled DC to the left footpad. Cropped and enlarged images of left and right popliteal lymph nodes in A (white boxes) are shown in B and C respectively. The images have average node SNR of 59 (control node). A large region of signal loss is detectable in the left lymph node. Similar results were acquired from the other 7 mice that were injected with 1×10^6 cells (n = 4 were PKH labeled and n = 4 were from GFP+ mice).

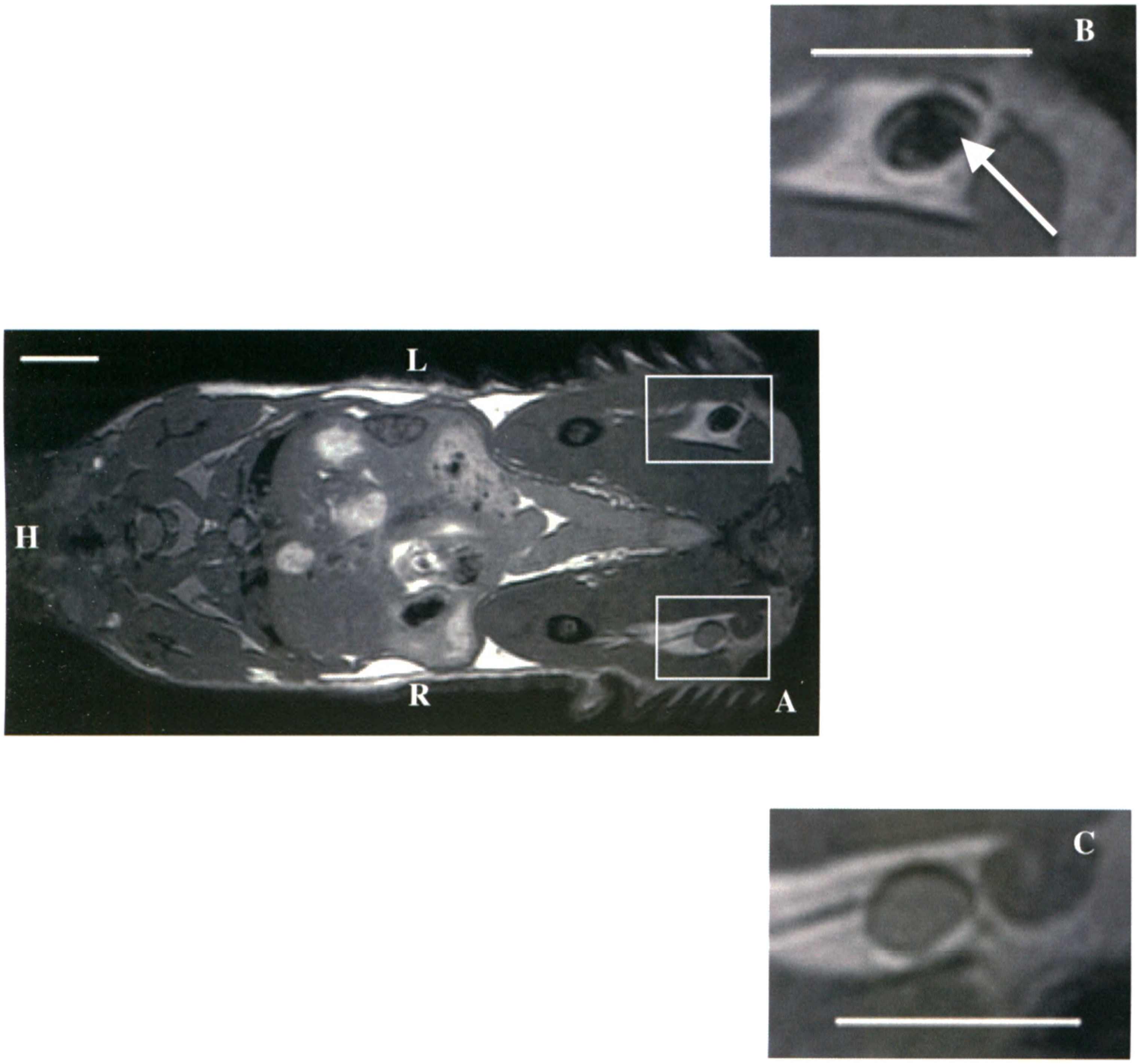

Figure 3.1. **Detectable signal loss in lymph node at 7 days after injection of 1x10^6 DC.** Coronal 3DFIESTA image (200x200x200μm) showing the popliteal lymph nodes from one representative mouse, seven days after injection with 1x10^6 unlabeled DC to the right footpad and 1x10^6 MPIO-labeled DC to the left footpad. (B&C) Cropped and enlarged images of popliteal lymph nodes in A (white boxes). Arrow indicates the region of signal loss within the left lymph node. H=head, R=right, L=left. Images are representative of n = 8. Scale bar = 0.5 cm.

Figure 3.2 shows representative images for one mouse at seven days after injection with 0.1×10^6 DC. Figure 3.2A shows the left lymph node after injection of 0.1×10^6 MPIO-labeled DC to the left footpad and Figure 3.2B shows the right lymph node after the footpad injection of 0.1×10^6 unlabeled DC. Cropped and enlarged images of left and right popliteal lymph nodes in A and B (white boxes) are shown in C and D, respectively. The region of signal loss is clearly detectable in the central part of the left lymph node. In this group of mice, signal loss was observed in the left lymph node in 2 out of 4 mice.

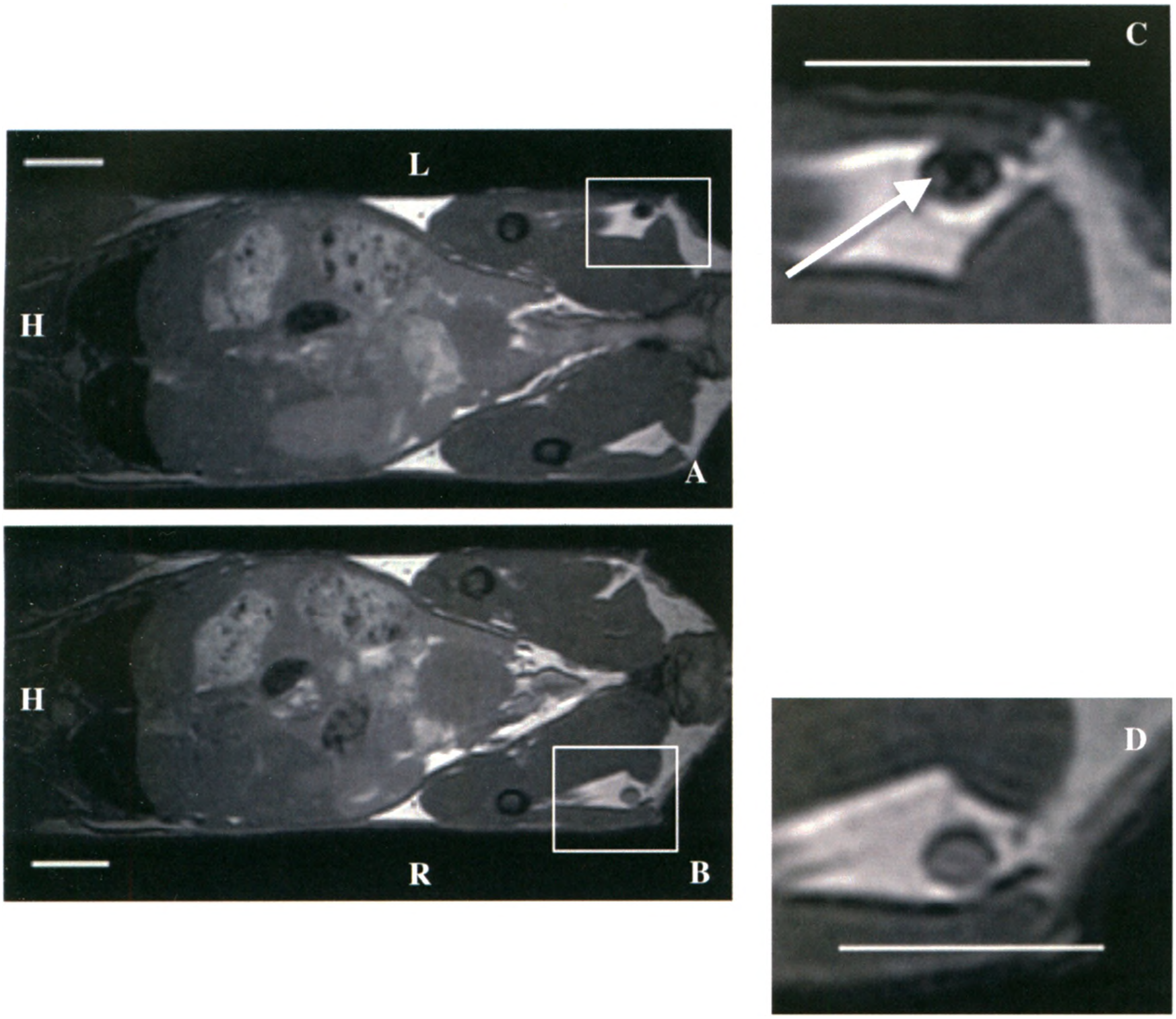

Figure 3.2. **Detectable signal loss in lymph nodes at 7 days after injection of 0.1×10^6 DC.** Coronal 3DFIESTA images (200x200x200µm) showing the popliteal lymph nodes from one representative mouse, seven days after injection with (A) 0.1×10^6 MPIO-labeled DC or (B) 0.1×10^6 unlabeled DC. (C&D) Cropped and enlarged images of popliteal lymph nodes in A&B (white boxes). Arrow indicates the region of signal loss within the left lymph node. H=Head, L=left, R=right. Images are representative of n = 8. Scale bar = 0.5 cm.

Cropped and enlarged images of the right (A) and left (B) popliteal lymph nodes for a representative mouse injected with 1×10^6 unlabeled DC and 1×10^6 MPIO-labeled DC and imaged at multiple time points are shown in Figure 3.3. The region of signal loss within the left popliteal lymph node was evident at day 2 post-injection and appears to increase over time between days 2 and 7. This hypointense region covered a large extent of the left lymph node at all post-injection time points. Surprisingly, a slight decrease in the signal intensity of the right lymph node was observed after injection of unlabeled DC. It is also apparent from the images that the size of the lymph node itself increased after the cell injection, for both the right and left sides (MPIO-labeled and unlabeled DC). The same result was observed in all mice that received 1×10^6 DC ($n = 8$).

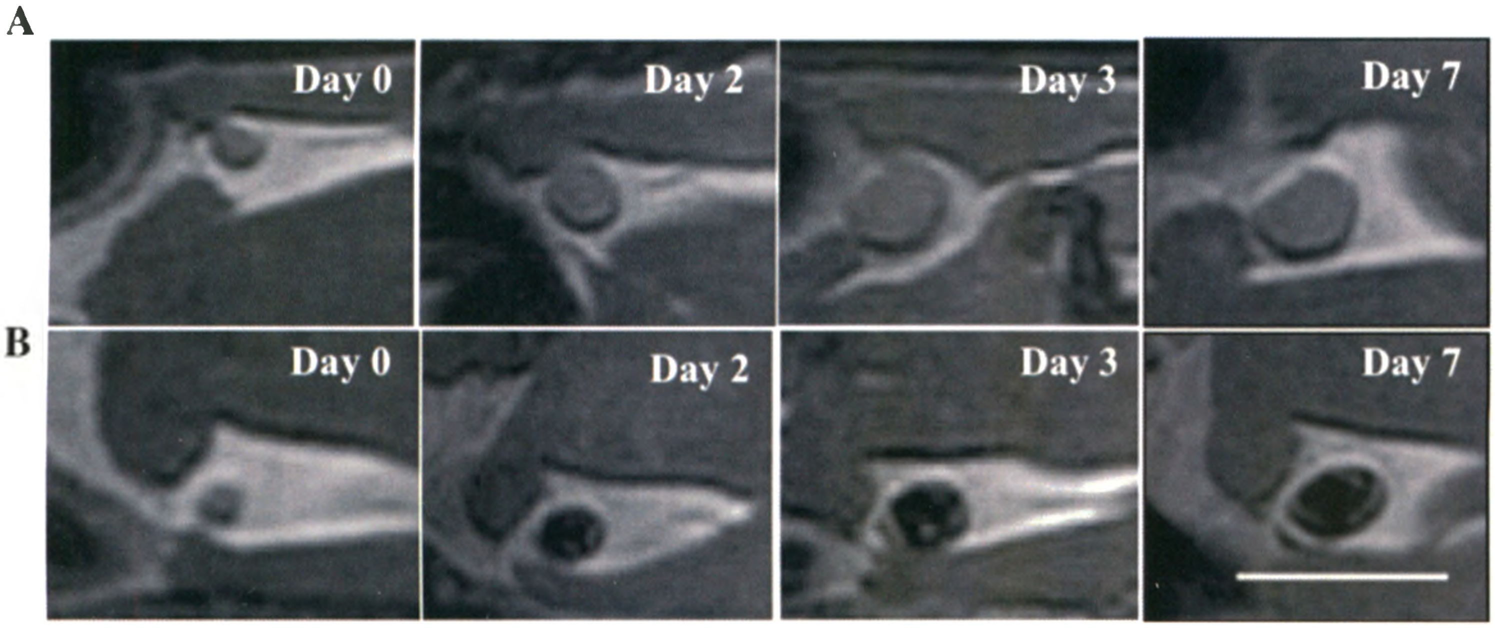

Figure 3.3. **Representative in vivo coronal images of popliteal lymph nodes at different time points after injection of 1×10^6 DC.** Coronal 3DFIESTA images (cropped and enlarged) of the right (A) and left (B) popliteal lymph nodes of the mouse injected with 1×10^6 MPIO labeled DC at 72 hours pre-injection and at day 2, 3 and 7 post-injection. A region of hypointensity was detected at day 2 after injection and persisted up to day 7. Images are representative of n = 8. Scale bar = 0.5 cm.

In the mice injected with 0.1×10^6 DC that showed signal loss in the node (2 of 4) a much smaller, less obvious region of signal loss was observed (Figure 3.4B). The region of signal loss was detected in the central part of the lymph node at day 3 and persisted in the same location up to day 7. In MR images it appears that the size of both the right and left lymph nodes increased slightly after the injection of 0.1×10^6 DC.

No signal loss was observed in any of the other lymph nodes in the mouse body after injection of either 0.1×10^6 or 1×10^6 MPIO-labeled DC.

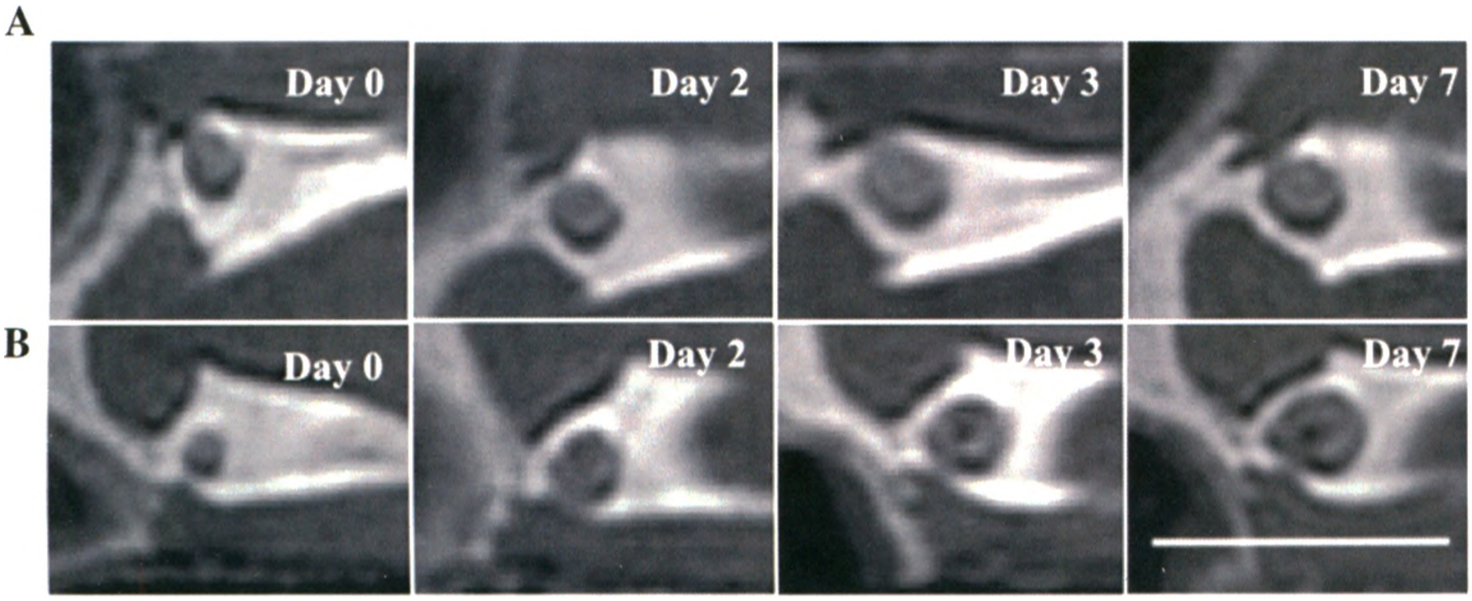

Figure 3.4. **Representative in vivo coronal images of popliteal lymph nodes at different time points after injection of 0.1×10^6 DC.** Coronal 3DFIESTA images (cropped and enlarged) of the right (A) and left (B) popliteal lymph nodes of the mouse injected with 0.1×10^6 MPIO labeled DC at 72 hours pre-injection and at day 2, 3 and 7 post-injection. Region of hypointensity was detected at day 3 after injection and persisted up to day 7. Images are representative of n = 2. Scale bar = 0.5 cm.

Figure 3.5 shows the quantification of the MR images. The fractional signal loss and the signal void volume was only measured for the mice injected with 1×10^6 MPIO-labeled DC because the signal void did not appear in all mice injected with 0.1×10^6 MPIO-labeled DC and because the appearance of signal void in these cases was much more subtle than in mice that were injected with 1×10^6 DC. The lymph node volume was measured for all mice and results are presented in Figure 3.5C.

After the footpad injection of 1×10^6 MPIO-labeled DC, the fractional signal loss (Figure 3.5A) in the left lymph node increased over time and reached approximately 92% at day 7. A Student t test confirmed that fractional signal loss at day 7 was significantly greater than the fractional signal loss at day 2. Similarly, signal void volume increased over time following the injection of the 1×10^6 MPIO-labeled DC (Figure 3.5B). There is a statistically significant difference between the signal void volume at day 2 (mean value of 0.933 mm^3) and day 3 (mean value of 1.22 mm^3), as well as between day 3 and day 7 (mean value of 2.30 mm^3).

The volumes of both right and left lymph nodes increased significantly over time after injection of either 1×10^6 unlabeled or MPIO-labeled DC (Figure 3.5C). There was no significant difference in the node volume after injection of unlabeled DC versus MPIO-labeled DC. The volume of lymph node after the injection of 1×10^6 cells was significantly larger than the volume of lymph node after the injection of 0.1×10^6 cells. No statistically significant increase in the size of the lymph node was found at different time points after injection of 0.1×10^6 unlabeled or labeled DC. These results are consistent with MR images of lymph nodes.

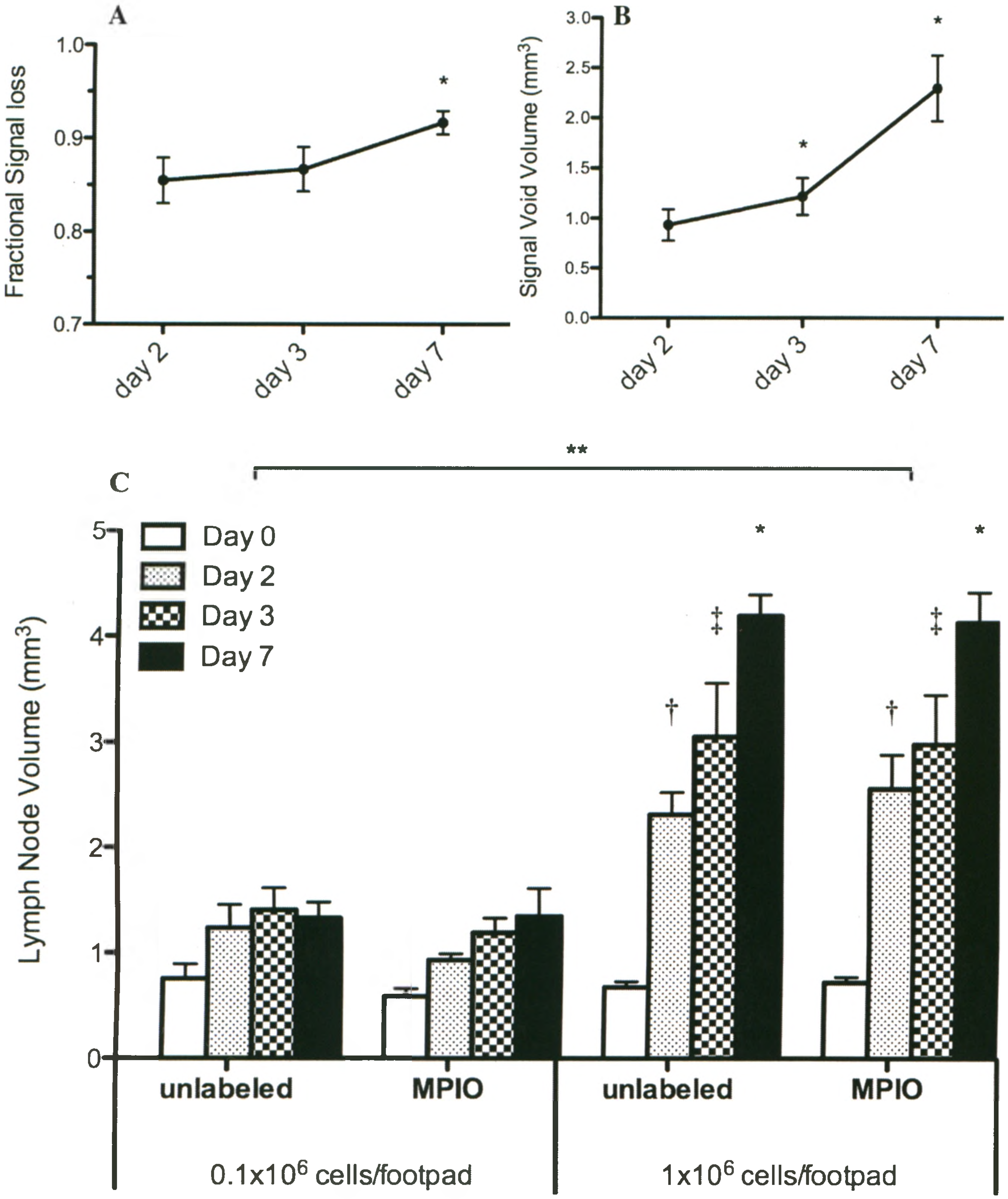

Figure 3.5. **Measurements of the lymph node volume, signal void volume and the fractional signal loss.** Fractional signal loss (A), signal void volume (B) were measured from images acquired 2, 3 and 7 days after injection of 1x10^6 DC. Horizontal bars represent mean values ±SEM (*$P<0.05$ for Day 2 vs. Day 3 and Day 3 vs. Day 7). Lymph node volume (C) was measured from images acquired pre-injection (day 0), 2, 3 and 7 days post-injection. Data are means ±SEM ($n = 8$ for 1×10^6 cells/footpad and $n = 4$ for 0.1×10^6 cells/footpad, †$P<0.05$ for Day 2 vs. Day 3, ‡$P<0.05$ for Day 3 vs. Day 0, *$P<0.05$ for Day 7 vs. Day 0, **$P<0.01$ for 1×10^6 cells/footpad vs. 0.1×10^6 cells/footpad).

3.3.2. Histology

Figure 3.6 presents representative fluorescence images of PKH+ DC in the lymph nodes 7 days after the injection of 1×10^6 unlabeled (3.6A) or MPIO-labeled (3.6B) DC. PKH+ DC were located mainly in the deep cortex of lymph nodes whether MPIO-labeled or unlabeled. Similar to the results of histology at day 2 post-injection (Chapter 2, Figure 2.6), the amount of DC in the draining lymph node, as indicated by the fluorescence images, was greater after the injection of unlabeled DC compared to MPIO-labeled DC. However, there appears to be fewer DC in the lymph nodes at day 7 compared with day 2. In some sections, an artifact caused by PKH was observed on some parts of the edge of sections. This artifact was evident after injection of either unlabeled or labeled DC.

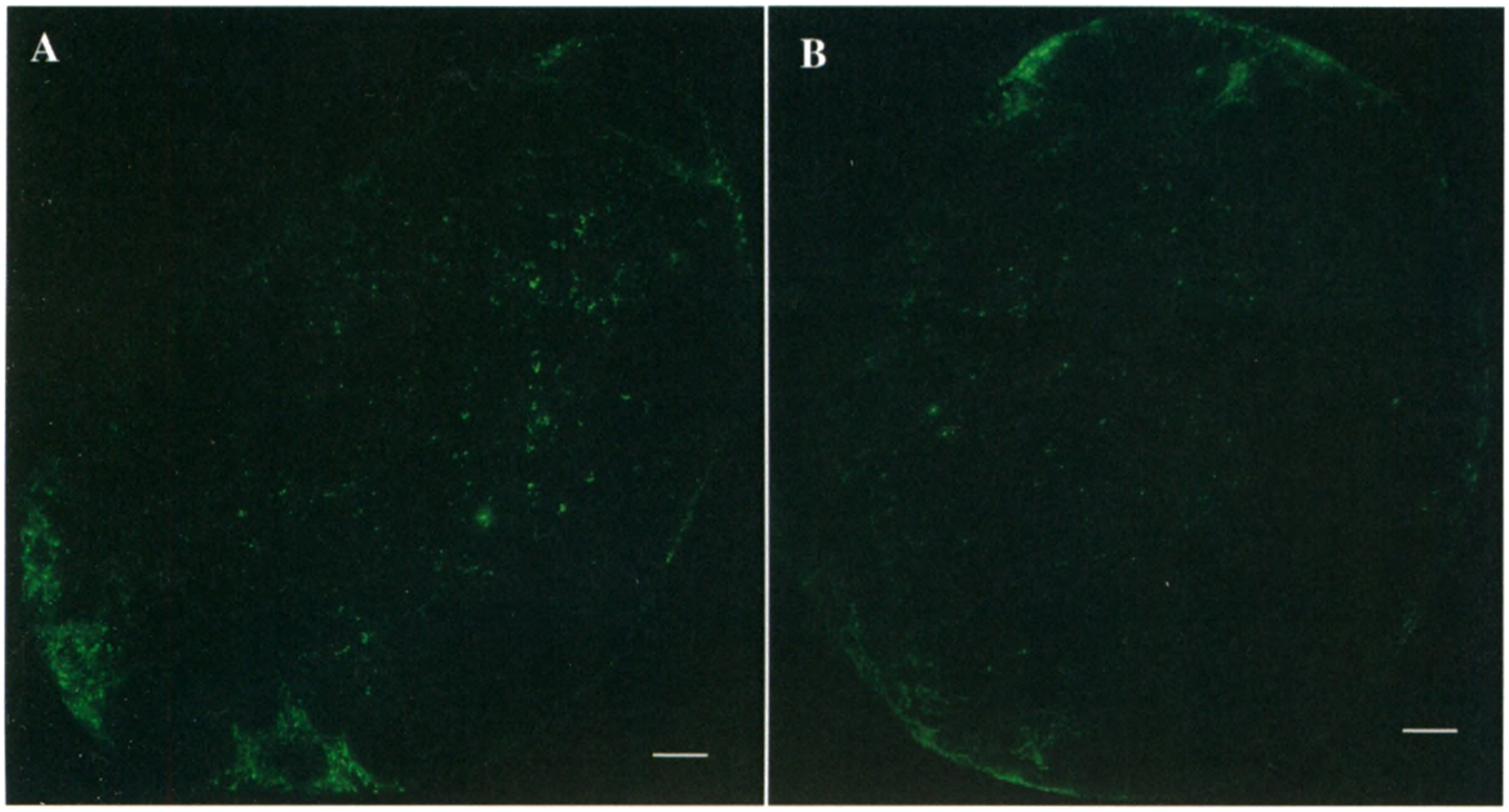

Figure 3.6. **Distribution of green PKH fluorescence in popliteal lymph nodes.** Distribution of green PKH fluorescence in popliteal lymph nodes seven days after injection of 1×10^6 unlabeled DC (A) or MPIO-labeled DC (B). The green fluorescent regions correspond with the presence of PKH+ DC. Scale bar = 100 μm

Comparing the fluorescence microscopy of green PKH+ DC and flash red MPIO particles in the popliteal lymph nodes revealed that the amount of green PKH+ DC was much less than the amount of flash red MPIO particles in the left lymph nodes (Figure 3.7). Green PKH fluorescence that corresponds to PKH+ DC was mainly distributed in the central part of the lymph node. Flash red fluorescence, that corresponds MPIO particles, was also mainly located in the central part of the nodes (Figure 3.7B), however, with more density per area of lymph node. This was observed in the majority of the sections through the lymph node.. Figures 3.7A and 3.7B are representative images of n = 4.

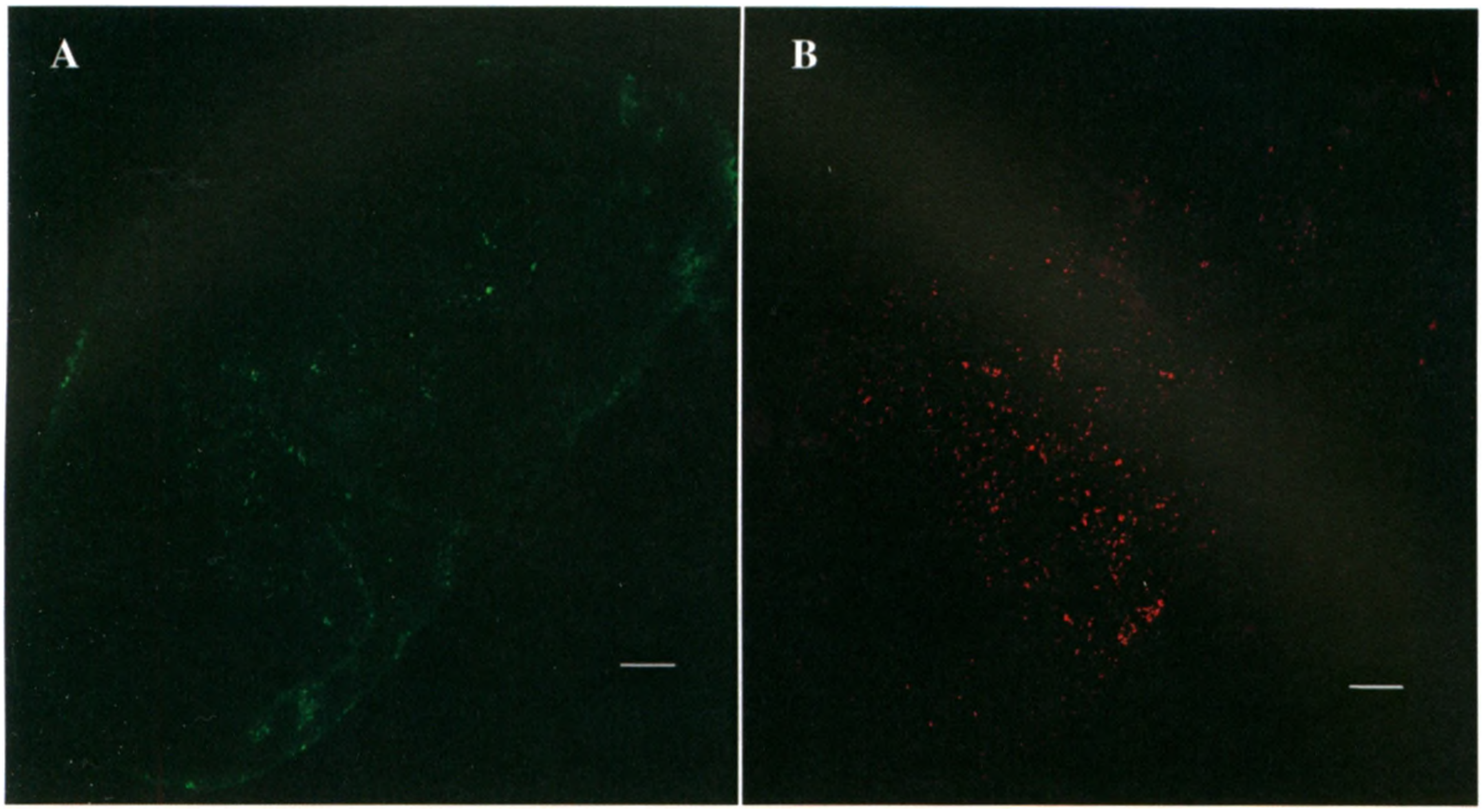

Figure 3.7. **Distribution of green PKH+ DC and flash red MPIO in popliteal lymph nodes 7 days after the injection of 1×10^6 DC.** Amount of green PKH+ DC in left lymph node (A) is less than the amount of flash red MPIO particles (B). Scale bar = 100 μm.

3.3.3. Inter- and Intra-observer Variability Assessment for Lymph Node Volume Measurement

Figure 3.8A is a Bland-Altman plot showing the results of the inter-observer variability analysis. In this plot, results of the lymph node volume measurement performed by two observers are shown. Most of the measurements are placed within the range of agreement which is the average of differences (bias) ± standard deviation (SD) (from −1.092 to +0.882). This plot indicates that measurements of two observers are in agreement. Linear regression analysis on the measurements of lymph node volume by the two observers suggests a strong positive correlation between them ($R^2 = 0.849$, Figure 3.8B).

The Bland-Altman plot for the result of intra-observer variability analysis is shown in Figure 3.9A. One observer repeated the lymph node volume measurements for the same set of images twice. In this graph, the difference between two measurements is plotted against the average of two measurements. Data points are mostly within the range of agreement (from −0.4084 to +0.4123). Furthermore, a strong positive correlation between two measurements of the same data set was found using linear regression analysis ($R^2 = 0.972$, Figure 3.9B). This indicates an excellent intra-observer agreement for lymph node volume measurement.

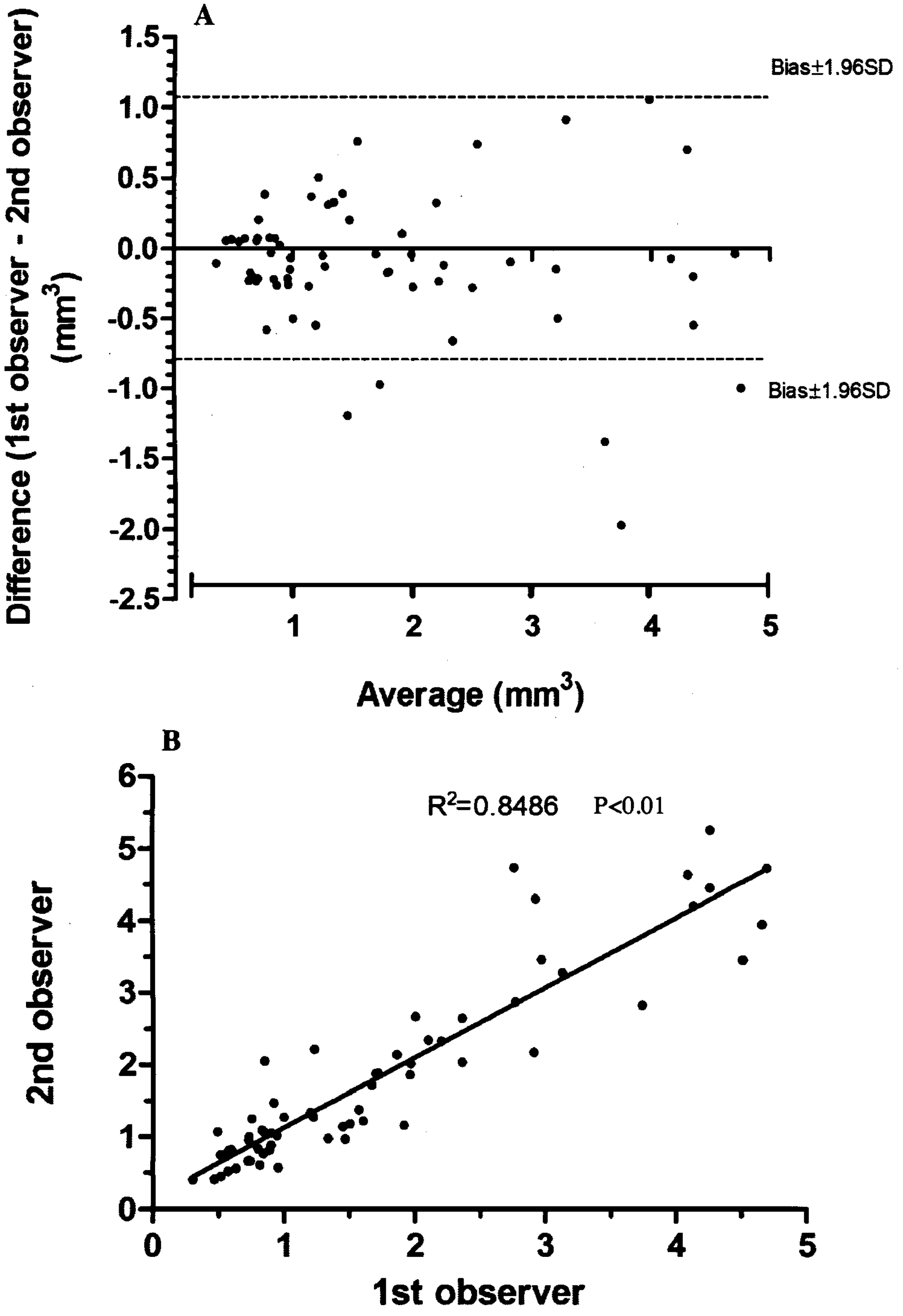

Figure 3.8. **Inter-observer variability assessment.** (A) Bland-Altman plot of the lymph node volume measurement between two observers. (B) correlation of lymph node volume measurements between two observers. SD = standard deviation

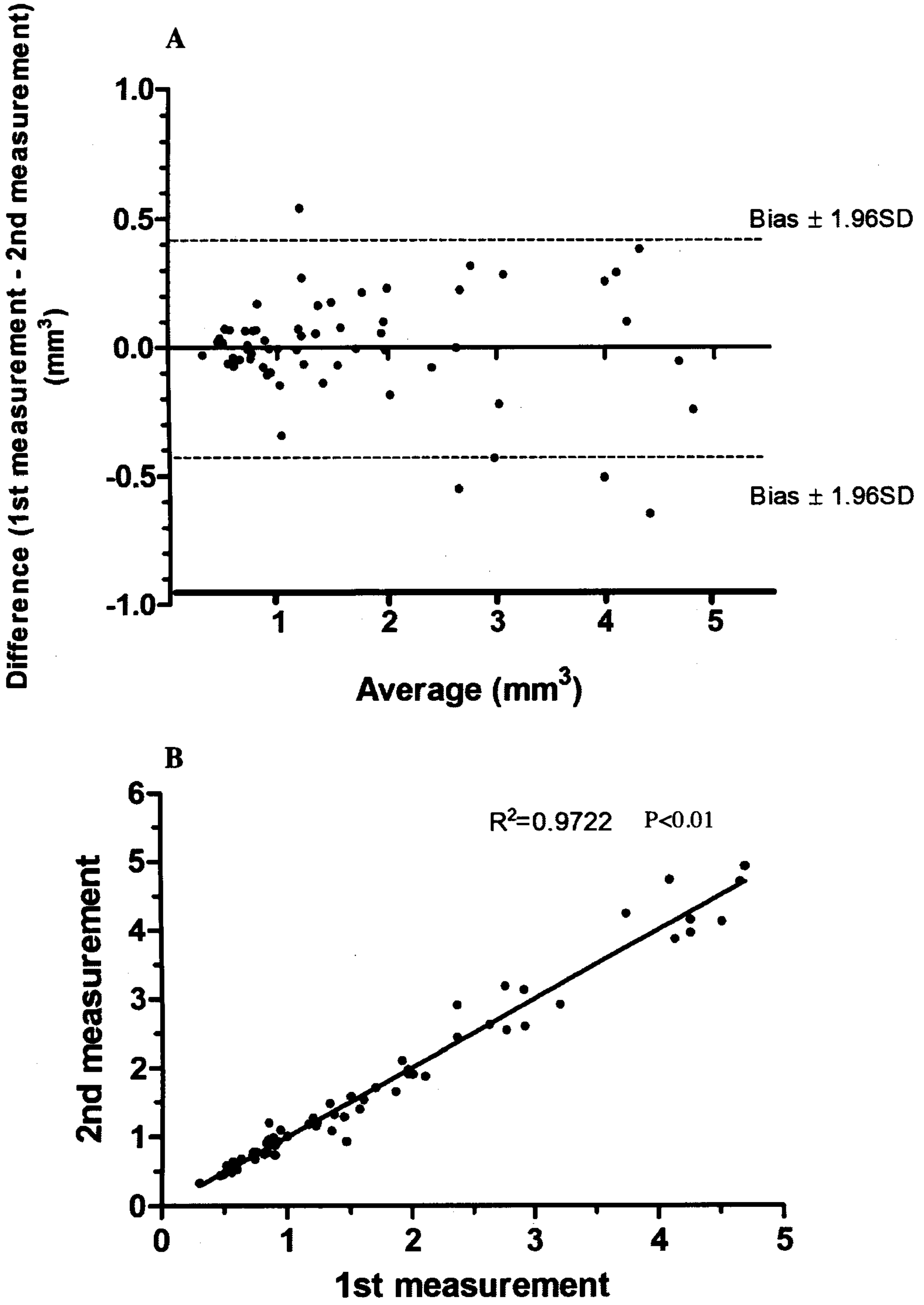

Figure 3.9. **Intra-observer variability assessment.** (A) Bland-Altman plot of lymph node volume measurements of the same data set performed twice by one observer. (B) correlation two lymph node volume measurements. SD = standard deviation.

3.4. Discussion

In the current chapter, we use cellular MRI techniques to study the fate of MPIO-labeled DC longitudinally. This experiment was designed to investigate whether signal loss in the node images was due to the presence of MPIO-labeled DC or to free MPIO particles. Most studies suggest that the migration of DC to draining nodes peaks at 48 hours after their subcutaneous injection and declines afterward (11), in line with the DC lifespan. However our imaging results show that signal loss is present in images of the nodes at day 2 post injection and persists in the node for up to 7 days. Of additional interest is related work going on in our lab which has shown the same result for SPIO-labeled DC. We are not the only group who have shown this type of imaging result. Previously, Baumjohann et al monitored the fate of the SPIO-labeled DC in the mouse lymphatic system and showed that signal loss persisted in the node for up to 112 hours after injection (12).

A quantitative analysis of the images revealed that signal void caused by MPIO-labeled DC in the node increased in size over time. The fractional signal loss was also found to increase with time. This suggests that iron was transported to the lymph node within cells or passively over time and therefore the accumulation of iron in the imaging voxels increased with time.

The volume of the lymph nodes increased over time after the injection of 1×10^6 DC (labeled or unlabeled). This may be an indication of T cell proliferation and an increase in the cellularity of lymph nodes. Our findings are similar to a previous study in which the increase in mouse lymph node cellularity was examined each day after injection of DC up to day 7. This study showed that increase in the cellularity of lymph node was detectable at day 1 after injection of 1×10^6 DC, increased up until day 4 and reached a plateau afterward (14). The fact that there was no difference in the change in node volume after the injection of unlabeled or labeled DC suggests no influence of MPIO labeling on the ability of DC to activate T cells.

Fluorescence microscopy of dissected nodes at day 7 showed that the amount of MPIO did not correspond well with the amount of DC; red fluorescence due to MPIO was greater than green fluorescence due to DC. This suggests that MPIO, which could be released from dying DC, are likely present in the lymph nodes freely or within cells other than the donor DC. Since only a small percentage of injected DC eventually migrate to the lymph nodes, some DC die at the site of injection or on their way to lymph nodes. MPIO released from dying DC are possibly taken up by resident DC or macrophages and arrive at the lymph nodes at later time points. A previous study on in vivo SPIO labeling and tracking of DC showed that endogenous DC capture SPIO released from injected dying tumor cells and migrate to mouse popliteal lymph node (13). The number of DC observed to be in the node by fluorescence was reduced compared with the number of DC in the node at day 2 (observed in Chapter 2). This is consistent with the previous reports of a 1-3 day life span for migrated DC (11).

The observations of these experiments, taken together with the results presented in Chapter 2, indicate that MPIO-labeled DC can be reliably tracked in vivo by MRI in the short-term, however the interpretation of signal loss in images of MPIO-labeled DC at timepoints longer than the lifespan of DC is complicated and needs to be interpreted with caution.

3.5. References

1. Porgador A, Snyder D, Gilboa E. Induction of antitumor immunity using bone marrow-generated dendritic cells. J Immunol. 1996 Apr 15;156(8):2918-26.

2. Steinman RM, Banchereau J. Taking dendritic cells into medicine. Nature. 2007 Sep 27; 449(7161):419-26.

3. Figdor CG, de Vries IJ, Lesterhuis WJ, Melief CJ. Dendritic cell immunotherapy: mapping the way. Nat Med. 2004 May;10(5):475-80.

4. de Vries IJ, Lesterhuis WJ, Barentsz JO, Verdijk P, van Krieken JH, Boerman OC, Oyen WJ, Bonenkamp JJ, Boezeman JB, Adema GJ, Bulte JW, Scheenen TW, Punt CJ, Heerschap A, Figdor CG. Magnetic resonance tracking of dendritic cells in melanoma patients for monitoring of cellular therapy. Nat Biotechnol. 2005 Nov;23(11):1407-13.

5. Ahrens ET, Feili-Hariri M, Xu H, Genove G, Morel PA. Receptor-mediated endocytosis of iron-oxide particles provides efficient labeling of dendritic cells for in vivo MR imaging. Magn Reson Med. 2003 Jun;49(6):1006-13.

6. de Vries IJ, Krooshoop DJ, Scharenborg NM, Lesterhuis WJ, Diepstra JH, Van Muijen GN, Strijk SP, Ruers TJ, Boerman OC, Oyen WJ, Adema GJ, Punt CJ, Figdor CG. Effective migration of antigen-pulsed dendritic cells to lymph nodes in melanoma patients is determined by their maturation state. Cancer Res. 2003 Jan 1;63(1):12-7.

7. Eggert AA, Schreurs MW, Boerman OC, Oyen WJ, de Boer AJ, Punt CJ, Figdor CG, Adema GJ. Biodistribution and vaccine efficiency of murine dendritic cells are dependent on the route of administration. Cancer Res. 1999 Jul 15;59(14):3340-5

8. Dekaban GA, Snir J, Shrum B, de Chickera S, Willert C, Merrill M, Said EA, Sekaly RP, Foster PJ, O'Connell PJ. Semiquantitation of mouse dendritic cell migration in vivo using cellular MRI. J Immunother. 2009 Apr;32(3):240-51.

9. Shapiro EM, Sharer K, Skrtic S, Koretsky AP. In vivo detection of single cells by MRI. Magn Reson Med. 2006 Feb;55(2):242-9.

10. Shapiro EM, Skrtic S, Sharer K, Hill JM, Dunbar CE, Koretsky AP. MRI detection of single particles for cellular imaging. Proc Natl Acad Sci U S A. 2004 Jul 27;101(30):10901-6. Epub 2004 Jul 15.

11. Huck SP, Tang SC, Andrew KA, Yang J, Harper JL, Ronchese F. Activation and route of administration both determine the ability of bone marrow-derived dendritic cells to accumulate in secondary lymphoid organs and prime CD8+ T cells against tumors. Cancer Immunol Immunother. 2008 Jan;57(1):63-71.

12. Baumjohann D, Hess A, Budinsky L, Brune K, Schuler G, Lutz MB. In vivo magnetic resonance imaging of dendritic cell migration into the draining lymph nodes of mice. Eur J Immunol. 2006 Sep;36(9):2544-55.

13. Long CM, van Laarhoven HW, Bulte JW, Levitsky HI. Magnetovaccination as a novel method to assess and quantify dendritic cell tumor antigen capture and delivery to lymph nodes. Cancer Res. 2009 Apr 1;69(7):3180-7.

14. MartIn-Fontecha A, Sebastiani S, Höpken UE, Uguccioni M, Lipp M, Lanzavecchia A, Sallusto F. Regulation of dendritic cell migration to the draining lymph node: impact on T lymphocyte traffic and priming. J Exp Med. 2003 Aug 18;198(4):615-21.

Chapter 4: Monitoring the Accumulation of SPIO and MPIO in the Mouse Lymph Node using Cellular MRI

Yuhua Chen, lab manager of the Foster group performed cryosectioning of lymph nodes. Development of the custom gradient insert coil and radiofrequency coils used in this project was completed in Dr. Rutt's Lab. SPIO injection and histological analysis of mice received SPIO were done by Sonali De Chickera. All other procedures including MR acquisition, mouse anesthesia, MPIO injection, tissue dissection and preparation for microscopy and fluorescence microscopy were performed by Roja Rohani.

4.1. Introduction

A number of labs have investigated the use of superparamagnetic nanoparticles (SPIO) to label dendritic cells (DC) and track their migration in mice (1-4). In Chapters 2 and 3, we reported on the use of micron sized iron oxide particles (MPIO) to label and detect DC by cellular MRI. We have shown that the migration of MPIO-labeled DC can be monitored in vivo in mice and that the signal loss due to DC in the nodes can be measured.

An important concern regarding tracking iron labeled cells using cellular MRI is that free iron, that might be associated with labeled cells or released from dead cells, may be misinterpreted in MR images as viable labeled cells (5-7). In Chapter 3 we found that a portion of MPIO particles in the draining lymph node were not within DC at day 7 post-injection. This result may be an indication of the presence of free MPIO at time points later than DC lifetime, which urges a caution in interpretation of signal void as MPIO-labeled DC.

The MR appearance of freely injected iron particles has been explored previously. Baumjohann et al showed that SPIO particles can be seen in subcapsular or sinus areas of the lymph node within 4 to 24 hours after footpad injection, but not enter the deeper central paracortex areas (2). This may suggest SPIO is transported passively to the nodes. A study in 2009 showed that the injection of free SPIO resulted in the rapid appearance of signal loss in the subcapsular region of lymph nodes (4). It reported that active transport of SPIO to the central part of the node by cells was not observed earlier than 3 days post-injection. So far, the accumulation of free SPIO in the mouse draining lymph node has been investigated, however a similar study for MPIO has not been performed.

In this chapter, the MRI and histological appearance of mouse lymph nodes was studied after the subcutaneous injection of free MPIO and SPIO. Our results show that signal void caused by both SPIO and MPIO particles in the mouse lymph node is detectable in vivo for up to day 21 post-injection.

4.2. Methods

4.2.1. In Vivo MR Imaging of Mouse Lymph Node After Free MPIO and SPIO Injection

MPIO and SPIO Administration

The amount of iron equivalent to 0.1 or 1×10^6 MPIO-labeled DC was calculated with respect to the result of inductively coupled plasma mass spectroscopy (ICP-MS). The resultant concentrations of free MPIO were diluted with sterilized Hank's Buffered Salt Solution (HBSS) and injected subcutaneously into the right footpad of recipient C57Bl/6 mice (n = 4 for each dose). For the control experiment, an equivalent amount of sterilized HBSS was injected into the left footpad. MPIO were 0.90 μm in diameter and tagged with flash-red fluorescent agent (excitation:emission peaks, 660:690 nm) (Bangs beads, Bangs Laboratories, Fisher, IN).

For SPIO administration, the same method was repeated with two groups of mice (n = 2 for each dose).

MR Imaging

Imaging of mice injected with free MPIO was performed in vivo using a 3 Tesla (3T) GE whole-body MR scanner (MR Signa® Excite™, GE Healthcare, Milwaukee, WI, USA) with a custom-built gradient coil (inner diameter=17.5cm, maximum gradient strength=500 mT/m, and peak slew rate=3000 T/m/sec) and a solenoid radiofrequency coil (4cm in length and 3cm in diameter). Mice were scanned using the a 3D fast imaging employing steady state acquisition (3D-FIESTA; GE Medical Systems, Milwaukee, WI, USA) pulse sequence. The imaging parameters were: repetition time (TR) = 4.2 ms, echo time (TE) = 2.1 ms, flip angle = 20°, bandwidth = 62.5 kHz, 200 μm^3 isotropic resolution over a 6cm FOV, 8 RF phase cycles and 1 signal average. Acquisition time was 21 minutes.

In vivo MR imaging of mice injected with free SPIO was done using a 1.5T GE CV/i MR scanner (GE Medical Systems, Milwaukee, WI) using a custom-built gradient coil (inner diameter=12 cm, maximum gradient strength=600 mT/m, and peak slew rate of 2000 T/m/s) and a customized solenoidal radiofrequency coil (diameter = 4cm, length = 4.5cm). Mice were scanned using 3D FIESTA pulse sequence. The imaging parameters were: TR = 9.2 ms, TE = 4.2 ms, flip angle = 30°, bandwidth = 20.83 kHz, 200 μm^3 isotropic resolution over a 6cm FOV and 2 signal average while phase cycling was on. Acquisition time was 21 minutes.

During scanning, anesthesia was induced and maintained with isofluorane (2% in oxygen to induce and 1.5% in oxygen to maintain) using a nose cone with vacuum for scavenging. Mice were placed on a custom-built plastic sled for secure positioning. The lower part of the body and tail of the mice were wrapped using gauze to maintain body temperature. All mice were scanned 2, 7, 14 and 21 days after the injection.

4.2.2. Histological Analysis of Mouse Lymph Node After Free MPIO Injection

MPIO Administration and Animal Groups

New mice, which were not imaged, were used to analyze the presence of MPIO in the node. Free MPIO (0.90 μm flash red MPIO) equivalent to the iron content of 1×10^6 MPIO-labeled DC were diluted with HBSS and injected subcutaneously into the right footpad of recipient C57Bl/6 mice. 4 groups of mice were used in a cross sectional experiment. 3 mice in each group were sacrificed at each of days 2, 4, 7 and 14 post-injection (n = 12) and their popliteal lymph nodes were removed.

Tissue Histology and Microscopy

Dissected popliteal lymph nodes were fixed using 10% formaldehyde in phosphate buffer solution (PBS) at 4% overnight. Cryoprotection of lymph nodes was performed by sequential incubation (24 hours) in increasing concentrations of sucrose in PBS (10%, 20% and 30%). For sectioning, lymph nodes were embedded in OCT compound (Sakura Finetek, Torrance CA) and snap frozen using dry ice. The entire node was cryosectioned into 16μm sections using a cryostat at a chamber and object temperature of -20°C. Serial sections were placed on collagen coated glass slides. Sections were subsequently studied with fluorescence microscopy for the presence flash red MPIO particles. Each section was examined with the Texas red channel (excitation: 530-585 nm, emission: 615 nm) to detect and localize MPIO particles. Sections were also stained with Perl's Prussian blue (PPB) and eosin. Digital images were collected using a Zeiss Axioimager fluorescence microscope equipped with a Qimaging Retiga Exi_color camera.

The same method was applied to SPIO particles.

4.3. Results

4.3.1. In vivo MR imaging of free MPIO

Figure 4.1 shows representative in vivo 3DFIESTA coronal images for one mouse at 2 days after injection with free MPIO equivalent to the amount of MPIO in an injection of 1×10^6 MPIO-labeled DC. Mouse received the MPIO injection in the right footpad and an equivalent amount of sterilized HBSS in the left footpad. Cropped and enlarged images of right and left popliteal lymph nodes in A (white boxes) are shown in B and C respectively. A region of signal loss is clearly observable in the right lymph node. It is located in the central part of the node. As expected, no signal loss was observed in the contralateral lymph node. Comparable results were observed in 3 more mice.

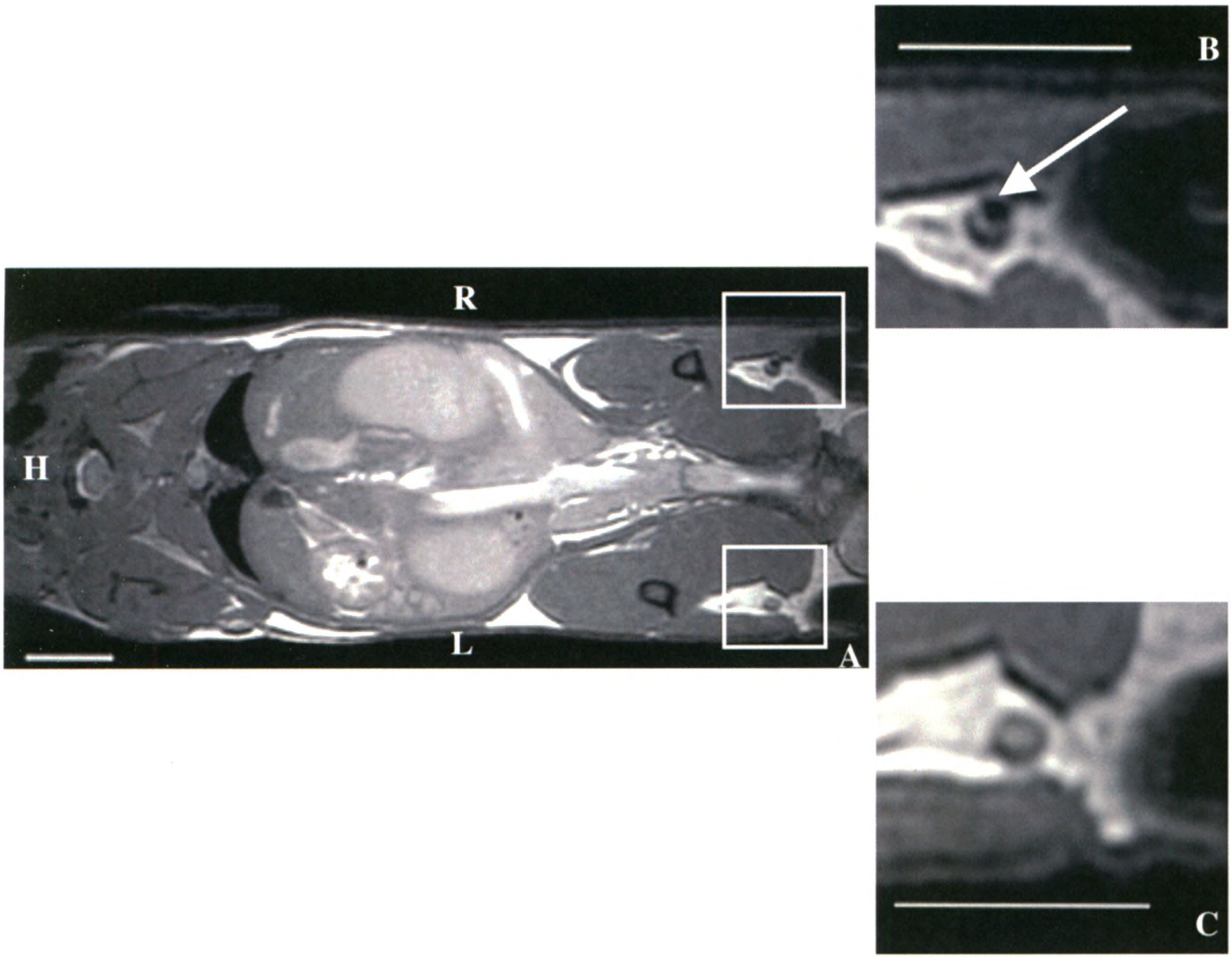

Figure 4.1. **Detectable signal loss in the right lymph node at 2 days after injection of free MPIO.** Coronal 3DFIESTA image (200x200x200μm) showing the popliteal lymph nodes from one representative mouse, two days after injection with free MPIO equivalent to 1×10^6 MPIO-labeled DC to the right footpad and HBSS to the left footpad. (B&C) Cropped and enlarged images of popliteal lymph nodes in A (white boxes). Arrow indicates the region of signal loss within the right lymph node.
H=Head, L=left, R=right. Images are representative of n = 4. Scale bar = 0.5 cm

Cropped and enlarged images of the right popliteal lymph nodes for a representative mouse injected with free MPIO equivalent to 1×10^6 MPIO-labeled DC and imaged at multiple time points are shown in Figure 4.2. The region of signal void appears to increase between days 2 and 7 and then remains unchanged up until the last scan which was on day 21 post-injection. For mice injected with a lower dose of free MPIO, signal void was detected in the popliteal node in only 1 of 4 mice and in this one mouse the appearance of the void was unchanged between days 2 and 21.

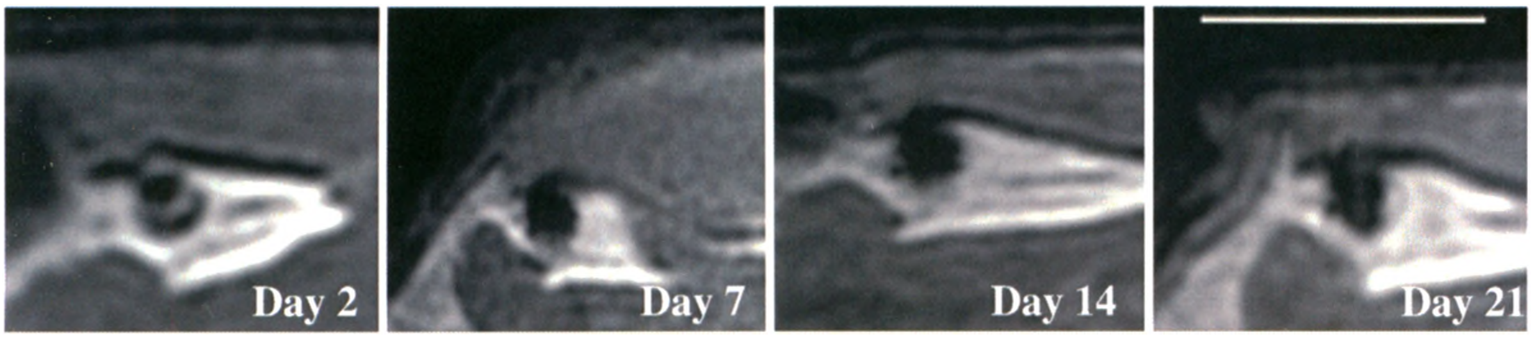

Figure 4.2. **Representative in vivo images of the mouse popliteal lymph node after injection of free MPIO.** Coronal 3DFIESTA images (cropped and enlarged) of the right popliteal lymph node of the mouse injected with free MPIO equivalent to 1×10^6 MPIO-labeled DC at day 2, 7, 14 and 21 post-injection. Images are representative of n = 4. Scale bar = 0.5 cm

4.3.2. In vivo MR imaging of free SPIO

Figure 4.3 shows cropped and enlarged images of the right popliteal lymph node for a representative mouse injected with free SPIO equivalent to 1×10^6 SPIO-labeled DC and imaged at multiple time points. In the image obtained at day 2 post-injection, signal void was very prominent, appearing to encompass the entire popliteal lymph node. Over time the region of void appeared to diminish and at day 21 appeared with a ring like pattern. Similar results were observed in the second mouse injected with this dose of SPIO.

Images of the right popliteal lymph node for a mouse injected with free SPIO equivalent to 0.1×10^6 SPIO-labeled DC (lower dose) and imaged at different time points are shown in Figure 4.4. A small region of signal void was apparent along the edge of the node in the images obtained at the day 2 post-injection. This was not apparent in images acquired at day 7 and later.

The pattern of signal void caused by free SPIO (Figure 4.3) was considerably different from the signal void caused by MPIO (Figure 4.2). While MPIO caused signal loss in the central part of the node, SPIO created signal loss mainly along the edge of the lymph node. The signal void caused by free MPIO increased over time while the signal void caused by free SPIO was maximal at day 2 and then decreased over time.

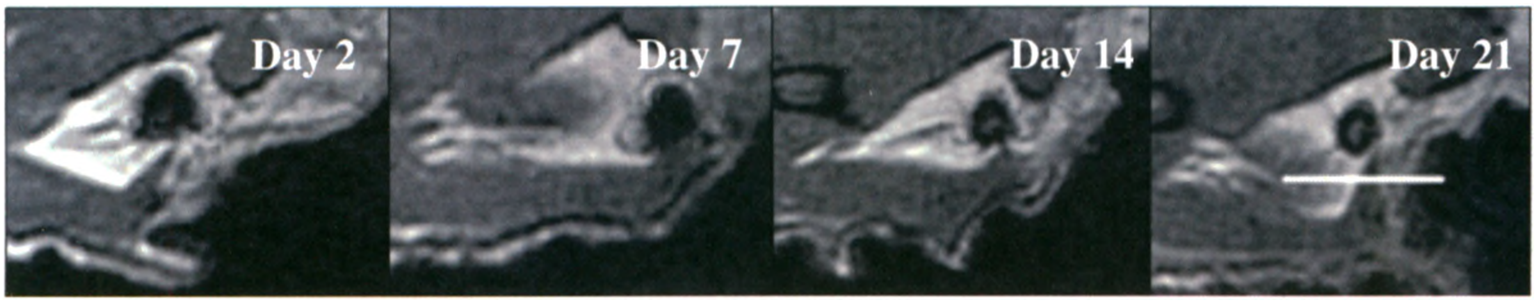

Figure 4.3. **Representative in vivo images of the mouse popliteal lymph node after injection of free SPIO.** Coronal 3DFIESTA images (cropped and enlarged) of the right popliteal lymph node of the mouse injected with free SPIO equivalent to 1×10^6 SPIO-labeled DC at day 2, 7, 14 and 21 post-injection. Images are representative of n = 2. Scale bar = 0.5 cm

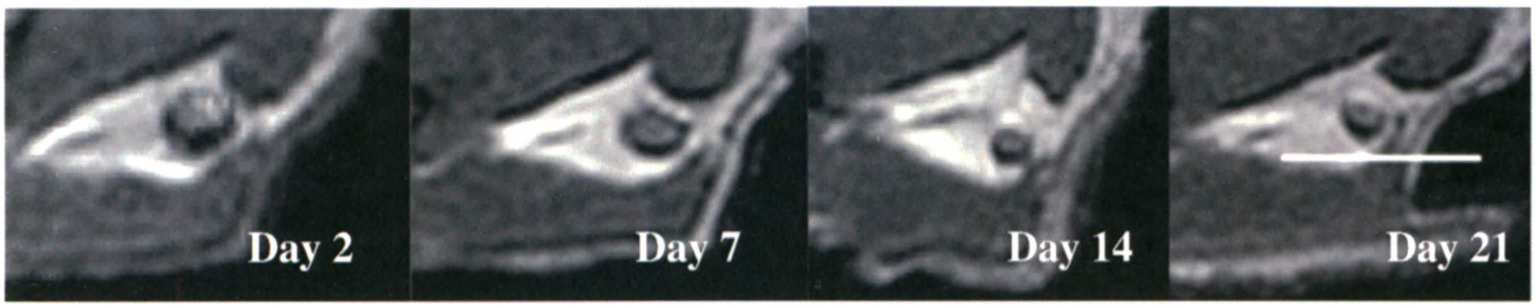

Figure 4.4. **Representative in vivo images of the mouse popliteal lymph node after injection of free SPIO.** Coronal 3DFIESTA images (cropped and enlarged) of the right popliteal lymph node of the mouse injected with free SPIO equivalent to 0.1×10^6 SPIO-labeled DC at day 2, 7, 14 and 21 post-injection. Images are representative of n = 2. Scale bar = 0.5 cm

4.3.3. Histology

Fluorescence microscopy of flash red MPIO particles in sections of popliteal lymph nodes revealed that the amount of MPIO in the right lymph node at day 2 post-injection was much less than the amount of MPIO at day 7, day 14 and day 21 (Figure 4.5). As shown in Figures 4.5B, 4.5C and 4.5D, the amount of MPIO particles in the nodes at these 3 time points appear to be similar. MPIO particles are mainly distributed in the central part of the lymph nodes at all time points. No red fluorescence was observed in the control lymph nodes. The fluorescence images of sections from the cross sectional experiment were in agreement with MR images. Figure 4.6 shows magnified images of sections in Figure 4.5 (magnification = 40x). Figures are representative images of n = 12.

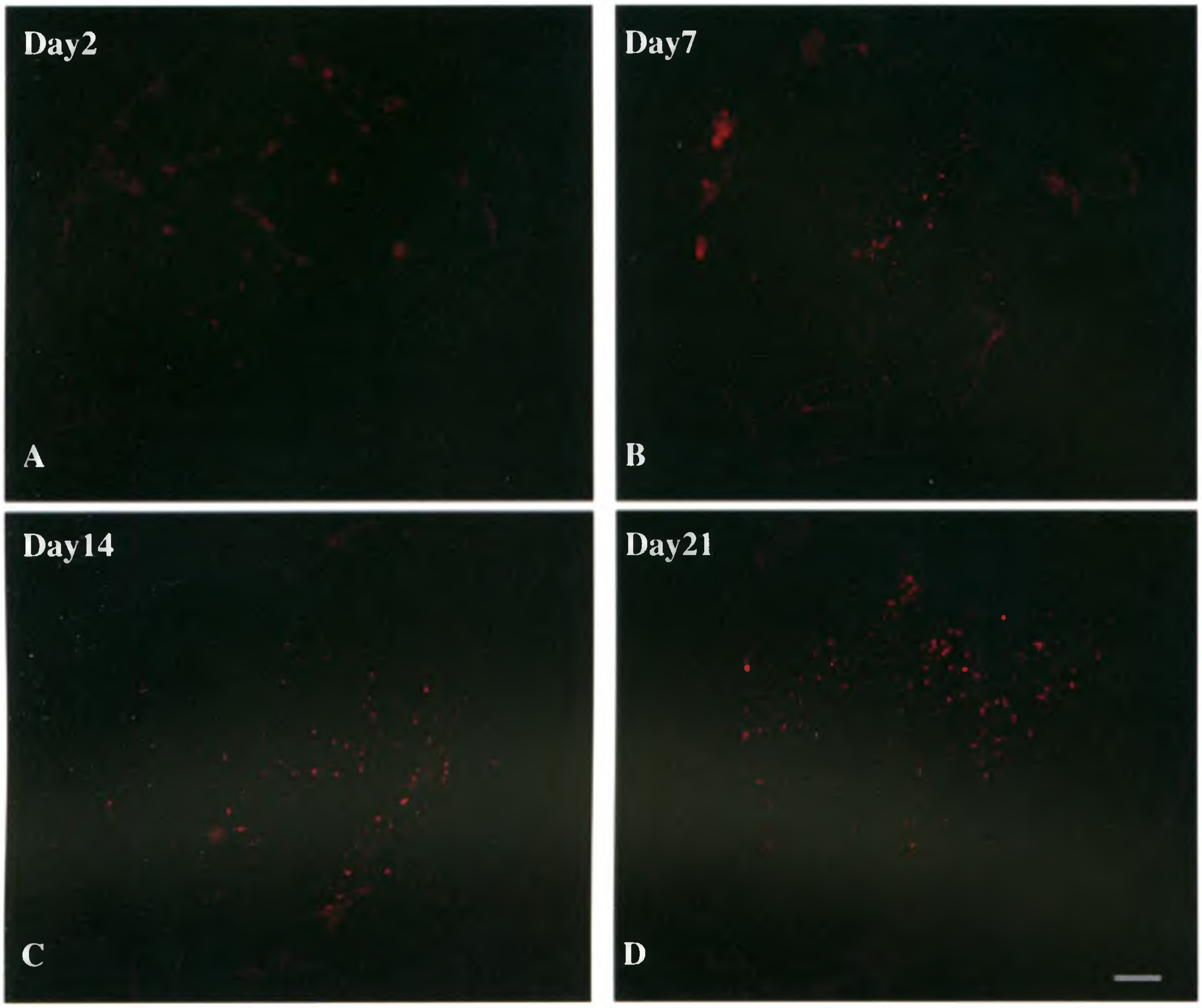

Figure 4.5 **Distribution of flash red MPIO particles in mouse lymph nodes at four time points after injection of free MPIO.** Distribution of MPIO particles in the right lymph node of a representative mouse injected with free MPIO equivalent to 1×10^6 MPIO-labeled DC at day 2 (A), 7 (B), 14 (C) and 21 (D) post-injection. The red fluorescence regions correspond to the presence of MPIO particles. Scale bar = 100 μm.

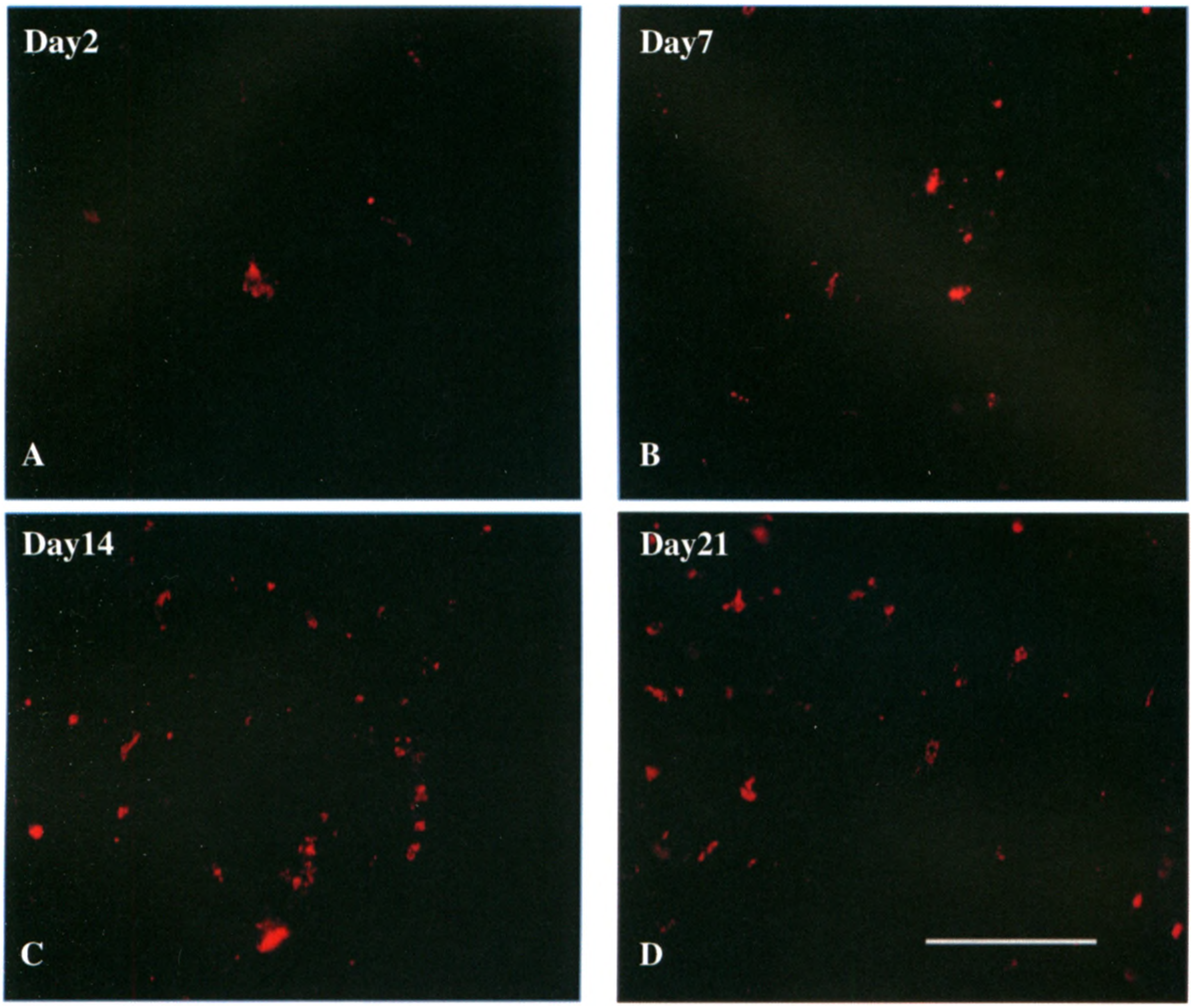

Figure 4.6. **Magnified images: Distribution of flash red MPIO particles in mouse lymph nodes at four time points after injection of free MPIO.** Magnified fluorescence images of figure 4.5 showing distribution of MPIO in the right lymph node of a representative mouse injected with free MPIO equivalent to 1×10^6 MPIO-labeled DC at day 2 (A), 7 (B), 14 (C) and 21 (D) post-injection. The red fluorescence regions correspond the to presence of MPIO particles. Scale bar = 100 μm, Magnification = 40 x

Magnified images of PPB and eosin stained sections are shown in Figure 4.7. Results of PPB staining were in agreement with fluorescent microscopic analysis and the MRI appearance of the right nodes after injection of free MPIO equivalent to 1×10^6 MPIO-labeled DC. They indicate that MPIO particles in the lymph nodes are present at day 2 post-injection and increase over time. There are approximately similar amounts of PPB stained particles at days 7, 14 and 21 post-injection. They also demonstrate that blue stained iron is in the eosin stained tissue and not in the extracellular spaces.

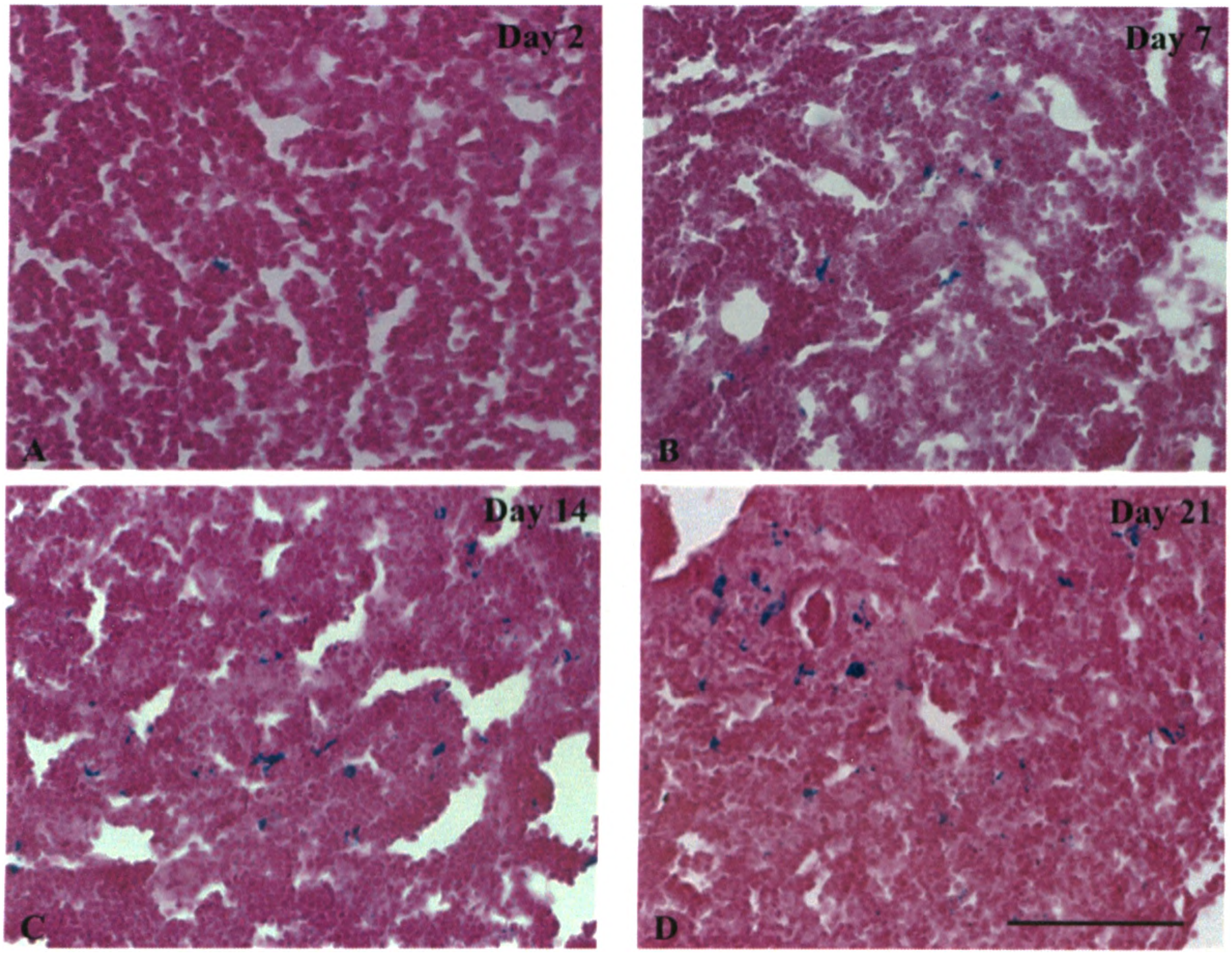

***Figure 4.7.* Distribution of Perl's Prussian blue stained MPIO particles in mouse lymph nodes at four time points after injection of free MPIO**. Distribution of MPIO particles in the right lymph node of a representative mouse injected with free MPIO equivalent to 1×10^6 MPIO-labeled DC at day 2 (A), 7 (B), 14 (C) and 21 (D) post-injection. Sections are counterstained with eosin. Scale bar = 100 μm, Magnification = 40x

Distribution pattern of free SPIO in the draining popliteal lymph node at day 7 post-injection is shown in Figure 4.8. This Section of the lymph node is stained with PPB and counterstained with eosin. It confirms that most of the iron particles accumulated along the edge and sinus areas of the node. Very few blue stained iron particles were observed in deeper regions of the node. This is in agreement with what other studies have reported.

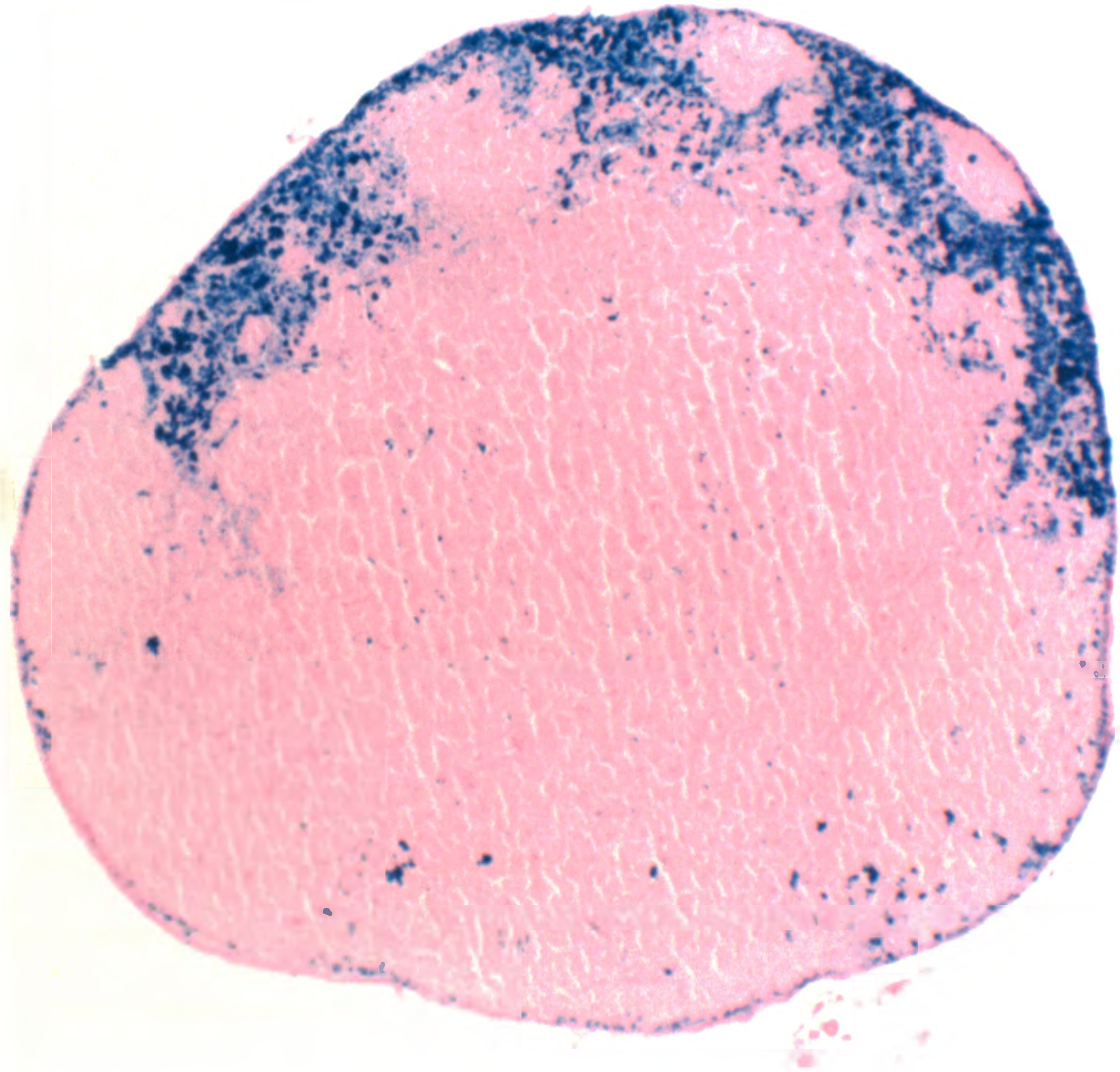

Figure 4.8. **Distribution pattern of free SPIO in mouse draining lymph node.** Distribution of SPIO particles in the lymph node of a representative mouse injected with free SPIO equivalent to 1×10^6 SPIO-labeled DC at day 7 post-injection. Magnification = 5x

4.4. Discussion

In this chapter, we report the longitudinal monitoring of free MPIO and SPIO accumulation in the mouse lymph node using cellular MRI. We investigated the MRI appearance of the mouse lymph nodes after subcutaneous injection of free SPIO and MPIO at day 2, 7, 14 and 21 post-injection to determine how their accumulation in the node would look in MR images and for how long the signal loss they generate would persist in vivo.

Signal loss was observed in the mouse popliteal lymph node 2 days after injection of either free SPIO or MPIO equivalent to 1×10^6 SPIO- or MPIO-labeled DC and persisted for up to 21 days. The pattern of signal loss caused by SPIO was notably different from the signal void observed after the injection of MPIO. Signal void caused by SPIO was maximal at day 2 and diminished over time. In contrast, signal loss caused by the injection of free MPIO was smallest at day 2 compared with later time points. The fact that the signal loss observed after the injection of free SPIO decreased over time is likely related to the fact that SPIO is biodegradable. SPIO particles are known to be degraded and consumed by cells in vivo. As they are broken down by cells, their iron enters the plasma iron pool and contributes in red cell production and other cells activities that need iron and eventually is disposed from the body as iron turnover (13, 14).

The fact that the signal loss observed after the injection of free MPIO increased over time might be explained in part by the fact that MPIO are believed to be inert and therefore they are not broken down by cells (12). In addition, it may indicate that MPIO are taken up by other cells such as macrophages and enter and accumulate in the node over time.

The most interesting difference between SPIO and MPIO is their localization in the popliteal lymph node. In MR images, SPIO is apparent along the edge of the node, in what is likely the subcapsular region of the node, which is consistent with literature (2, 4). Previous studies showed that SPIO cause signal loss in the subcapsular or sinus areas of the node. They suggest that SPIO is passively drained to the lymph node with lymphatic flow rather than actively with immune cells (2, 4).

Long et al examined the MRI and histological appearance of the lymph node 1 and 7 days after injection of free SPIO (4). They reported a corona-like shaped signal loss along the edge of the node which was verified with histology. Their histological analysis showed that no SPIO was present in the the central part of the node at day 7 post-injection. In this study, the goal was in vivo labeling of DC with SPIO-labeled tumor cells. They reported that the earliest time point that SPIO-labeled DC were detected in the paracortex area of the node was day 3. These observations may suggest that free SPIO particles are more likely transported to the node with lymphatic flow.

In this chapter, we observed a large region of signal loss at day 2 and 7 after injection of free SPIO equivalent to 1×10^6 SPIO-labeled DC. A large blooming artifact caused by SPIO at the early time points covered the entire node. However, as signal loss diminished with time, it was observed that SPIO caused a ring-like signal reduction pattern on the subcapsular areas of the node; an observation that was verified by histological analysis.

In contrast, MPIO creates signal loss in the central part of the node. Fluorescence microscopy of the popiteal lymph node at multiple time points confirmed the presence of MPIO particles in the deep cortex of the node. This may mean that MPIO particles are transported to the lymph node within immune cells such as resident DC or macrophages. PPB and eosin staining revealed that MPIO are not in the extracellular spaces. Cellular uptake of iron-oxide particles has been shown to be higher when particles have a larger zeta potential (8-10) and when they are larger in diameter (11, 12). This suggests that MPIO particles are more likely to be actively taken up by cells in vivo, compared with SPIO particles. Therefore, the pattern of signal loss within the lymph node after the injection of free MPIO is more likely to resemble the appearance of the node after MPIO-labeled DC migrate to the node, compared with the ring-like signal void of free SPIO.

4.5. References

1. Ahrens ET, Feili-Hariri M, Xu H, Genove G, Morel PA. Receptor-mediated endocytosis of iron-oxide particles provides efficient labeling of dendritic cells for in vivo MR imaging. Magn Reson Med. 2003 Jun;49(6):1006-13.

2. Baumjohann D, Hess A, Budinsky L, Brune K, Schuler G, Lutz MB. In vivo magnetic resonance imaging of dendritic cell migration into the draining lymph nodes of mice. Eur J Immunol. 2006 Sep;36(9):2544-55.

3. Dekaban GA, Snir J, Shrum B, de Chickera S, Willert C, Merrill M, Said EA, Sekaly RP, Foster PJ, O'Connell PJ. Semiquantitation of mouse dendritic cell migration in vivo using cellular MRI. J Immunother. 2009 Apr;32(3):240-51.

4. Long CM, van Laarhoven HW, Bulte JW, Levitsky HI. Magnetovaccination as a novel method to assess and quantify dendritic cell tumor antigen capture and delivery to lymph nodes. Cancer Res. 2009 Apr 1;69(7):3180-7.

5. Evgenov NV, Medarova Z, Pratt J, Pantazopoulos P, Leyting S, Bonner-Weir S, Moore A. In vivo imaging of immune rejection in transplanted pancreatic islets. Diabetes. 2006 Sep;55(9):2419-28.

6. Pawelczyk E, Arbab AS, Chaudhry A, Balakumaran A, Robey PG, Frank JA. In vitro model of bromodeoxyuridine or iron oxide nanoparticle uptake by activated macrophages from labeled stem cells: implications for cellular therapy. Stem Cells. 2008 May;26(5):1366-75.

7. Lepore AC, Walczak P, Rao MS, Fischer I, Bulte JW. MR imaging of lineage-restricted neural precursors following transplantation into the adult spinal cord. Exp Neurol. 2006 Sep;201(1):49-59.

8. Tabata Y, Ikada Y. Effect of the size and surface charge of polymer microspheres on their phagocytosis by macrophage. Biomaterials. 1988 Jul;9(4):356-62.

9. Piskin E, Tuncel A, Denizli A, Ayhan H. Monosize microbeads based on polystyrene and their modified forms for some selected medical and biological applications. J Biomater Sci Polym Ed 1994;5:451–471.

10. Ahsan F, Rivas IP, Khan MA, Torres Sua′ rez AI. Targeting to macrophages: role of physicochemical properties of particulate carrier-liposomes and microspheres-on the phagocytosis by macrophages. J Control Release 2002;79:29–40.

11. Matuszewski L, Persigehl T, Wall A, Schwindt W, Tombach B, Fobker M, Poremba C, Ebert W, Heindel W, Bremer C. Cell tagging with clinically approved iron oxides: feasibility and effect of lipofection, particle size, and surface coating on labeling efficiency. Radiology. 2005 Apr;235(1):155-61.

12. Shapiro EM, Skrtic S, Koretsky AP. Sizing it up: cellular MRI using micron sized iron oxide particles. Magn Reson Med 2005;53:329–338.

13. Wang YX, Hussain SM, Krestin GP. Superparamagnetic iron oxide contrast agents: physicochemical characteristics and applications in MR imaging. Eur Radiol. 2001;11(11):2319-31.

14. Skotland T, Sontum PC, Oulie I. In vitro stability analyses as a model for metabolism of ferromagnetic particles (Clariscan), a contrast agent for magnetic resonance imaging. J Pharm Biomed Anal. 2002 Apr 15;28(2):323-9.

Chapter 5: Summary and Future Work

Dendritic cells (DC) are highly specialized for immune-surveillance, and the induction and regulation of primary immune responses. This capacity reflects their ability to ingest foreign and self-antigen, which they transport to secondary lymphoid tissues. In addition, DC are exquisitely equipped to sense microbes or molecules released from inflamed or damaged tissues, including tumors. These cues transform DC into potent antigen-presenting cells (APC) that can stimulate antigen-specific effector T cells. Due to these key properties, DC are promising therapeutic candidates for the treatment of cancer.

DC therapy for cancer requires loading of in vitro generated DC with tumor antigens and introducing them back to the patient. The efficacy of the DC-based cancer vaccine is highly dependent on their migration to lymph nodes where they can present antigens to other immune cells. Current common methods to track the migration of DC are invasive and often require biopsy of the nodes. The development of non-invasive methods to follow DC migration in vivo is key to understanding the fate of injected DC.

There have been a few studies reporting labeling DC with superparamagnetic iron oxide (SPIO) contrast agents and tracking their migration in vivo using cellular MRI (1-6). Although, micron size iron oxide particles (MPIO) have been successfully used for imaging a number of cells, such as cancer cells (18), macrophages (7), mesenchymal stem cells (MSC) (8, 9), hepatocytes and fibroblasts (10, 11), this is the first report of the use of MPIO for imaging DC. We believe that MPIO has some advantages over SPIO for preclinical work. For example, MPIO contain more iron per particle compared to SPIO, and as a result MPIO have higher relaxivity than SPIO. Some MPIO also have a fluorescent tag, which makes fluorescence microscopy of cells labeled with MPIO possible.

In Chapter 2, we show that DC can be labeled in vitro with MPIO without substantial effects on viability. We used the FIESTA imaging sequence on a 3 Tesla clinical scanner equipped with a custom-built high-performance gradient coil insert to image the migration of MPIO-labeled DC to mouse lymph nodes in vivo at day 2 post-injection. Migration of MPIO-labeled DC was clearly detected at day 2 after injection of 1×10^6 cells, as a region of signal loss in the popliteal lymph node in MR images. However, signal loss was only observed in the draining node in 1 of 8 mice injected with the lower dose of MPIO-labeled DC (0.1×10^6). Many fewer MPIO-labeled DC were observed in the node by fluorescence microscopy, after the lower dose. These observations indicate that when 0.1×10^6 MPIO-labeled DC are injected the percentage of cells that migrate to the draining lymph node are insufficient to generate contrast for detection by MRI under the conditions used in this thesis. A strong positive correlation was found between green fluorescent DC and red fluorescent MPIO in the draining lymph nodes, indicating that signal voids observed in MR images are very likely created by MPIO-labeled DC.

Of special importance is the observation that fewer DC migrate to the popliteal lymph node when the cells are MPIO-labeled versus unlabeled. Another student in our group (SD, Dekaban lab) has observed the same result for SPIO-labeled DC. None of the published studies on the use of SPIO and MRI for tracking DC migration have investigated this. The fluorescent tag on the MPIO along with the fluorescent labeling of the DC allowed us to look in detail at the relationship between the numbers of MPIO-labeled and unlabeled DC in the node.

Something we do not fully understand is how *many* fewer DC migrate when they are MPIO-labeled. The area of green fluorescence due to PKH+DC in the node is approximately 2x greater for unlabeled DC, at both DC doses.

Another factor to consider is whether or not loading DC with a lower amount of MPIO might restore this effect on migration. The incubation time and concentration of MPIO particles added to the DC in culture can be tailored to result in different iron loading levels.

In Chapter 3, we monitored the signal loss caused by the migration of MPIO-labeled DC to the nodes for a longer time frame, up to day 7 post-injection, in the attempt to answer the question of whether the persistence of signal void due to MPIO reflects the life span of DC. It was reported that subcutaneous injected DC mostly disappear, presumably die, within 2-3 days after their migration to the popliteal lymph node (12). We imaged the mouse body at 2, 3 and 7 days after the subcutaneous injection of 1×10^6 MPIO-labeled DC. Our imaging showed that the signal void in the draining popliteal lymph nodes was visible at day 2 and persisted up to day 7. In addition, the region of signal void increased in size over time, as did the volume of the lymph node itself.

However, fluorescence microscopy of the lymph node revealed that the amount of MPIO in the node was much larger than the amount of DC. This observation suggests that signal void observed in lymph nodes at day 7 might be not due to MPIO-labeled DC but due to MPIO released from dying DC or MPIO within cells other than DC.

When comparing the fluorescence microscopy from this experiment with the results from nodes examined at day 2 (in Chapter 2) we saw that the amount of DC at day 7 was less than what was observed in nodes removed on day 2. This is not surprising since the lifespan of DC in the node is reported as a few days. We also saw that the amount of MPIO in the nodes at day 2 (Chapter 2) or day 7 was similar, again indicating that some of the signal loss observed in images acquired on day 7 post injection may be related to MPIO not associated with DC.

These findings raised another important concern about the use of MPIO contrast agents for cell tracking; the possibility of misinterpreting free MPIO, associated with injected cells or released from dying cells, as MPIO-labeled DC. To address this concern, we investigated the MR appearance of the mouse lymph node after subcutaneous injection of free MPIO and free SPIO. Imaging began at day 2 post-injection and continued until day 21. The injection of free SPIO caused very pronounced signal loss in the MR images at the first time point, which diminished with time and at day 21 post injection appeared as a ring of signal void surrounding the node. In contrast, after the injection of MPIO signal void was observed in the central part of node, resembling the appearance of signal void created by MPIO-labeled DC, and increased with time. Similar results have been reported in the literature for injections of free SPIO. Baumjohann et al. report detection of a corona like signal loss along the edge of lymph node a few hours after footpad injection of free SPIO (4). Long et al. monitored accumulation of SPIO in the node longer, up to day 7, and showed that a ring like region of void is apparent within hours after free SPIO is injected and it does not change until day 7 (6).

It is possible that the relatively small SPIO particles drain to the lymph node with the lymph rather than migrate within cells. On the other hand the larger MPIO are more likely taken up by phagocytic cells and migrate into the cortex and paracortex area of the node. A possible explanation of this difference is that MPIO is more efficient in opsonizing cells. It has been reported that cells take up particles with larger diameter size and higher surface potential more easily (13-16). Taken together these results suggest that caution be taken when using MPIO as the contrast agent to monitor DC in vivo for long periods of time.

This research shows that cellular MRI using MPIO as the cell label provides an efficient technique to be used in pre-clinical studies on DC immunotherapy. DC immunotherapy is a relatively new field that has opened a window of hope to cure diseases including cancer. MRI has gained popularity in clinical and pre-clinical practice because of its ability to provide high resolution and three-dimensional images non-invasively. There are only a few reports of the use of cellular MRI to visualize DC in vivo. So far, only one group has imaged human DC labeled with iron particles (2). Using MPIO as the cell label can be helpful to optimize cellular MRI technique in the detection and visualization of DC-based cancer vaccines in vivo.

There are still many debated issues regarding DC-based cancer vaccines including antigen selection, methods for loading DC with the antigen, methods for DC isolation and activation, dose and frequency of DC vaccination and the route of administration (17). Methods developed in this thesis can be used to allow researchers to investigate these variables. As mentioned earlier, one of the main obstacles to the success of DC-based cancer vaccines is the poor migration of DC to the lymph nodes. Future studies can use this cellular MRI approach to study different strategies to enhance migration of DC.

5.1. References

1. Ahrens ET, Feili-Hariri M, Xu H, Genove G, Morel PA. Receptor-mediated endocytosis of iron-oxide particles provides efficient labeling of dendritic cells for in vivo MR imaging. Magn Reson Med. 2003 Jun;49(6):1006-13.

2. de Vries IJ, Lesterhuis WJ, Barentsz JO, Verdijk P, van Krieken JH, Boerman OC, Oyen WJ, Bonenkamp JJ, Boezeman JB, Adema GJ, Bulte JW, Scheenen TW, Punt CJ, Heerschap A, Figdor CG. Magnetic resonance tracking of dendritic cells in melanoma patients for monitoring of cellular therapy. Nat Biotechnol. 2005 Nov;23(11):1407-13.

3. Verdijk P, Scheenen TW, Lesterhuis WJ, Gambarota G, Veltien AA, Walczak P, Scharenborg NM, Bulte JW, Punt CJ, Heerschap A, Figdor CG, de Vries IJ. Sensitivity of magnetic resonance imaging of dendritic cells for in vivo tracking of cellular cancer vaccines. Int J Cancer. 2006 Mar 1;120(5):978-84.

4. Baumjohann D, Hess A, Budinsky L, Brune K, Schuler G, Lutz MB. In vivo magnetic resonance imaging of dendritic cell migration into the draining lymph nodes of mice. Eur J Immunol. 2006 Sep;36(9):2544-55.

5. Dekaban GA, Snir J, Shrum B, de Chickera S, Willert C, Merrill M, Said EA, Sekaly RP, Foster PJ, O'Connell PJ. Semiquantitation of mouse dendritic cell migration in vivo using cellular MRI. J Immunother. 2009 Apr;32(3):240-51.

6. Long CM, van Laarhoven HW, Bulte JW, Levitsky HI. Magnetovaccination as a novel method to assess and quantify dendritic cell tumor antigen capture and delivery to lymph nodes. Cancer Res. 2009 Apr 1;69(7):3180-7.

7. Williams JB, Ye Q, Hitchens TK, Kaufman CL, Ho C. MRI detection of macrophages labeled using micrometer-sized iron oxide particles. J Magn Reson Imaging. 2007 Jun;25(6):1210-8.

8. Hinds KA, Hill JM, Shapiro EM, Laukkanen MO, Silva AC, Combs CA, Varney TR, Balaban RS, Koretsky AP, Dunbar CE. Highly efficient endosomal labeling of progenitor and stem cells with large magnetic particles allows magnetic resonance imaging of single cells. Blood, 2003. 102(3): p. 867-72.

9. Gonzalez-Lara LE, Xu X, Hofstetrova K, Pniak A, Brown A, Foster PJ. In vivo magnetic resonance imaging of spinal cord injury in the mouse. J Neurotrauma. 2009 May;26(5):753-62.

10. Shapiro EM, S Skrtic, AP Koretsky. Sizing it up: cellular MRI using micron-sized iron oxide particles. Magn Reson Med, 2005. 53(2): p. 329-38.

11. Shapiro EM, Skrtic S, Sharer K, Hill JM, Dunbar CE, Koretsky AP. MRI detection of single particles for cellular imaging. Proc Natl Acad Sci U S A. 2004 Jul 27;101(30):10901-6. Epub 2004 Jul 15.

12. Huck SP, Tang SC, Andrew KA, Yang J, Harper JL, Ronchese F. Activation and route of administration both determine the ability of bone marrow-derived dendritic cells to accumulate in secondary lymphoid organs and prime CD8+ T cells against tumors. Cancer Immunol Immunother. 2008 Jan;57(1):63-71.

13. Tabata Y, Ikada Y. Effect of the size and surface charge of polymer microspheres on their phagocytosis by macrophage. Biomaterials. 1988 Jul;9(4):356-62.

14. Piskin E, Tuncel A, Denizli A, Ayhan H. Monosize microbeads based on polystyrene and their modified forms for some selected medical and biological applications. J Biomater Sci Polym Ed 1994;5:451–471.

15. Ahsan F, Rivas IP, Khan MA, Torres Sua′ rez AI. Targeting to macrophages: role of physicochemical properties of particulate carrier-liposomes and microspheres-on the phagocytosis by macrophages. J Control Release 2002;79:29–40.

16. Matuszewski L, Persigehl T, Wall A, Schwindt W, Tombach B, Fobker M, Poremba C, Ebert W, Heindel W, Bremer C. Cell tagging with clinically approved iron oxides: feasibility and effect of lipofection, particle size, and surface coating on labeling efficiency. Radiology. 2005 Apr;235(1):155-61.

17. Figdor CG, de Vries IJ, Lesterhuis WJ, Melief CJ. Dendritic cell immunotherapy: mapping the way. Nat Med. 2004 May;10(5):475-80.

18. Heyn C, Ronald JA, Mackenzie LT, MacDonald IC, Chambers AF, Rutt BK, Foster PJ. In vivo magnetic resonance imaging of single cells in mouse brain with optical validation. Magn Reson Med. 2006 Jan;55(1):23-9.

Appendix 1. Protocol Optimization

The following representative images were acquired during steps taken to optimize the image quality, image artifact and visualization of the mouse lymph nodes.

1. Increasing Image Quality

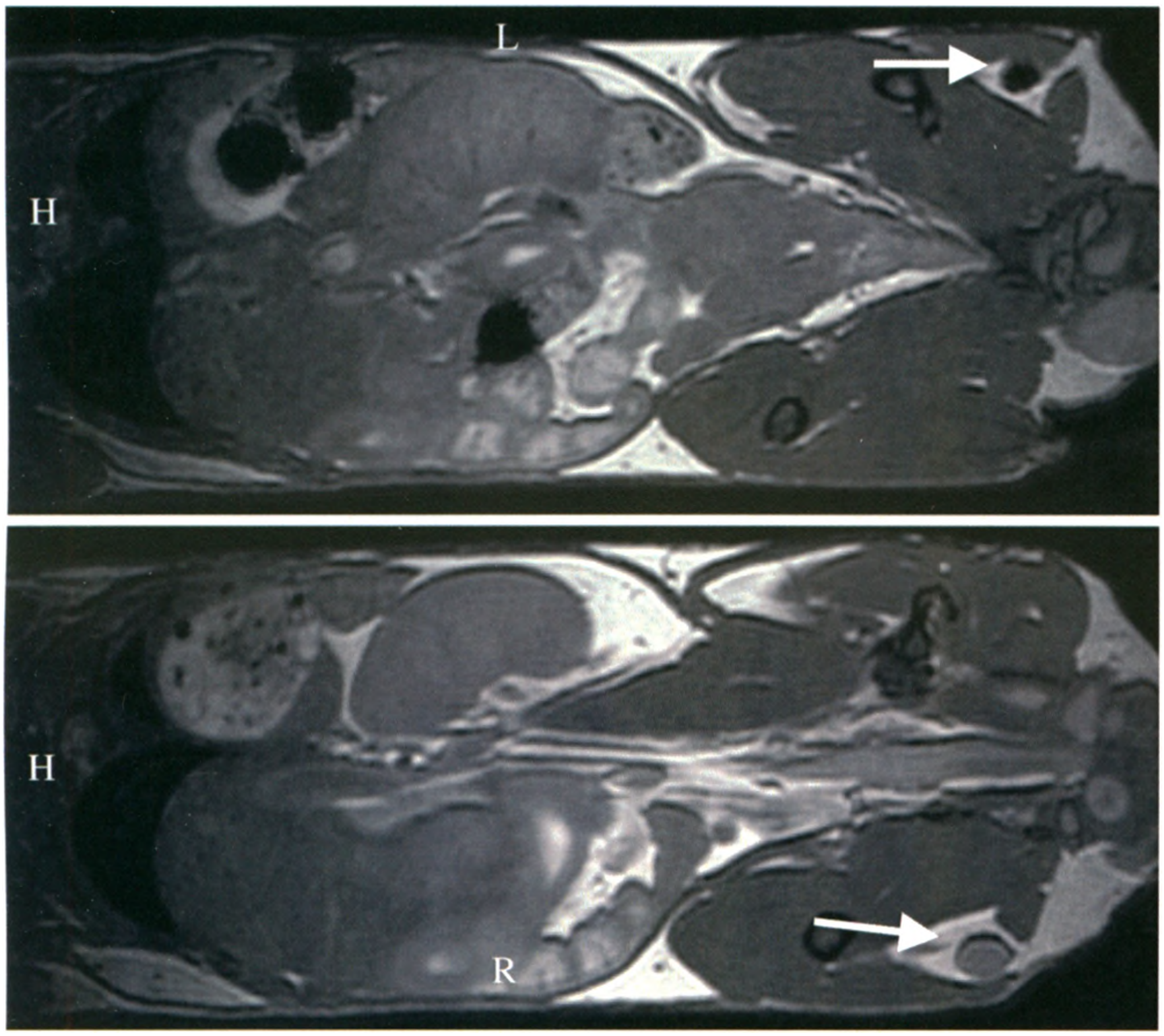

Figure 1. Coronal View: TR/TE= 4.2/2.1, Resolution = 200 μm^3, Field of view (FOV) = 6 cm^2, Bandwidth (BW) = 62.5 kHz, Flip angle (FA) = 20°, Phase cycling = 8, Signal average = 1, Scan time = 21 m, L = left, R = right, H = head

Signal to noise ratio (SNR) of node = 82.5, Contrast to noise ratio between fat and node (CNR) = 60.2

Figure 2. Axial view: TR/TE= 4.2/2.1, Resolution = 200 μm^3, FOV = 3 cm^2, BW = 62.5 kHz, FA = 20°, Phase cycling = 8, Signal average = 1, Scan time = 11 m, L = left, R = right

SNR of node = 30, CNR = 14.5

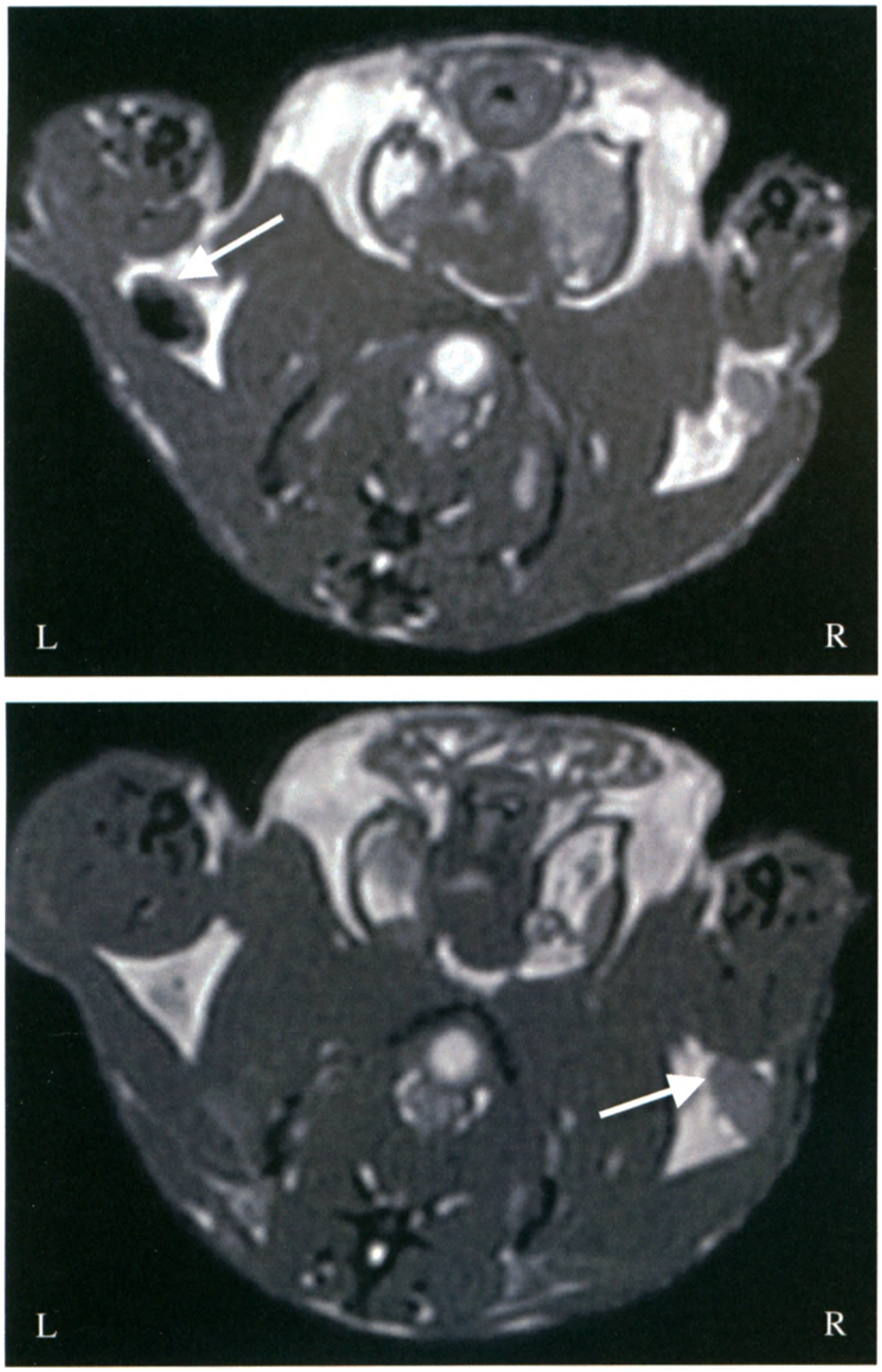

Figure 3. TR/TE= 4.2/2.1, Resolution = 200 μm^3, FOV = 3 cm^2, BW = 62.5 kHz, FA = 20°, Phase cycling = 4, Signal average = 2, Scan time= 11 m, L = left, R = right

SNR of node = 51, CNR = 31.4

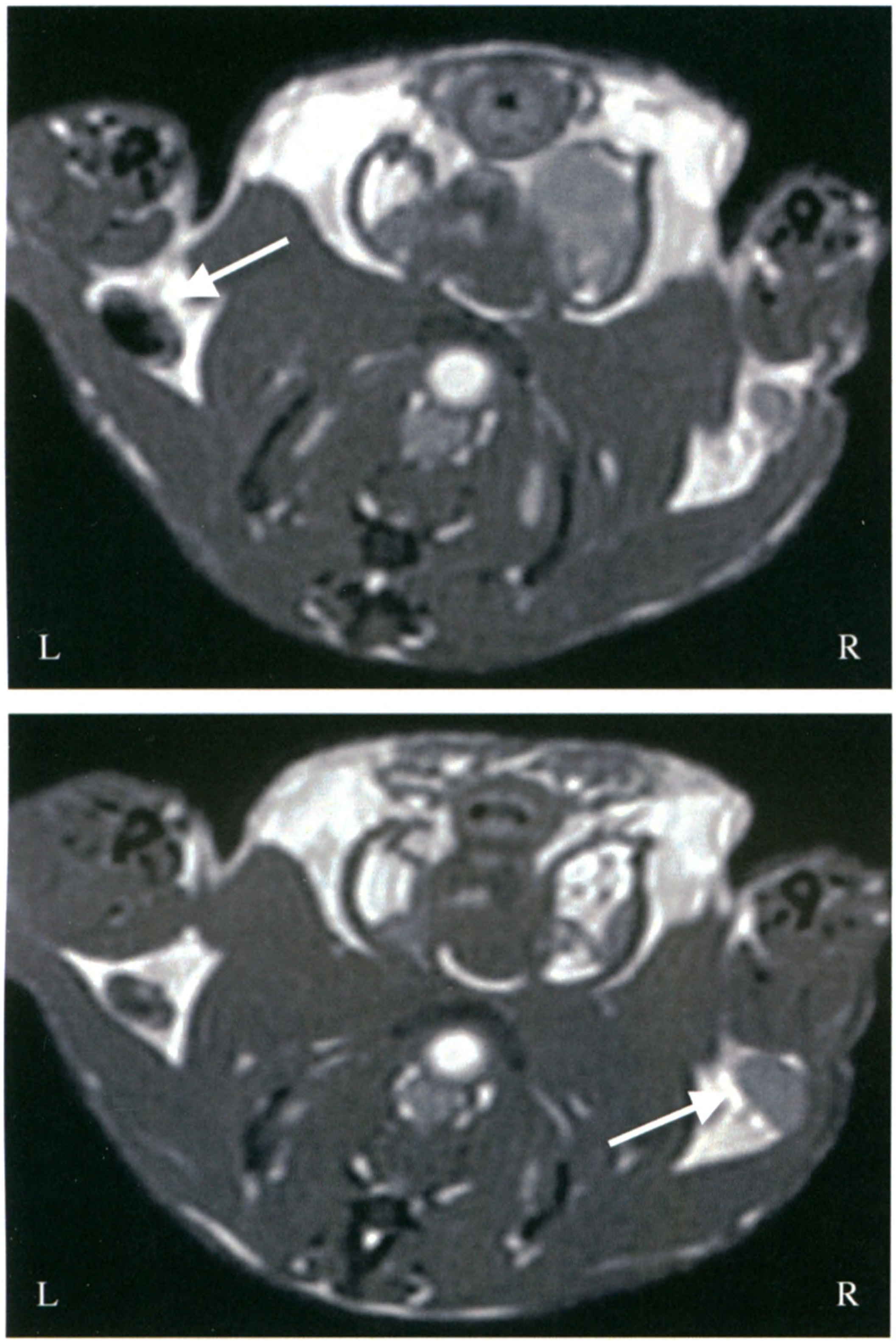

Figure 4. TR/TE= 4.2/2.1, Resolution = 200 μm^3, FOV = 3 cm^2, BW = 62.5 kHz, FA = 20°, Phase cycling = 4, Signal average = 4, Scan time = 41 m, L = left, R = right

SNR of node = 63.8, CNR = 55.4

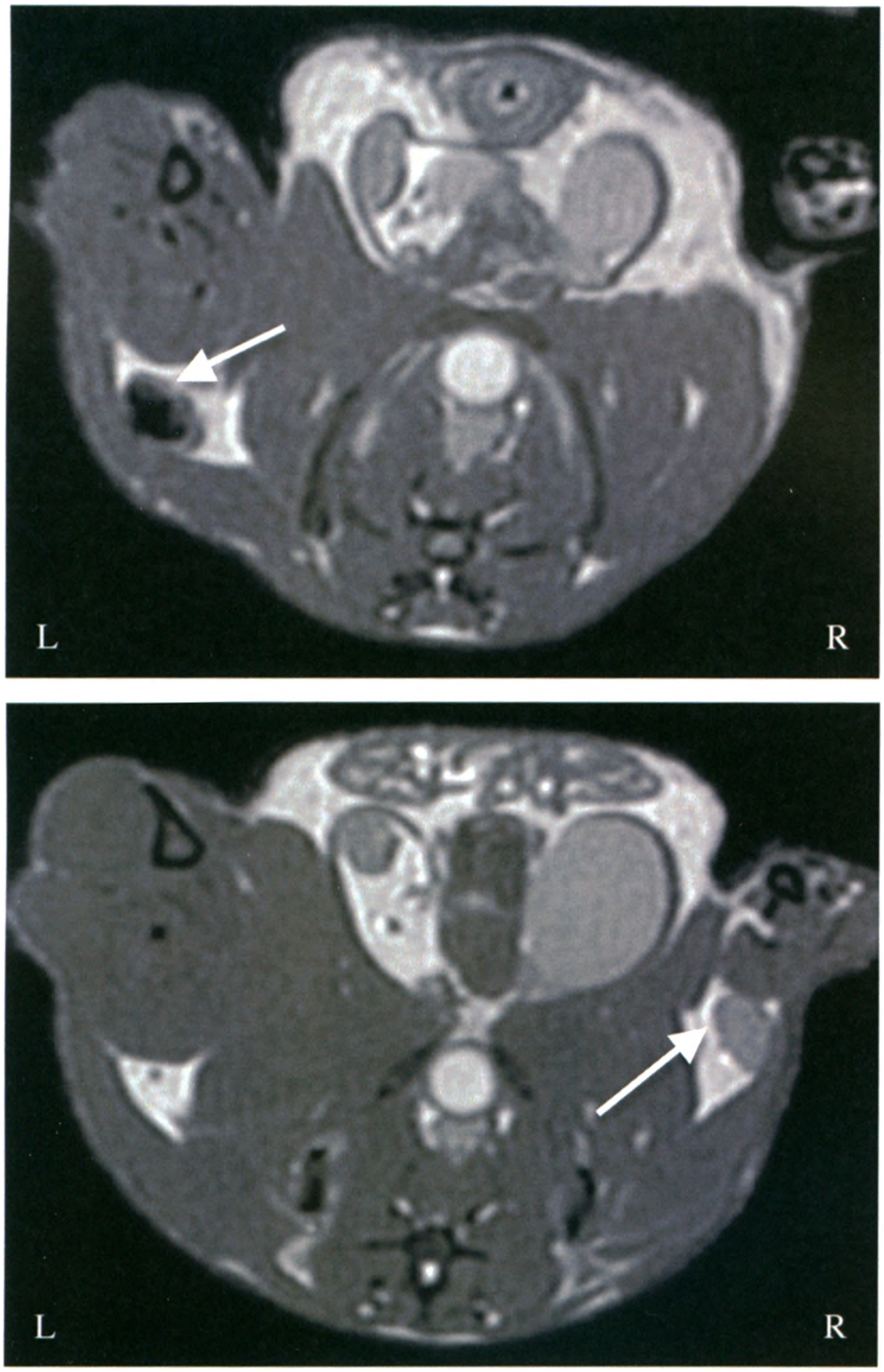

Figure 5.TR/TE= 4.2/2.1, Resolution = 200 μm^3, FOV = 3 cm^2, BW = 62.5 kHz, FA = 20°, Phase cycling = 8, Signal average = 2, Scan time = 21 m, L = left, R = right

SNR of node = 61.7, CNR = 40

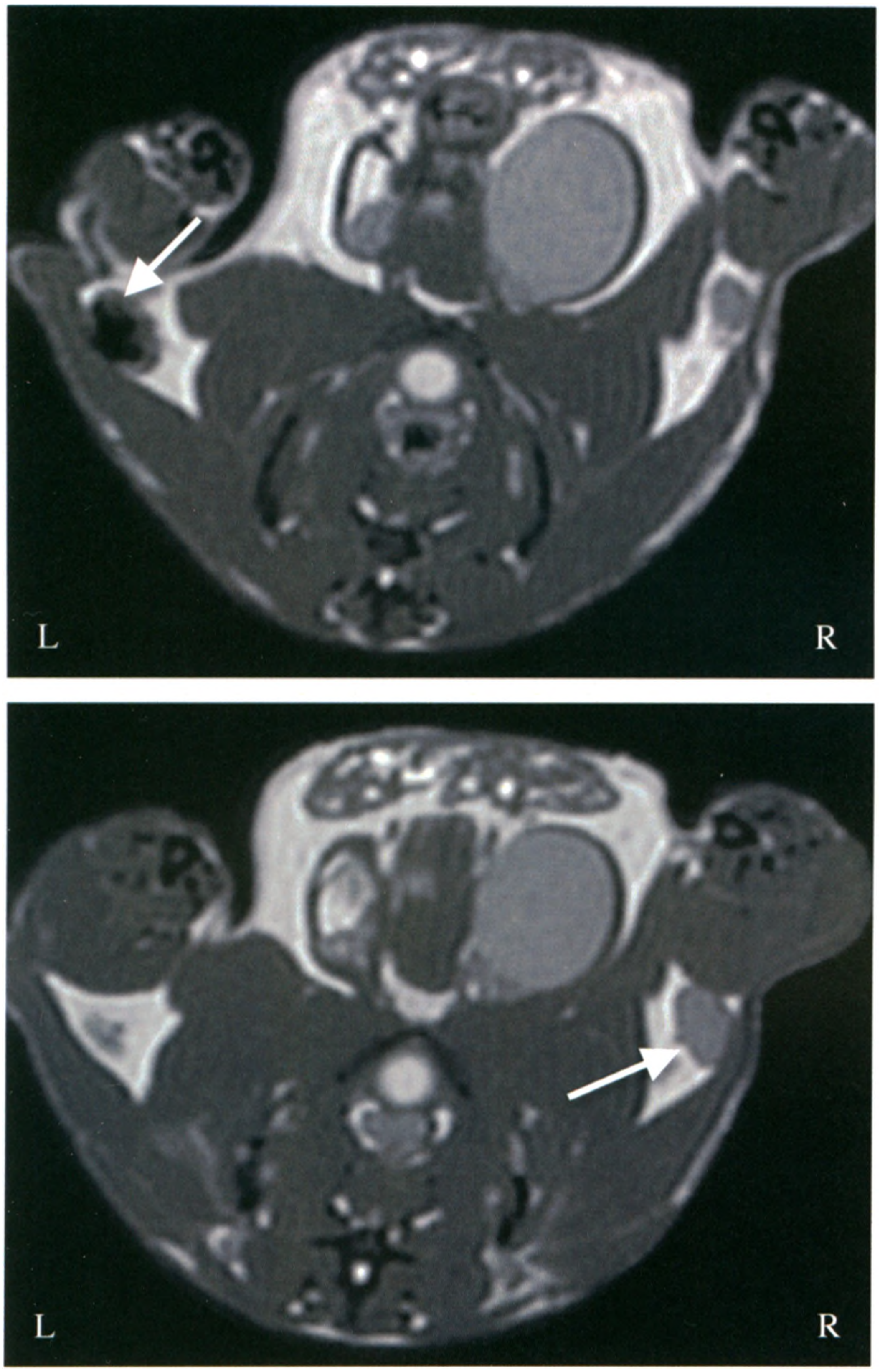

Figure 6.TR/TE= 4.2/2.1, Resolution = 200 μm^3, FOV = 3 cm^2, BW = 62.5 kHz, FA = 20°, Phase cycling = 8, Signal average = 4, Scan time = 43 m, L = left, R = right

SNR of node = 99, CNR = 70.3

2. Varying Flip Angle

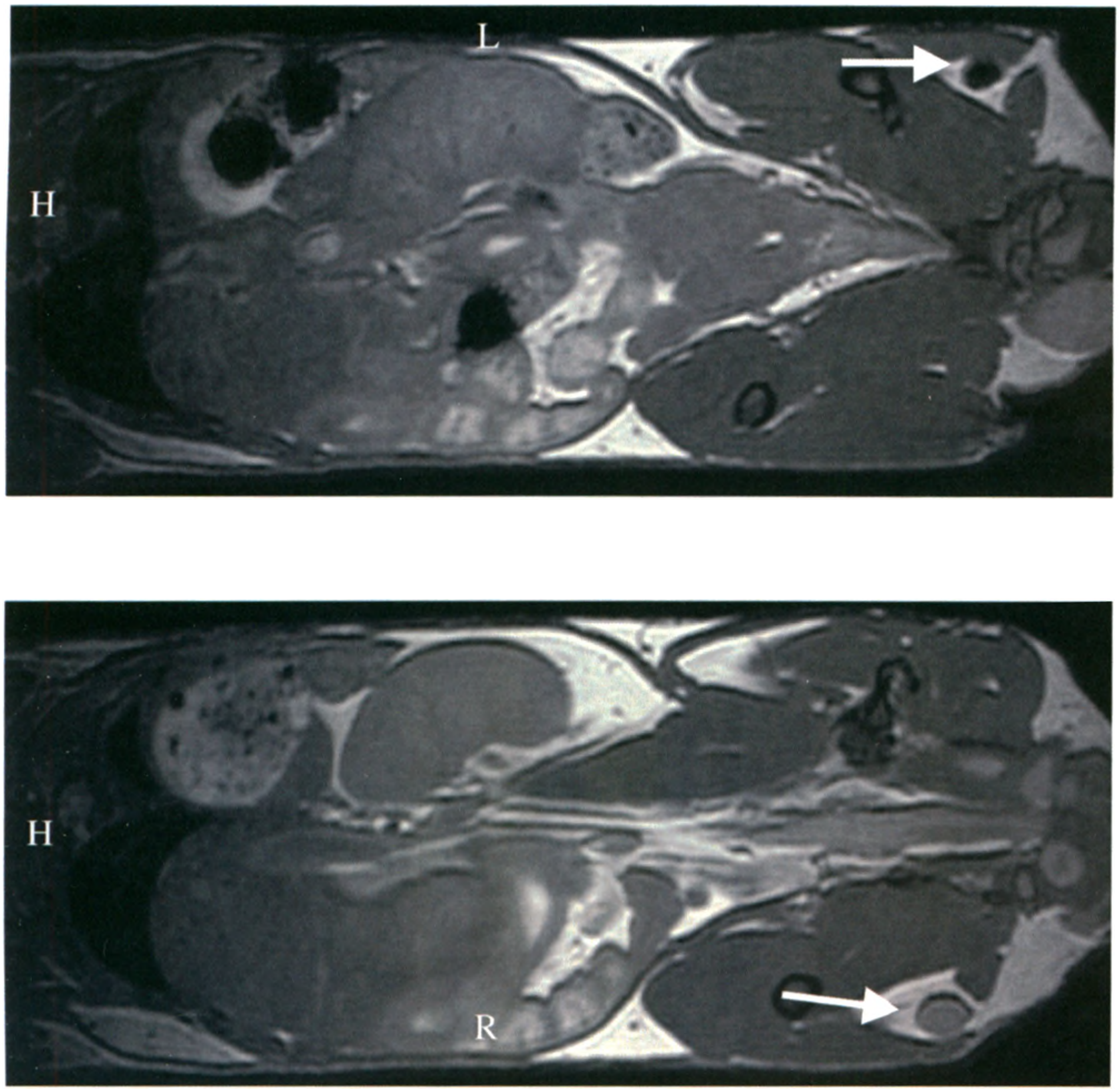

***Figure** 7.* TR/TE= 4.2/2.1, Resolution = 200 µm^3, FOV = 6 cm^2, BW = 62.5 kHz, FA = 20°, Phase cycling = 8, Signal average = 1, Scan time = 21 m, L = left, R = right, H = head

SNR of node = 82.5, CNR = 60.2

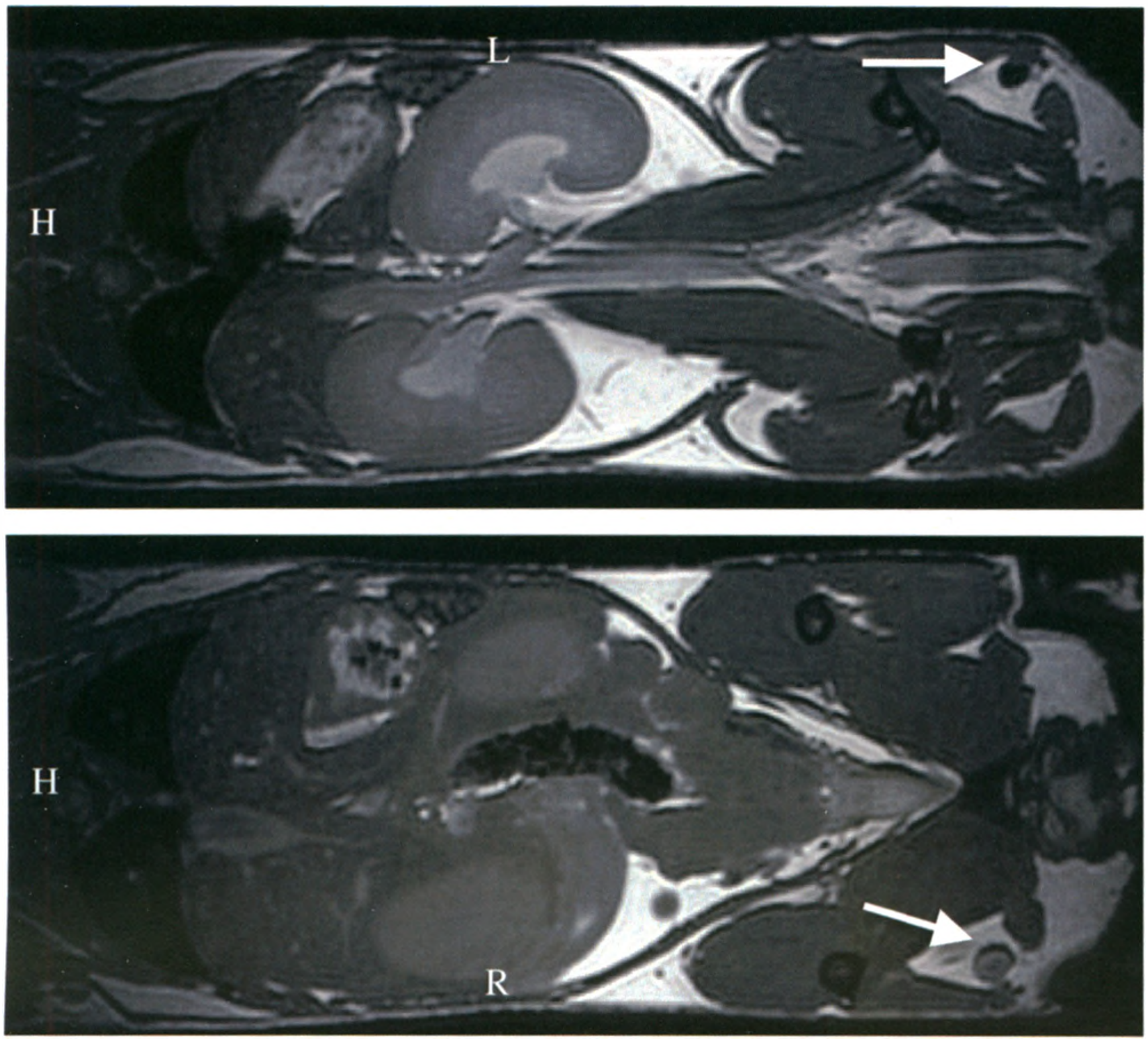

Figure 8. TR/TE= 4.2/2.1, Resolution = 200 μm^3, FOV = 6 cm^2, BW = 62.5 kHz, FA = 30°, Phase cycling = 8, Signal average = 1, Scan time= 21 m, L = left, R =right, H = head

SNR of node = 72.5, CNR = 74.7

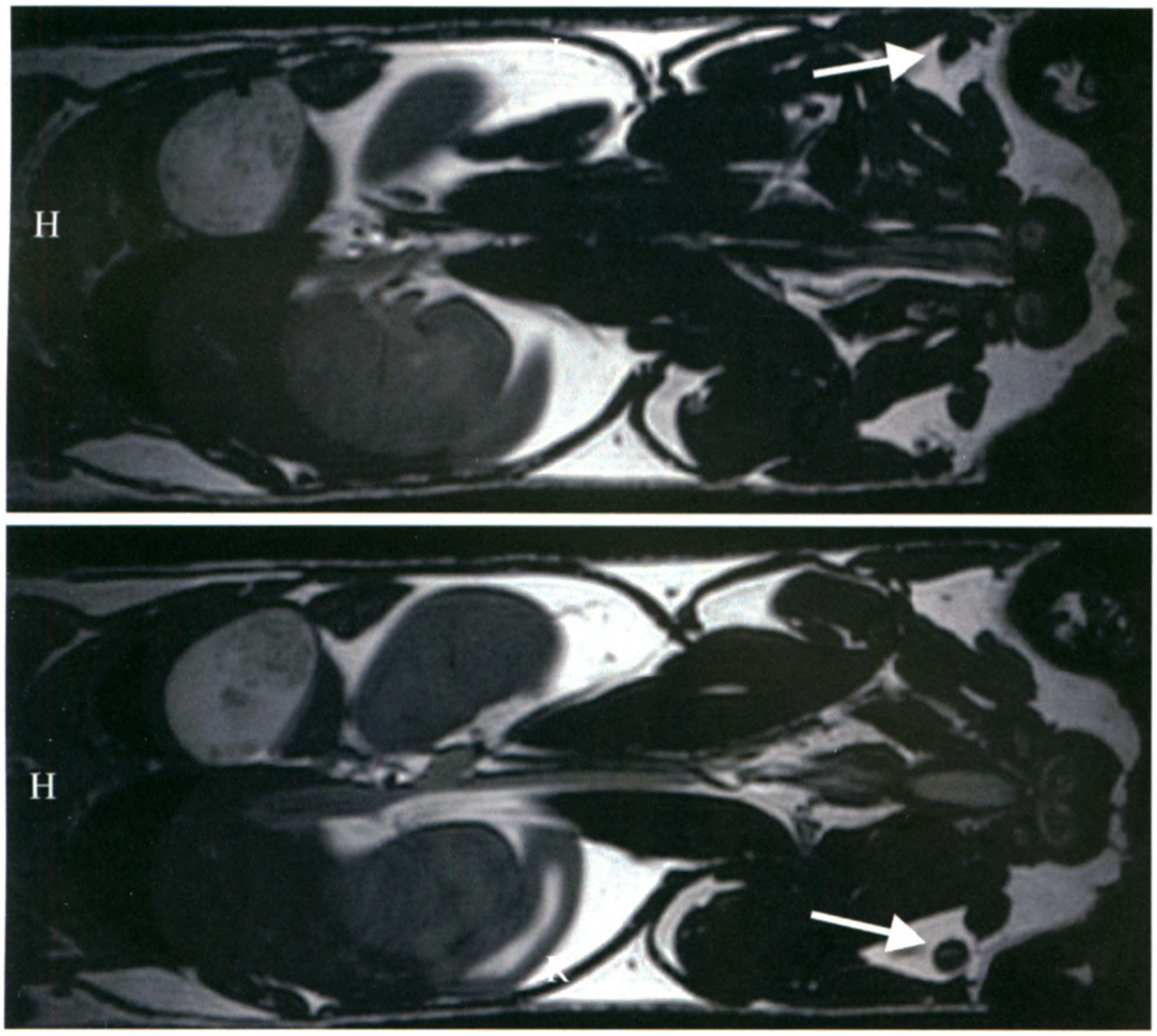

Figure 9. TR/TE= 4.2/2.1, Resolution = 200 μm^3, FOV = 6 cm^2, BW = 62.5 kHz, FA = 40°, Phase cycling = 8, Signal average = 1, Scan time= 21 m, L = left, R =right, H = head

SNR of node = 50, CNR = 150.2

3. Increasing Echo Time

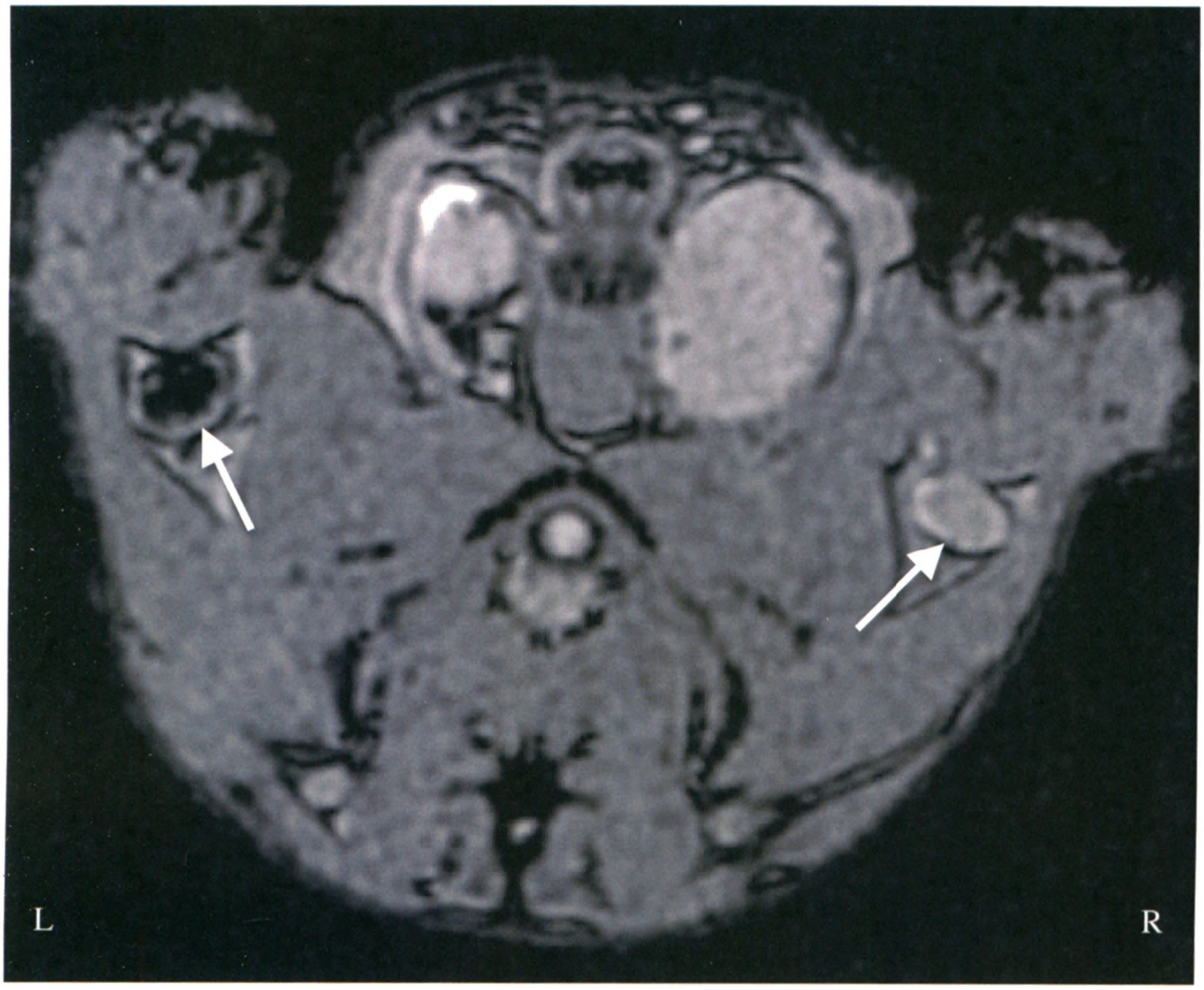

Figure 10. TR/TE= 16/8. Resolution = 200 µm^3, FOV = 3 cm^2, BW = 62.5 kHz, FA = 20°, Phase cycling = 8, Signal average = 1, Scan time = 41 m, L = left, R = right, H = head

SNR of node = 32, CNR = -3.3

4. Conclusion

Coronal plane was used as the imaging plane and the following parameters were set as the final protocol: TR/TE= 4.2/2.1, Resolution = 200 μm^3, FOV = 6 cm^2, Bandwidth BW = 62.5 kHz, Flip angle FA = 20°, Phase cycling = 8, Signal average = 1, Scan time = 21 m

Appendix 2. Supplementary Fluorescent Images

The following images are representative fluorescent images of the lymph nodes, provided to support results of the fluorescence microscopy in chapter 2 and chapter 3.

1. Chapter 2

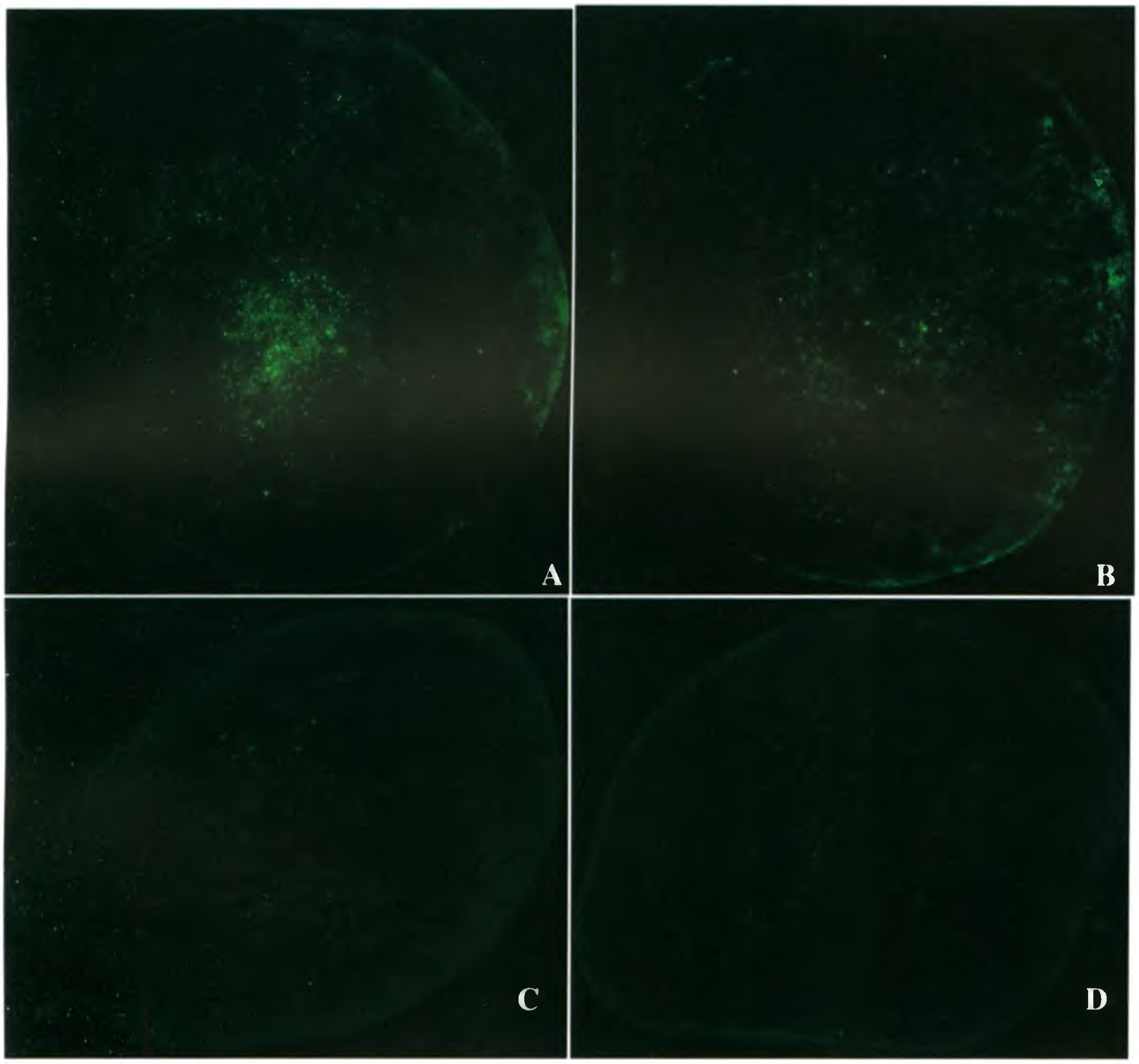

Figure 1. Distribution of green PKH fluorescence in popliteal lymph nodes two days after injection of (A) 1×10^6 unlabeled DC, (B) 1×10^6 MPIO-labeled DC, (C) 0.1×10^6 unlabeled DC or (D) 0.1×10^6 MPIO-labeled DC. The green fluorescence regions correspond to the presence of PKH+ DC.

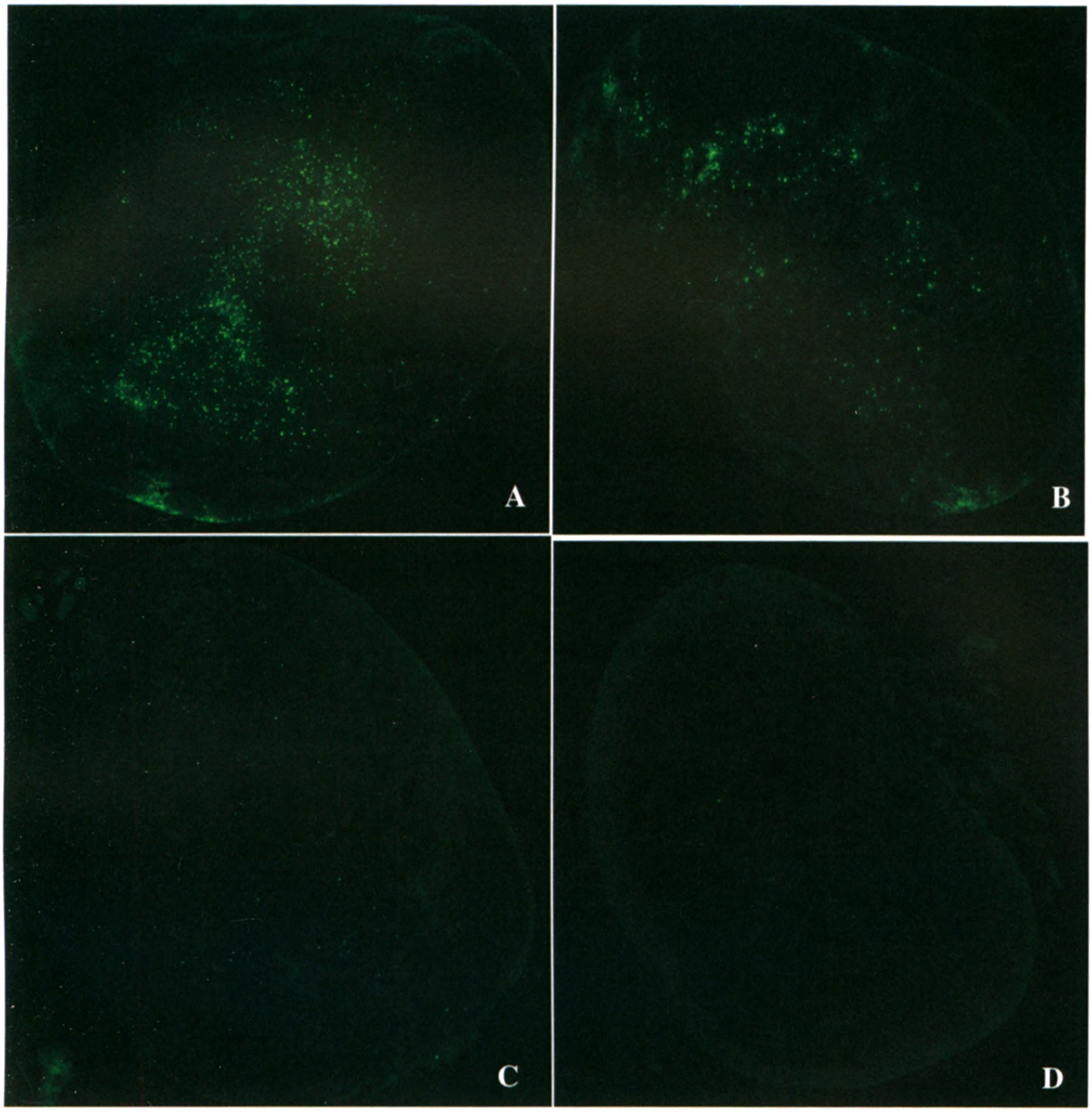

Figure 2. Distribution of green PKH fluorescence in popliteal lymph nodes two days after injection of (A) 1×10^6 unlabeled DC, (B) 1×10^6 MPIO-labeled DC, (C) 0.1×10^6 unlabeled DC or (D) 0.1×10^6 MPIO-labeled DC. The green fluorescence regions correspond to the presence of PKH+ DC.

Figure 3. Distribution of green PKH+ DC (A, C, E) and flash red MPIO (B, D, F) in popliteal lymph nodes 2 days after the injection of 1×106 MPIO-labeled DC. The green fluorescence regions correspond the presence of PKH+ DC and red fluorescence regions to MPIO particles.

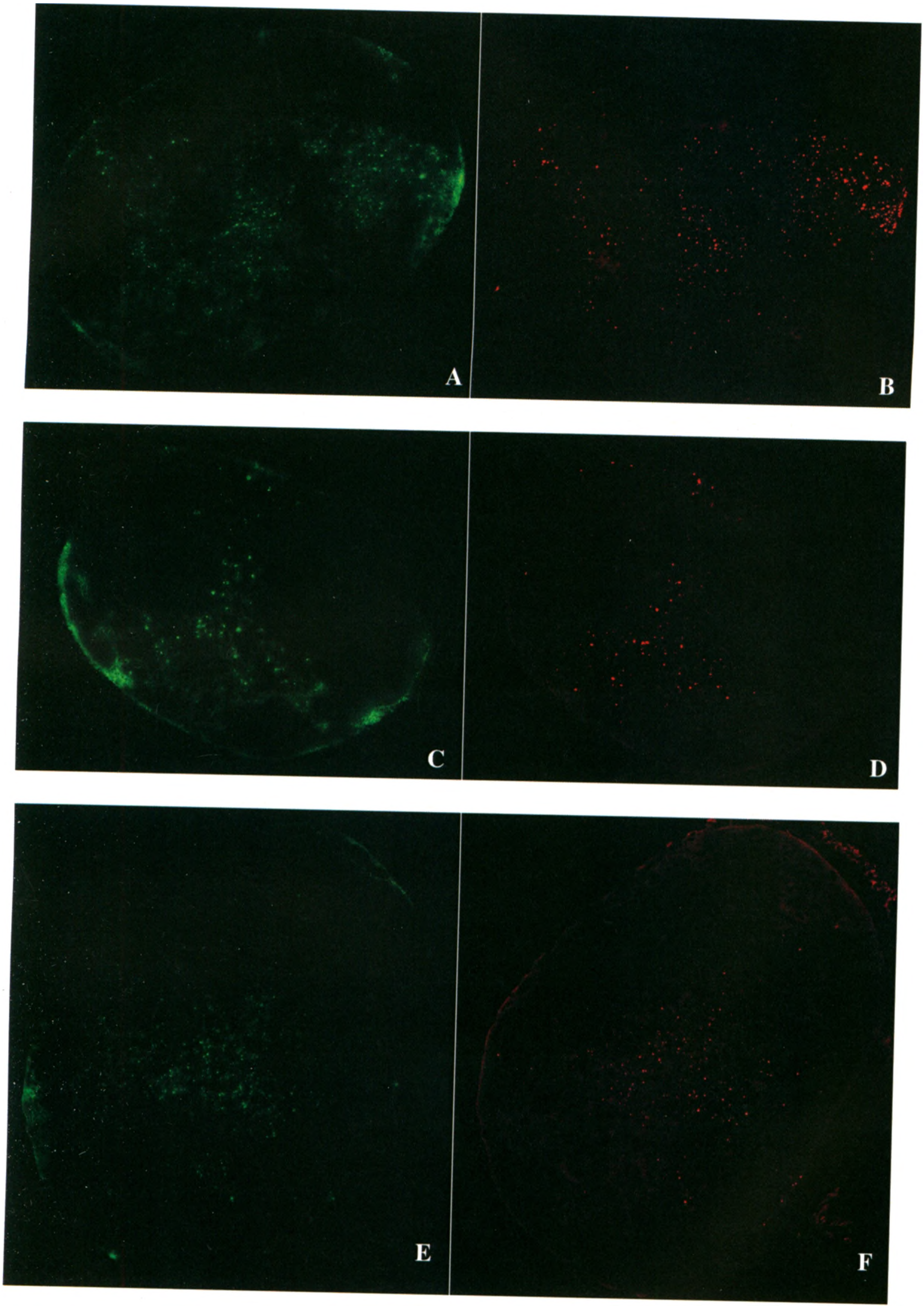
A
B
C
D
E
F

2. Chapter 3

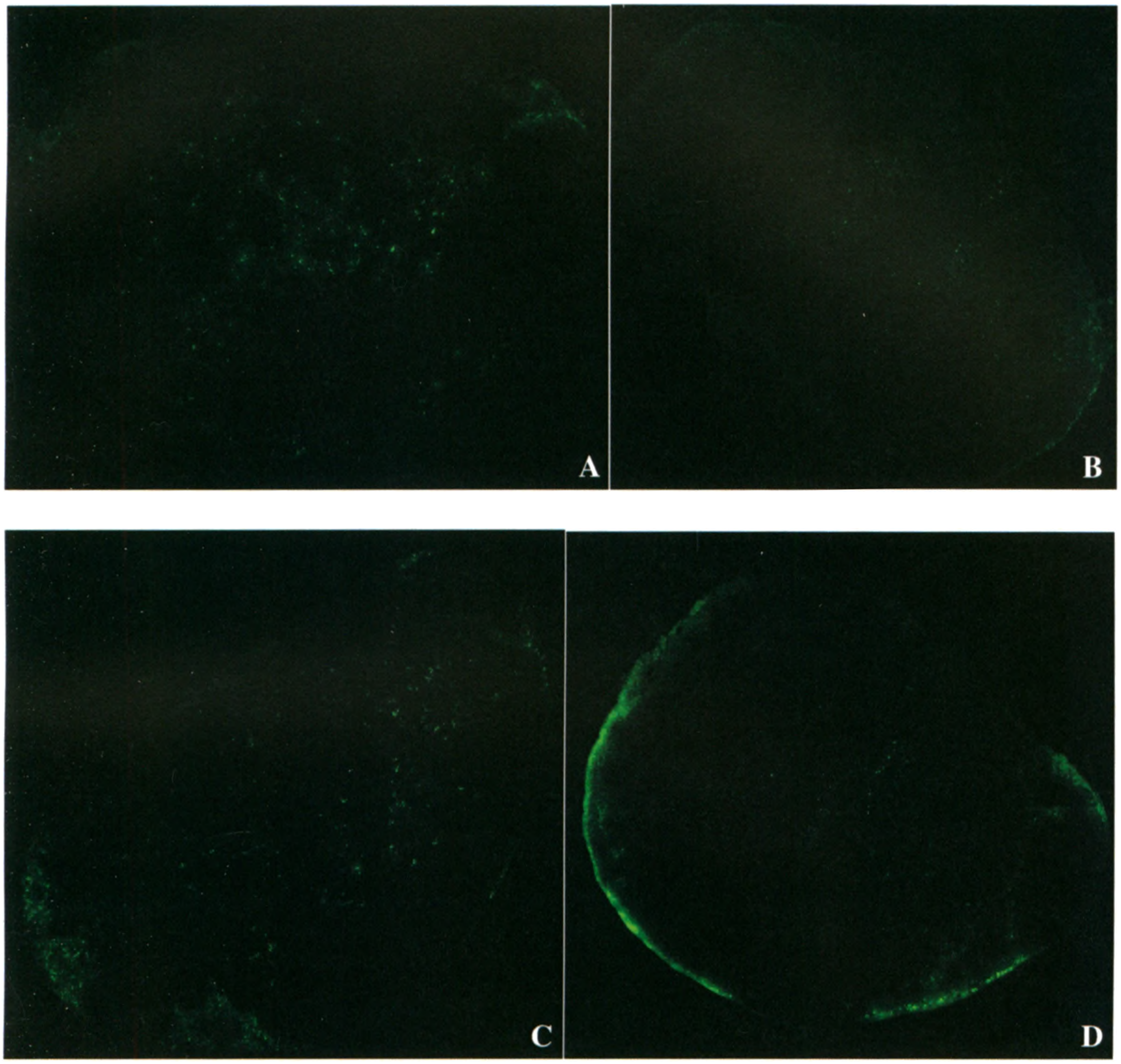

Figure 4. Distribution of green PKH fluorescence in popliteal lymph nodes seven days after injection of (A and C) 1×10^6 unlabeled DC and (B and D) 1×10^6 MPIO-labeled DC.

Figure 5. Distribution of green PKH+ DC (A, C, E) and flash red MPIO (B, D, F) in popliteal lymph nodes 7 days after the injection of 1×10^6 MPIO-labeled DC.

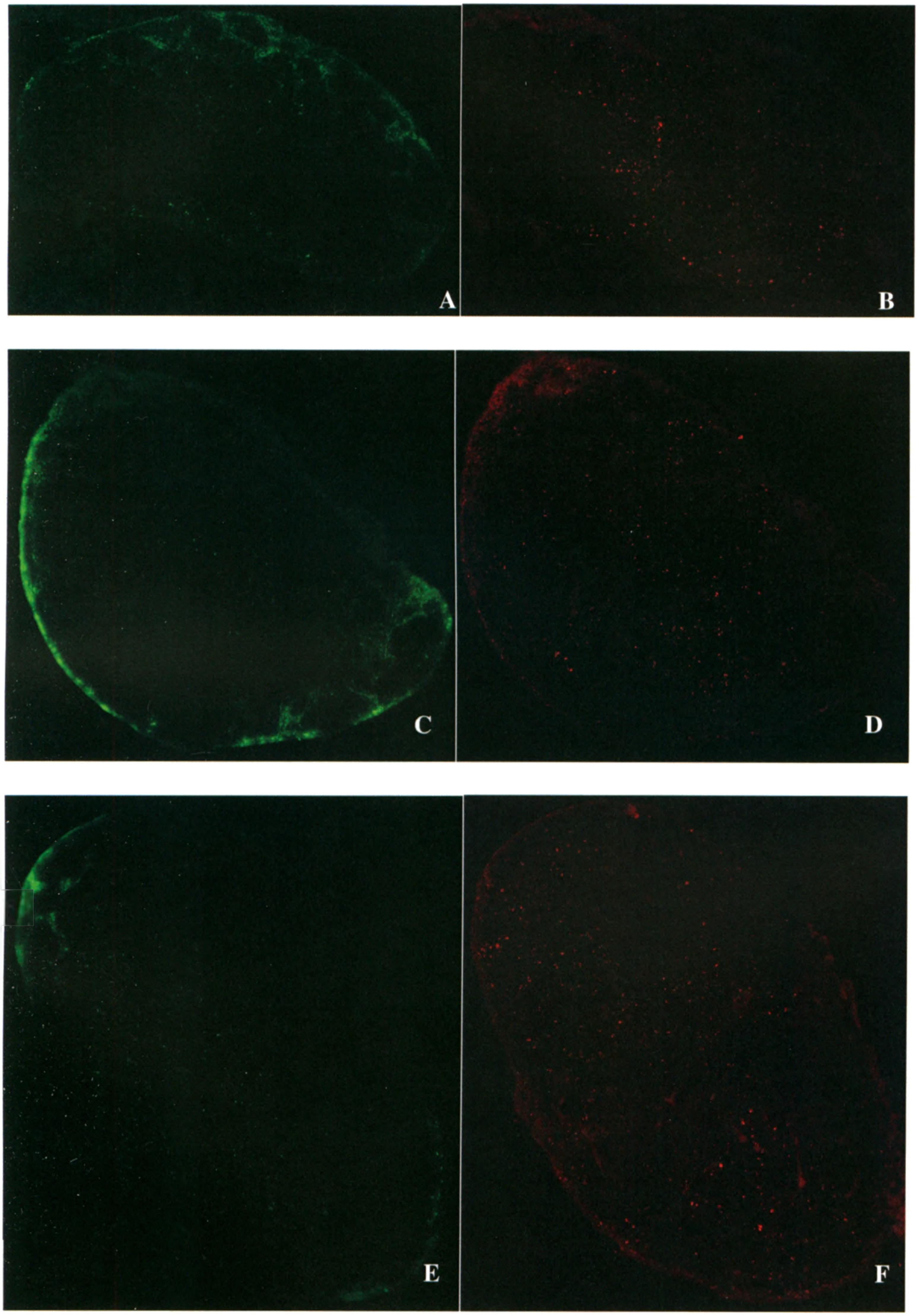
A
B
C
D
E
F

Appendix 3. Proof of Ethics Approval

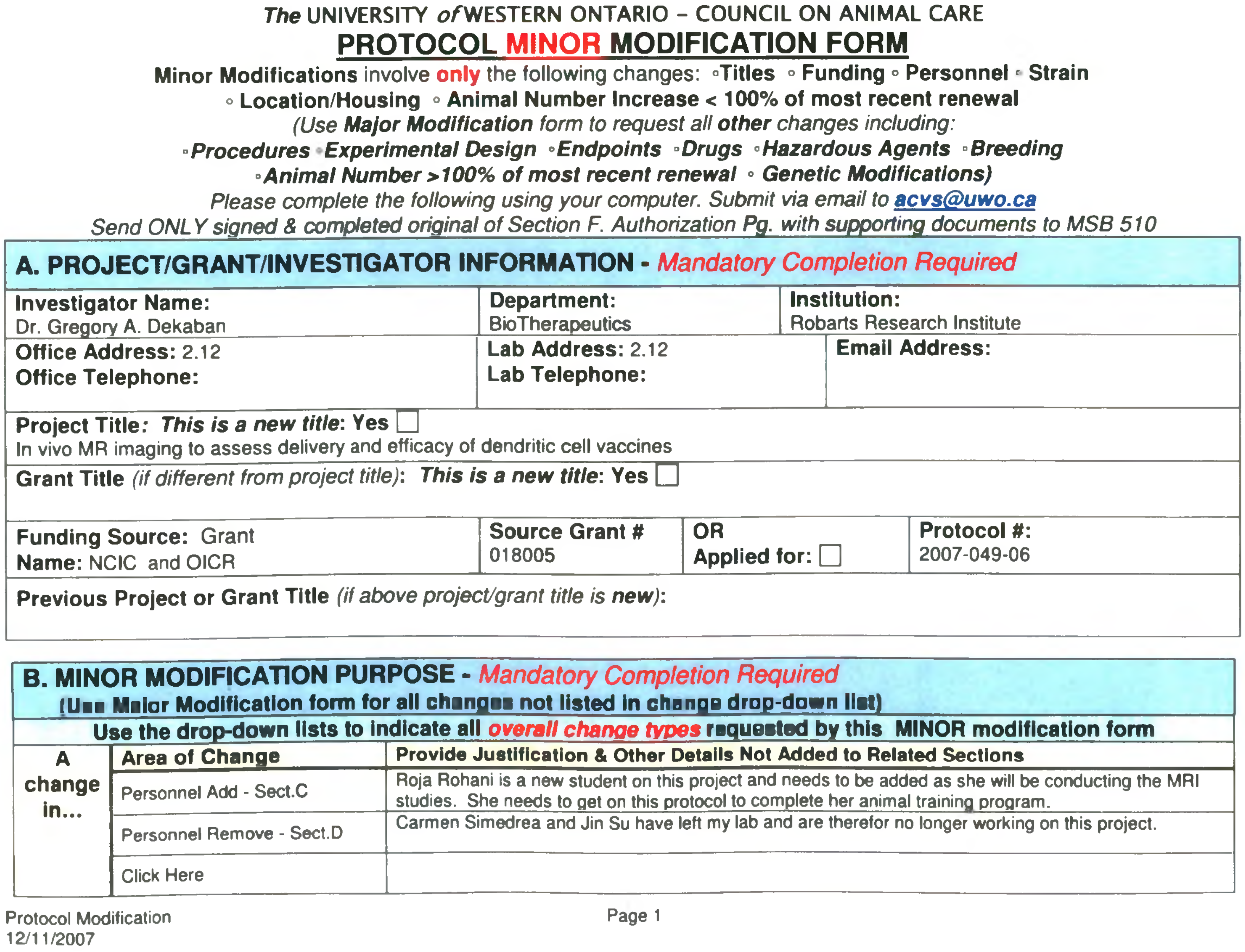

The UNIVERSITY *of* WESTERN ONTARIO – COUNCIL ON ANIMAL CARE

PROTOCOL MINOR MODIFICATION FORM

Minor Modifications involve **only** the following changes: ◦**Titles** ◦ **Funding** ◦ **Personnel** ◦ **Strain** ◦ **Location/Housing** ◦ **Animal Number Increase < 100% of most recent renewal**

*(Use **Major Modification** form to request all **other** changes including:*
*◦**Procedures** ◦**Experimental Design** ◦**Endpoints** ◦**Drugs** ◦**Hazardous Agents** ◦**Breeding** ◦**Animal Number >100% of most recent renewal** ◦ **Genetic Modifications**)*

Please complete the following using your computer. Submit via email to acvs@uwo.ca
Send ONLY signed & completed original of Section F. Authorization Pg. with supporting documents to MSB 510

A. PROJECT/GRANT/INVESTIGATOR INFORMATION - *Mandatory Completion Required*

Investigator Name: Dr. Gregory A. Dekaban	**Department:** BioTherapeutics	**Institution:** Robarts Research Institute
Office Address: 2.12 **Office Telephone:**	**Lab Address:** 2.12 **Lab Telephone:**	**Email Address:**

Project Title*:* ***This is a new title*****: Yes** ☐
In vivo MR imaging to assess delivery and efficacy of dendritic cell vaccines

Grant Title *(if different from project title)*: ***This is a new title*****: Yes** ☐

Funding Source: Grant **Name:** NCIC and OICR	**Source Grant #** 018005	**OR** **Applied for:** ☐	**Protocol #:** 2007-049-06

Previous Project or Grant Title *(if above project/grant title is **new**)*:

B. MINOR MODIFICATION PURPOSE - *Mandatory Completion Required*
(Use Major Modification form for all changes not listed in change drop-down list)

Use the drop-down lists to indicate all *overall change types* requested by this MINOR modification form

A change in...	**Area of Change**	**Provide Justification & Other Details Not Added to Related Sections**
	Personnel Add - Sect.C	Roja Rohani is a new student on this project and needs to be added as she will be conducting the MRI studies. She needs to get on this protocol to complete her animal training program.
	Personnel Remove - Sect.D	Carmen Simedrea and Jin Su have left my lab and are therefor no longer working on this project.
	Click Here	

Protocol Modification
12/11/2007

Page 1